POLITECNICO DI MILANO

School of Industrial and Information Engineering

Master of Science – Biomedical Engineering

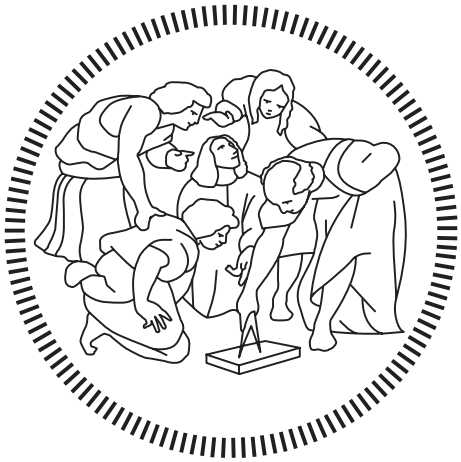

FSI STUDY IN A BOVINE ARCH GEOMETRY WITH DIFFERENT SETS OF BOUNDARY CONDITIONS TO IDENTIFY FLUID DYNAMIC PATTERNS THAT COULD INITIATE AORTIC DISSECTION

Supervisor:

Prof. Alberto Redaelli

Co-Supervisor:

Prof. Elena Di Martino (University of Calgary)

PostDoc. Arianna Forneris (University of Calgary)

Author:

Elisa Casari

Matr. 919155

Academic Year 2020-2021

TABLE OF CONTENT

LIST OF FIGURES

LIST OF TABLES

GLOSSARY

AD	Aortic Dissection
ALE	Arbitrary Lagrangian Eulerian
BAV	Bicuspid Aortic Valve
BC	Boundary Condition
BCT	Brachiocephalic Trunk
BP	Blood Pressure
CFD	Computational Fluid Dynamic
CILCA	Common origin of the Innominate and Left Carotid Artery
CT	Computer Tomography
CXR	Chest Radiography
EC	Endothelial Cell
ECM	Extracellular Matrix
FEA	Finite Element Analysis
FSI	Fluid Structure Interaction
IHM	Intramural Hematoma
LCCA	Left Common Carotid Artery
MRI	Magnetic Resonance Imaging
OSI	Oscillatory Shear Index
PWS	Peak Wall Stress
RBC	Red Blood Cell
RRT	Relative Residence Time
SCA	Left Subclavian Artery
SIMPLE	Semi-Implicit Method for Pressure-Linked Equation
TAV	Tricuspid Aortic Valve
TAVR	Transcatheter Aortic Valve Replacement
TAWSS	Time Averaged Wall Shear Stress
TEE	Transoesophageal Echocardiography
TEVAR	Thoracic Endovascular Repair
TTE	Transthoracic Echocardiography
UDF	User Defined Function
URF	Under Relaxation Factor
VENC	Velocity Encoding
VMTK	Vascular Modelling Toolkit
VSMC	Vascular Smooth Muscle Cells
WSS	Wall Shear Stress

ABSTRACT

I. Introduction

Aortic dissection (AD) is a life-threatening condition, characterized by a tear in the tunica intima and a false lumen in the tunica media through which blood can flow. ADs can be classified according to the Stanford classification, that distinguishes between type A dissections, which involve the ascending aorta, regardless of the origin location, and type B dissection that involve the aorta distal to the SCA. It is a dangerous pathology, that can lead to major complications such as aneurysm formation, aortic rupture, cardiac failure (acute aortic regurgitation, acute myocardial infarction, or cardiac tamponade) and end-organs ischaemia. At present, the mortality rate in the first 2 weeks after the onset of the symptoms increases by 1 to 3% per hour after presentation and is approximately 25% during the first 24 hours, 70% during the first week, and 80% at 2 weeks [1-3]. These percentage are the result of the lack of comprehension of the AD pathogenesis, which makes prevention and diagnosis difficult to be done. AD is the final stage of a multifactorial process that can involve different causes and conditions, like the hypertensions, the atherosclerosis and genetic pathologies that involve the aortic wall structure (Marfan syndrome, Loeys-Dietz syndrome… [3, 4]). This multifactorial process leads to a histological degeneration of the tunica media, usually characterized by the loss and fragmentation of elastic fibres, the loss of smooth muscle cells and the accumulation of proteoglycans in the medial layer of the aorta.

Numerous studies focused on finding a predictor that can help assessing which patients are at risk of AD initiation and propagation. Fluid-structure interaction (FSI) numerical simulations were demonstrated to be an effective tool to approach this problem as they allow to calculate hemodynamic and structural quantities and to find a correlation with the dissection pathology. It has been shown that elevated wall shear stresses (WSS) correspond to the location at which tear formation can occur, and that elevated peak wall stresses (PWS) increase the probability for AD development [5, 6]. Numerical simulations permit also to evaluate how these quantities of interest vary according to pathological conditions and aortic morphology; however little literature was found on the topic. Pasta et al. [7] demonstrated that subjects with bicuspid aortic valve (BAV) are more at risk of AD development due to the fact that more elevated PWS were measured for the bicuspid valve with respect to the tricuspid one. Campobasso et al. [8] assessed

that increasing the peripheral resistance significantly augments the PWS and the pressure values for stiff walls, meaning that the hypertensive condition is more dangerous for patients with a less compliant wall, such as those with an aneurysm. Chi et al. [6] noticed that higher aortic diameter, lower angles between aortic arch and supra-aortic vessels, and elevated tortuosity increase the WSS values and the probability for AD development. The mentioned studies are not sufficient to explore the relation between aortic hemodynamic and AD, a lot of aspects have still not been considered and others need further examination. This study aims at implementing multiple 2-way FSI simulations to assess the impact of different boundary conditions and different aortic arch geometries on the local stress concentrations and fluid disturbances that could facilitate AD formation and propagation. Two geometries of non-dilatated aortic vessels are considered, one presents the bovine arch configuration (the left common carotid artery departs form the brachiocephalic trunk) at the aortic arch while the other presents the common configuration. Three sets of boundary conditions will be applied for each geometry, i.e. the normotensive, the hypertensive and the hypotensive condition. A total of six simulations will be performed and compared.

II. Materials and methods

The simulations have been performed in ANSYS Workbench, applying ANSYS Fluent for fluid dynamic simulations and Mechanical APDL for the structural analysis. The solvers interact through the System Coupling component and the results were analysed by CFD-Post.

A mesh of approximately 700 thousand tetrahedral elements was chosen both for the common and the bovine arch configuration in the fluid dynamic domain, by means of a mesh sensitivity analysis. Five prism layers were implemented next to the wall in order to capture with higher accuracy the hemodynamic quantities of interest, which in this area are characterized by elevated gradient. The blood was modelled as a Newtonian, incompressible fluid with a density of 1060 kg/m^3 and a viscosity of 0.00319 Pa*s, which represent a typical value at normal hematocrit level (45%). The blood flow was assumed to be laminar, which is a commonly accepted simplification for large vessels where the average velocity results in relatively low Reynolds numbers.

The boundary conditions implemented for this study were obtained by a multi-dimensional model developed by Computational Life Inc, Delaware. This is an innovation introduced by this work thesis. Indeed, the gold standard at the moment is the use of patient-specific boundary conditions, or the imposition of a flow division between the descending aorta and the supra-aortic vessel based on the literature. The patient-specific boundary conditions guarantee the greatest adherence to reality possible but it can be difficult to obtain and process these data; on the other hand the flow division is very easy to model but represents a strong simplification of the system. The curves obtained by the Computational Life model can represent a good compromise to reproduce accurately the cardiovascular system without complicating excessively the process to obtain these boundary conditions. A flat time-varying velocity profile was imposed at the inlet, and a pressure time-varying profile was applied for each outlet (Figure I). The simulations were run for two cardiac cycles with a time step of 0.001 s. The duration of one cardiac cycle was normalized to 1 s, so that a total of 2000 time-steps were run to end one simulation. The results were extracted at the second cardiac cycle.

For the structural domain, a wall thickness of 2 mm was imposed, which was discretized through a single layer mesh of shell elements. In particular SHELL281 elements were chosen as they are ideal for non-linear applications characterized by large deformations. The meshes obtained were characterized by approximately 70 thousand and 100 thousand elements for the standard and the bovine arch configuration, respectively. The wall was modelled as an isotropic, incompressible, hyperelastic material with a density equal to 1120 kg/m^3. A Yeoh constitutive model was chosen, which is characterized by the following strain energy function:

$$\psi = C_{10}(I_1 - 3) + C_{20}(I_1 - 3)^2 \qquad \textbf{(1.1)}$$

were I_1 is the first invariant of the Cauchy-Green strain tensor, $C_{10} = 1.39\ MPa$ and $C_{20} = 0.5\ MPa$ are material parameters [9].

Two sub-steps for each time iteration were imposed, as a $\Delta t = 0.001\ s$ was not sufficient to guarantee the convergence of the structural domain. A Rayleigh numerical damping was introduced with $\alpha = 5650$ and $\beta = 0.1$, to enhance the convergence of the system. A fixed support was adopted at the inlet and the outlets, a fluid solid interface was defined on the surface to allow the interaction with the fluid domain, and a pressure of 52 mmHg was applied to the exterior surface to account for the constrain imposed by the surrounding tissues.

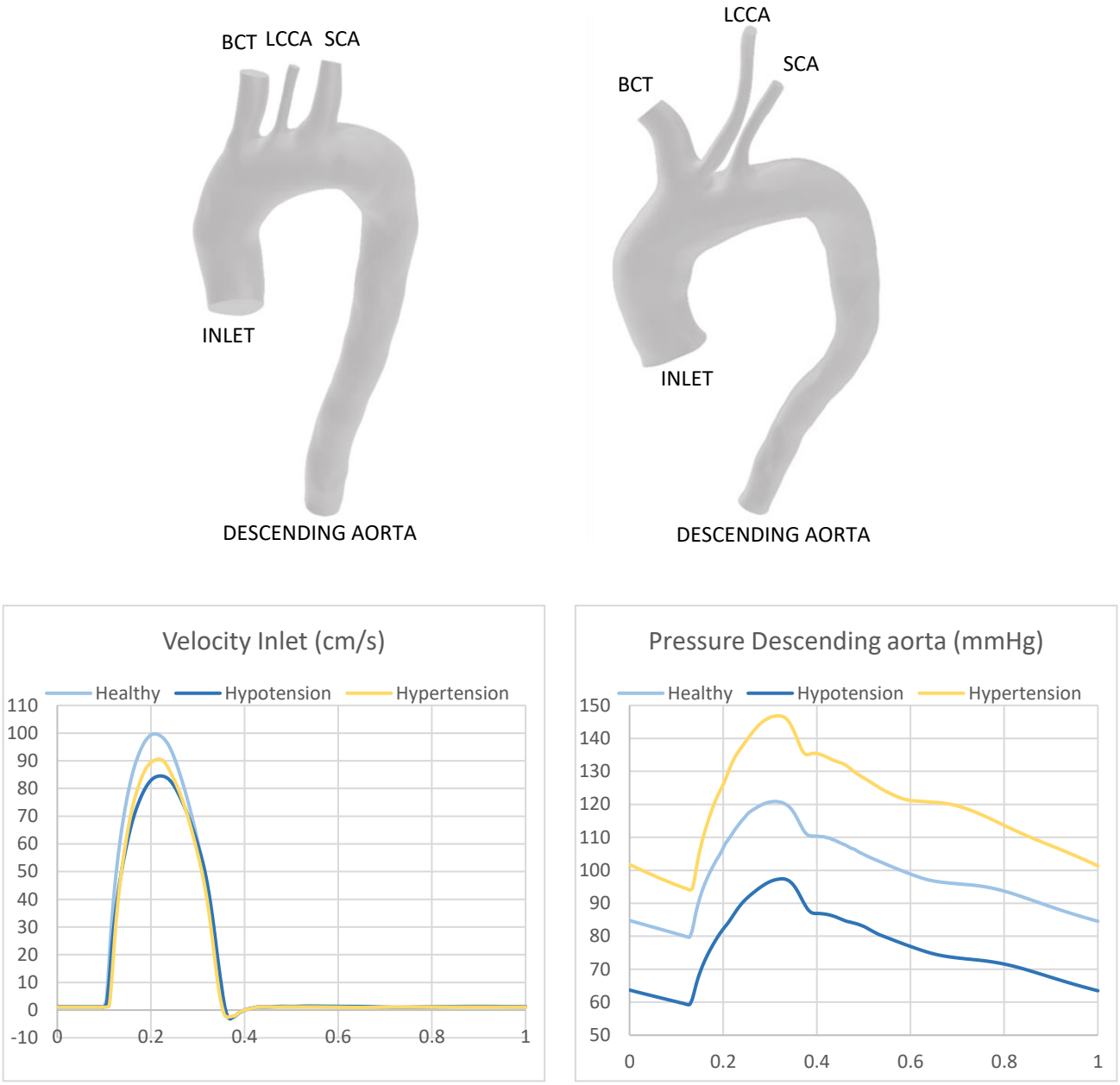

Figure I Boundary conditions imposed at the inlet and at the descending aorta.

With this set-up, the simulations reached the convergence with a run time around 5 to 7 days. The flow patterns, the WSS-based descriptors (Time average wall shear stress, oscillatory shear index and the relative residence) and the maximum principal stresses were extracted, computed and compared.

III. Results

Flow rate curves

The flow rate curves at the outlets have been plotted, in order to assess the resemblance of the physiological patterns, and to evaluate the differences generated by the various pressure conditions. The curves reproduce faithfully the pattern typical of the cardiac cycle, however the depth of the negative peak for the SCA and the LCCA is excessive being almost as high and as large as the systolic one.

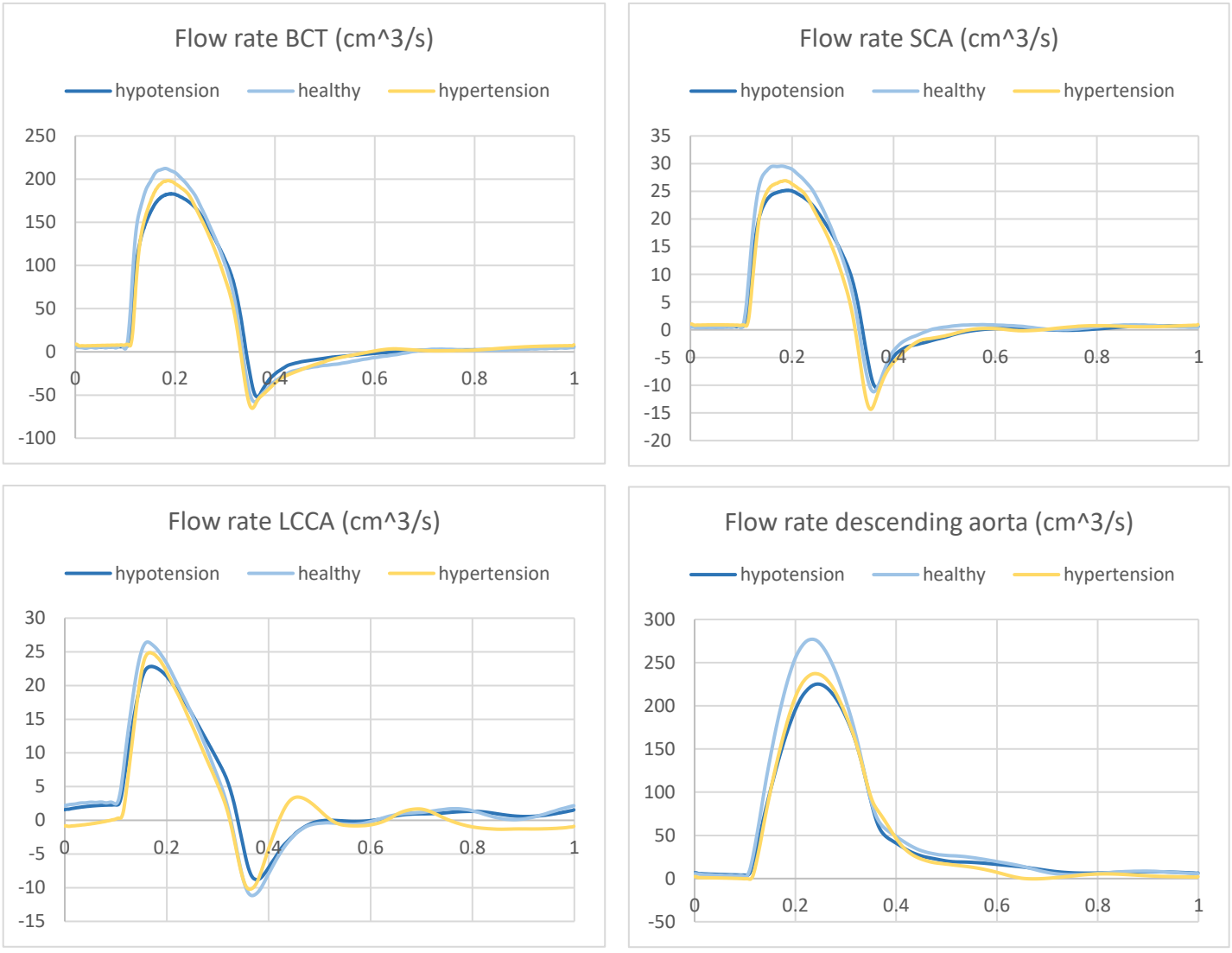

Figure II Flow rate plots for the bovine configuration for the three sets of boundary conditions.

The comparison among boundary conditions highlights that the hypertensive condition presents higher oscillatory patterns, especially at the LCCA. At the systolic peak, a decrease of 10-18% is measured for the hypotension curve with respect to the healthy one depending on the outlet considered for both configurations; for the hypertensive condition, instead, the decrement observed varies between approximately 4% and 17 % depending on the vessel analysed. It may seem surprising that the hypertension curve is lower than the healthy one, however the development of flow in the ascending aorta depends strongly on the afterload (or the resistance present in the systemic circulation), which is higher in the hypertensive case. In Figure II are reported the graphs for the bovine arch geometry.

Comparison results for different BCs

Looking at the results obtained for both the standard and the bovine arch configurations, some general considerations on the effects of the boundary conditions can be made.

Focusing on the fluid dynamic results, first it can be noticed that for the hypertension condition the flow is redirected toward the SCA, leading to higher velocity values in this area. In particular, for the standard configuration at the peak systole (t=0.4 s) there are few streamlines at the BCT, suggesting the flow encounters some difficulties in going through the first supra-aortic vessel, and an acceleration through the SCA (Figure III).

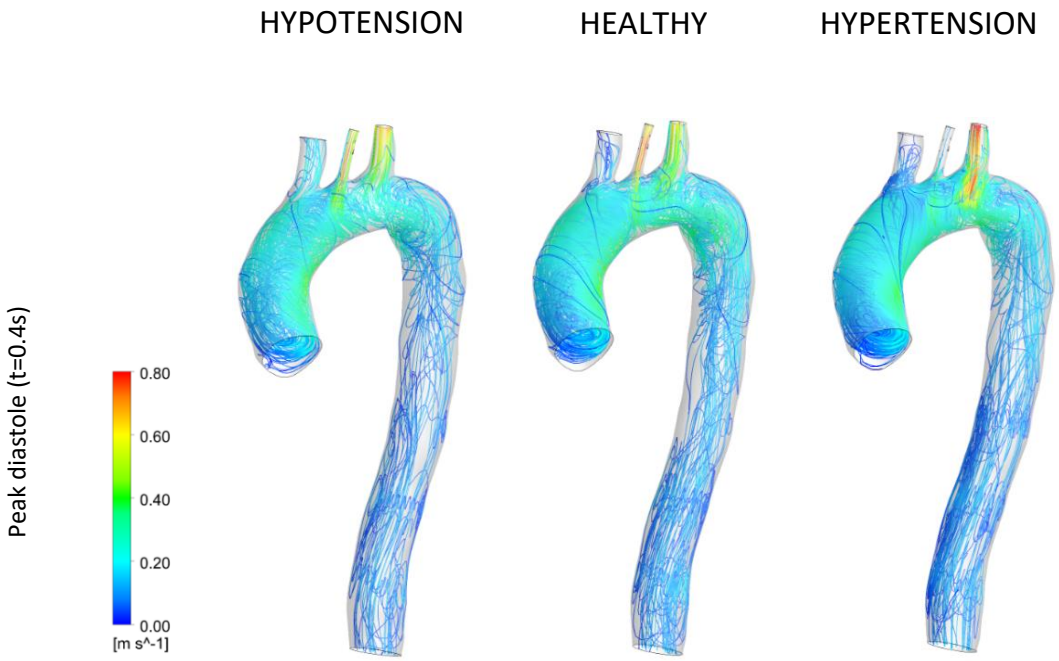

Figure III Flow patterns at the diastolic peak for the healthy configuration.

The time averaged wall shear stresses (TAWSS) are higher for the healthy case, consistently with the fact the velocity magnitude imposed for this pressure condition at the inlet is higher than in the other two cases, especially for the bovine arch configuration. Indeed, as shown in Table I, the mean value measure for the healthy condition is 14% and 17% higher than the hypertension and the hypotension case, respectively.

Pressure levels	**TAWSS**		**OSI**		**RRT**	
	Mean	Max	Mean	Max	Mean	Max
Hypotension	1.79	14.10	0.10	0.50	1.17	126.71
Healthy	2.10	17.24	0.09	0.49	0.97	64.88
Hypertension	1.73	15.08	0.11	0.49	1.25	107.12

Table I Mean and Maximum value WSS-based descriptors for the bovine arch configuration.

The extension of the areas characterized by elevated OSI values (maximum of 0.5) is larger for the hypertension condition, especially in correspondence of the SCA vessel. This is evident mostly for the standard configuration (Figure IV).

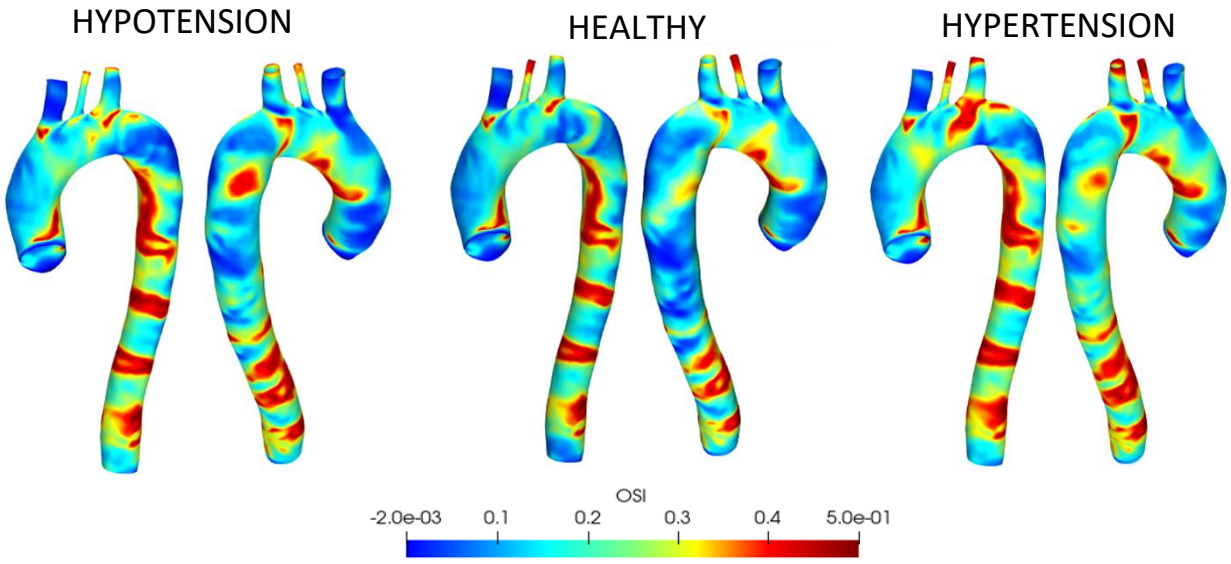

Figure IV OSI distribution for the standard configuration.

Looking at the structural result, a significant difference among the boundary conditions is seen in the maximum principal stress values. For the standard configuration, taken the healthy condition as baseline, a 44% decrease in the maximum value is observed for the hypotension condition and a 46% increment is measured for the hypertension one (Figure V). In the bovine

arch configuration instead, a decrease by 38% for the hypotension case and an increase by 37 % for the hypertensive one was observed. In both cases the difference is significant.

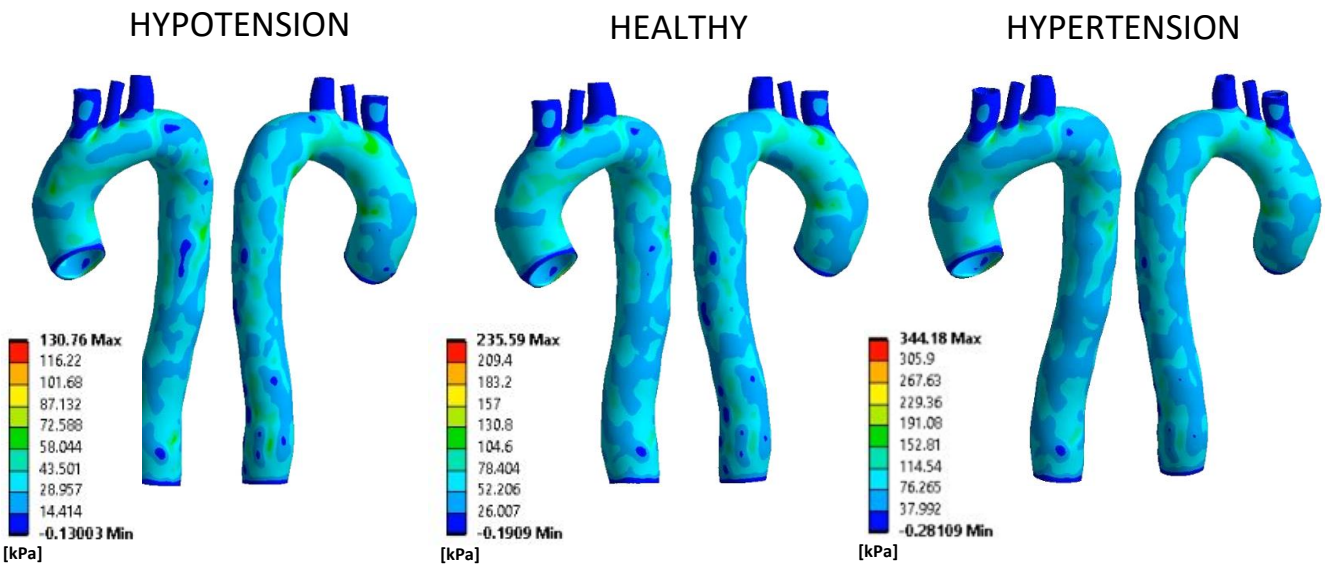

Figure V Maximum principal stress for the standard configuration.

The data collected suggest that the hypertension condition is the most dangerous one for AD initiation and propagation as it presents and larger area with high OSI and higher PWS.

Standard vs bovine configuration

The aortic arch configuration is shown to have an impact on the patterns of both hemodynamic and structural quantities.

At the diastolic peak (t=0.4 s) it can be seen a substantial difference in the organization of the flow patterns (Figure VI). In the standard configuration the flow tend to be more organized in the ascending aorta to then disrupt into recirculation patterns in the descending aorta, in the bovine arch case instead an opposite behaviour is observed, which present disturbed flow in the ascending aorta and more organized streamlines at the descending one. It is believed that the lack of the bifurcation in the last part of the aortic arch has a role in favouring a more organized flow in the descending aorta of the bovine arch configuration.

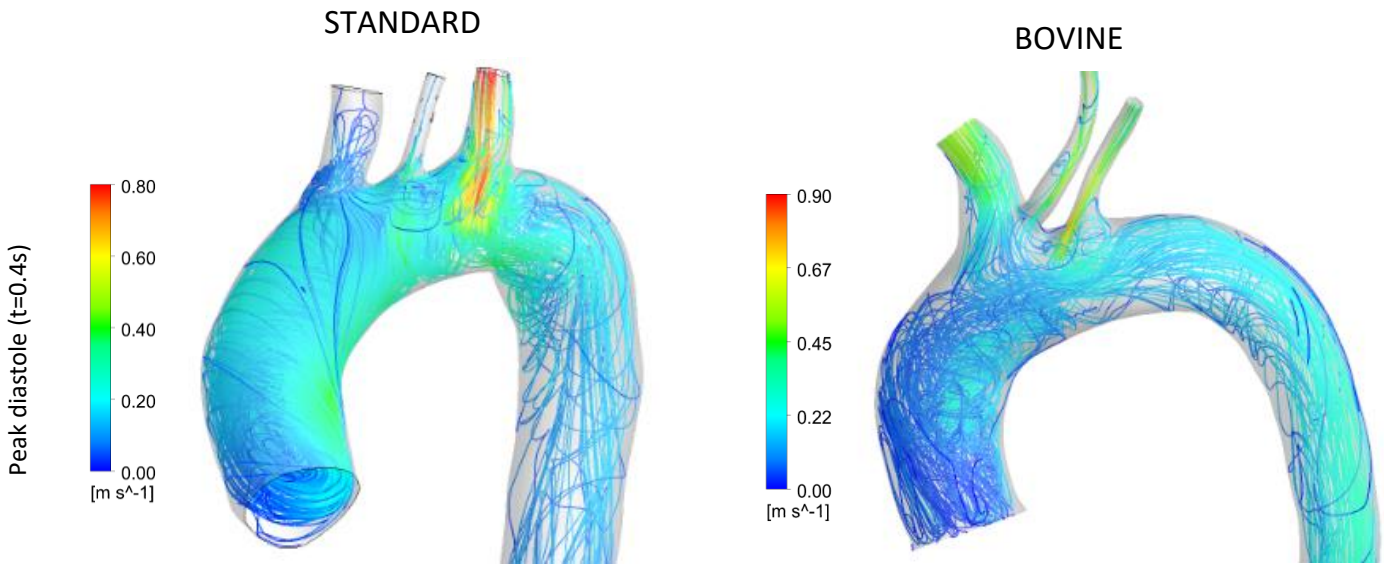

Figure VI Flow patterns for the two configurations at diastolic peak.

Also, Table II shows that the geometry influences the flow rate distribution through the supra-aortic vessels. No big differences are shown in the output of the LCCA, while there is a clear increment of the flow through the BCT and a reduction in the SCA, moving from the standard to the bovine configuration.

Artery	**Flow rate (%)**	
	Standard	Bovine
BCT	26.24	37.63
LCCA	3.79	4.24
SCA	12.95	5.27

Table II Flow rate percentage at the supra-aortic vessels

To compare the hemodynamic descriptors between the two configurations, the geometries were divided in patches through the use of VMTK. The value associated to each patch is calculated as the mean of the values at the nodes belonging to the patch itself. The bovine arch configuration presents more elevated TAWSS value at the descending aorta, at the distal portion of the BCT and throughout the length of the SCA. Both configurations instead are characterized by elevated values where the bifurcation of the BCT and the SCA occur.

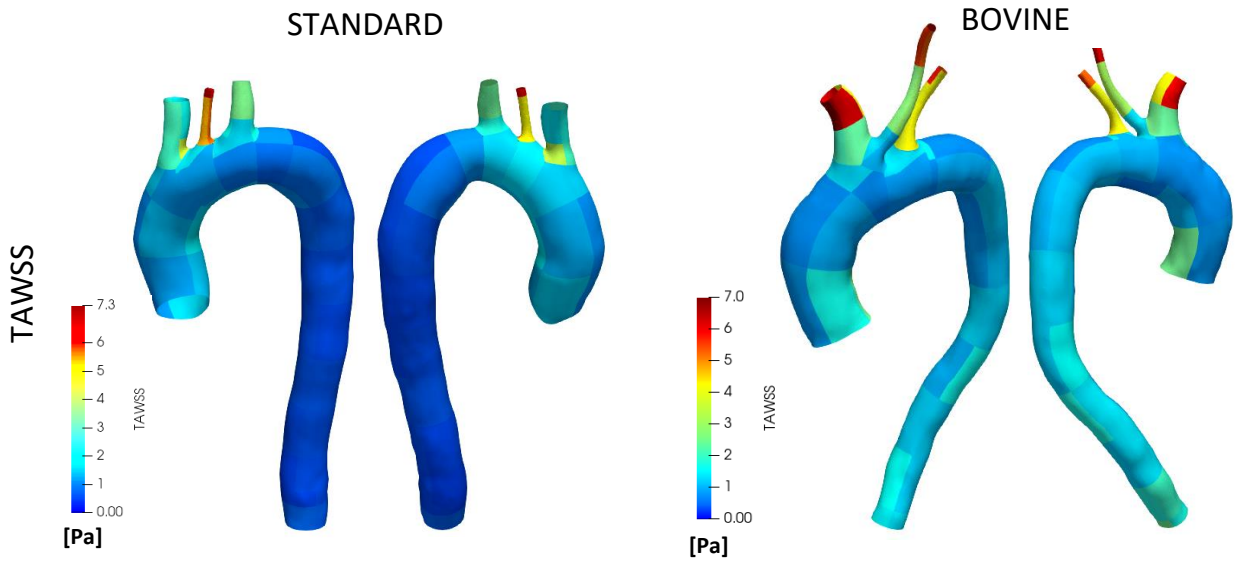

Figure VII TAWSS values calculated on patches for the two configurations.

The OSI distribution is specular for the two configurations, as the standard aortic arch shows OSI peak values in correspondence of the descending aorta, while the bovine configuration shows higher values in the ascending aorta. However elevated OSI values are measured for both configurations in correspondence of the patches next to the SCA and the BCT entrances.

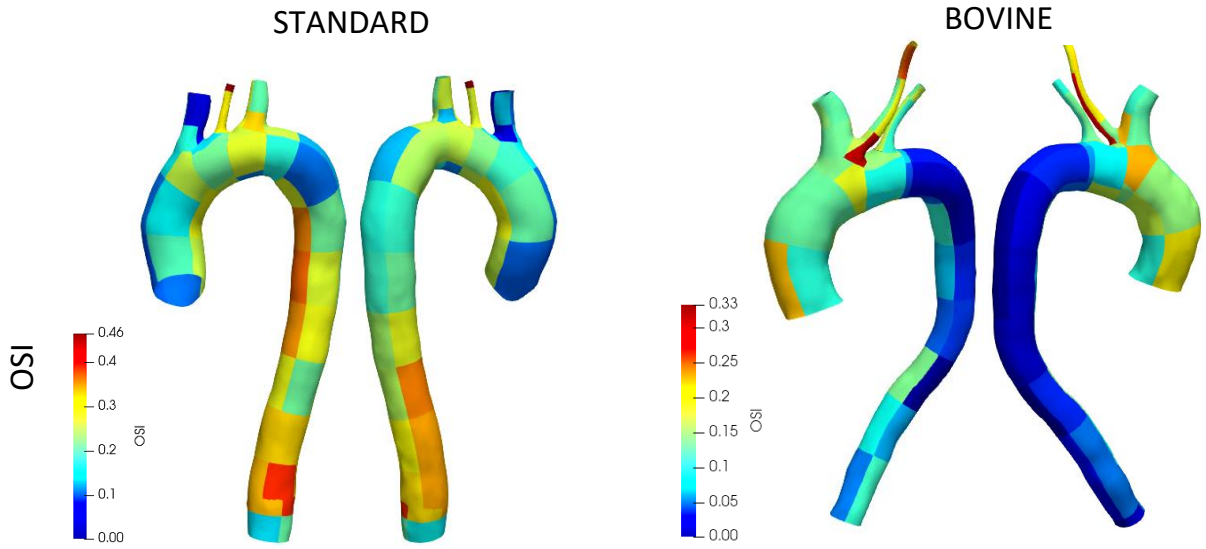

Figure VIII OSI values calculated on patches for the two configurations.

Looking at the structural results, for the standard case a peak value is registered only at the entrance of the BCT vessel, while the bovine arch configuration presents a maximum also at the ascending aorta and at the mid descending one. The maximum value reached by the bovine arch geometry is much lower than the one obtained for the standard configuration: a percentage difference of 34% is measured between the two configurations. This suggests that the standard configuration has overall a higher probability for the AD to propagate.

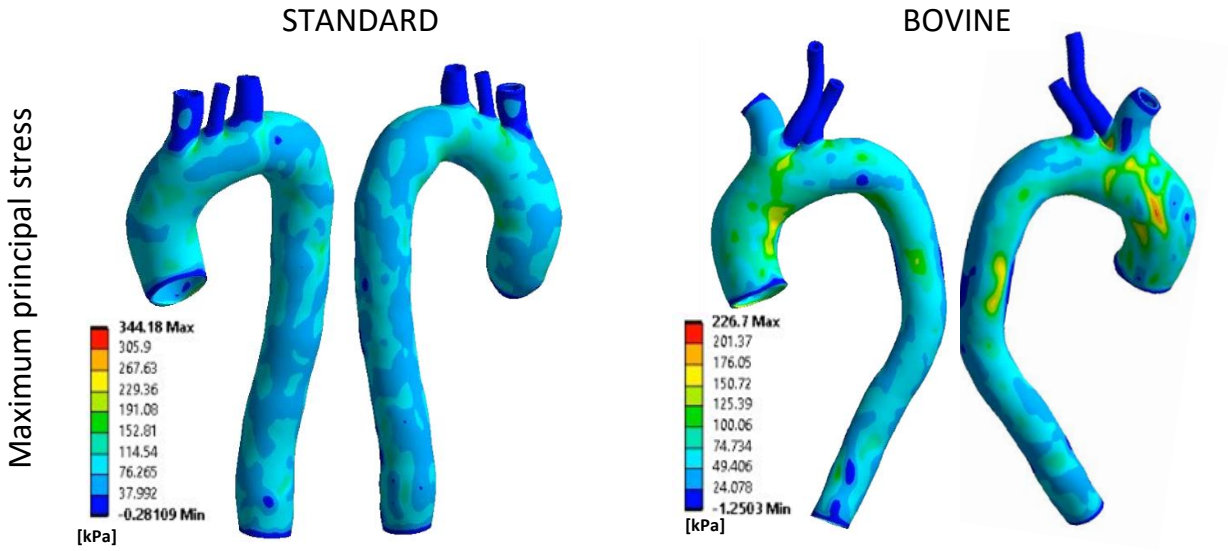

Figure IX Maximum principal stresses for the two configurations.

The comparison between the two configurations suggests that the bovine arch geometry has a higher probability to develop type B AD, and that the standard configuration has a higher probability for AD to develop if tear formation occurs.

IV. Conclusions

In this work thesis, 2-way FSI simulations were implemented in order to assess the influence of different pressure conditions and geometry configuration on the location at which the AD could initiate and propagate. The results obtained suggest the variation of the BCs affect the probability for the aortic vessel to experience the dissection pathology. The hypertension case is observed to be the riskiest condition for the AD pathology, which is in accordance with the clinical data. Regarding the impact of the aortic arch geometry, significant differences are observed in the flow patterns and in the WSS based descriptor distribution. It can be stated that

the standard configuration retains a higher probability for the AD to initiate at the posterior wall of the ascending aorta, at the bifurcation area of the BCT and the SCA, and at the LCCA vessel. In the bovine arch configuration, instead, tear formation has a higher probability to occur in correspondence of the bifurcations of the supra-aortic vessel or at the distal the descending aorta. This study is affected by some limitations, such as the choice of using an isotropic model for the structural domain or the impossibility to compare the results with the clinical outcome of the patients. This opens the possibility for further investigation.

V. Bibliography

[1] Kurz SD, Falk V, Kempfert J, Gieb M, Ruschinski TM, Kukucka M, Tsokos M, Grubitzsch H, Herbst H, Semmler J, Buschmann C. Insight into the incidence of acute aortic dissection in the German region of Berlin and Brandenburg. International journal of cardiology 2017; 241: 326-329

[2] Criado FJ. Aortic dissection: a 250-year perspective. Texas Heart Institute journal 2011; 38: 694-700

[3] Khan IA, Nair CK. Clinical, Diagnostic, and Management Perspectives of Aortic Dissection. Chest 2002; 122: 311-328

[4] Nienaber CA, Clough RE, Sakalihasan N, Suzuki T, Gibbs R, Mussa F, Jenkins MP, Thompson MM, Evangelista A, Yeh JS. Aortic dissection. Nature Reviews Disease Primers 2016; 2: 1-18

[5] Khanafer K, Berguer R. Fluid–structure interaction analysis of turbulent pulsatile flow within a layered aortic wall as related to aortic dissection. Journal of Biomechanics 2009; 42: 2642-2648

[6] Chi Q, He Y, Luan Y, Qin K, Mu L. Numerical analysis of wall shear stress in ascending aorta before tearing in type A aortic dissection. Computers in biology and medicine 2017; 89: 236-247

[7] Pasta S, Rinaudo A, Luca A, Pilato M, Scardulla C, Gleason TG, Vorp DA. Difference in hemodynamic and wall stress of ascending thoracic aortic aneurysms with bicuspid and tricuspid aortic valve. Journal of Biomechanics 2013; 46: 1729-1738

[8] Campobasso R, Condemi F, Viallon M, Croisille P, Campisi S, Avril S. Evaluation of peak wall stress in an ascending thoracic aortic aneurysm using FSI simulations: effects of aortic stiffness and peripheral resistance. Cardiovascular engineering and technology 2018; 9: 707-722

[9] Gasbarro MD, Shimada K, Di Martino ES. Mechanics of abdominal aortic aneurysm. European Journal of Computational Mechanics/Revue Européenne de Mécanique Numérique 2007; 16: 337-363

SOMMARIO

I. Introduzione

La dissezione aortica (AD) è una patologia pericolosa, caratterizzata da una ferita nella tunica intima e da un falso lume nella tunica media attraverso il quale il sangue può fluire. Le dissezioni possono essere classificate secondo la classificazione di Stanford, che distingue tra le dissezioni di tipo A, che coinvolgono l'aorta ascendente indipendentemente dalla posizione di origine, e la dissezione di tipo B che coinvolgono l'aorta discendente. È una patologia che può portare a complicazioni come la formazione di aneurisma, la rottura aortica, l'insufficienza cardiaca (rigurgito aortico acuto, infarto miocardico acuto o tamponamento cardiaco) e l'ischemia degli organi. Attualmente, il tasso di mortalità nelle prime 2 settimane dopo l'insorgenza dei sintomi aumenta dell'1-3% all'ora ed è di circa il 25% durante le prime 24 ore, del 70% durante la prima settimana e dell'80% a 2 settimane [1-3]. Queste percentuali sono il risultato della mancanza di comprensione della patogenesi dell'AD, che rende difficile la prevenzione e la diagnosi. L'AD è la fase finale di un processo multifattoriale che può coinvolgere diverse cause e condizioni, come l'ipertensione, l'aterosclerosi e alcune patologie genetiche che coinvolgono la struttura della parete (sindrome di Marfan, sindrome di Loeys-Dietz... [3, 4]). Questo processo porta ad una degenerazione istologica della tunica intima, solitamente caratterizzato dalla perdita e frammentazione delle fibre elastiche, dalla perdita di cellule muscolari lisce e dall'accumulo di proteoglicani nello tunica media dell'aorta.

Numerosi studi si sono concentrati sulla ricerca di un predittore che possa aiutare a valutare quali pazienti sono a rischio di iniziazione e propagazione dell'AD. Le simulazioni numeriche di interazione fluido-struttura (FSI) si sono dimostrate uno strumento efficace per affrontare questo problema in quanto consentono di calcolare quantità emodinamiche e strutturali e di trovare una correlazione con la AD. È stato dimostrato che l'elevata sollecitazione di taglio alla parete (WSS) corrisponde alla posizione in cui può verificarsi la lacerazione [5, 6] e che elevati valori dei massimi sforzi principali misurati alla parete (PWS) aumentano la probabilità di sviluppo dell'AD [5, 6]. Le simulazioni numeriche permettono anche di valutare come queste quantità di interesse variano a seconda delle condizioni patologiche e della morfologia aortica; tuttavia, poca letteratura è disponibile sull'argomento. Pasta et al. [7] hanno dimostrato che i

soggetti con valvola aortica bicuspide (BAV) sono più a rischio di sviluppo dell'AD, poiché i PWS misurati sono più elevati rispetto a quelli nei soggetti con valvola tricuspide. Campobasso et al. [8] hanno documentato che aumentare significativamente la resistenza periferica aumenta i PWS e i valori di pressione per pareti con elevata rigidità, il che significa che la condizione ipertensiva è più pericolosa per i pazienti la cui parete presenta una minore compliance, tra i quali si evidenziano i pazienti con aneurisma. Chi et al. [6], invece, notarono che un diametro aortico più elevato, angoli più bassi tra archi aortici e vasi sopra-aortici, e un'elevata tortuosità aumentano i valori WSS e la probabilità di sviluppo dell'AD. Gli studi citati non sono sufficienti per esplorare la relazione tra emodinamica aortica e AD, molti aspetti non sono ancora stati presi in considerazione e altri hanno bisogno di ulteriori esami. Questo studio mira ad implementare simulazioni FSI di tipo 2-way per valutare l'impatto di diverse condizioni al contorno e diverse geometrie dell'arco aortico sulle concentrazioni degli stress locali e sui disturbi fluidodinamici che potrebbero facilitare la formazione e la propagazione dell'AD. Vengono prese in considerazione due tipologie di arco aortico, una con configurazione ad arco bovino (la carotide comune sinistra parte dal tronco brachiocefalico) mentre l'altra con la configurazione standard. Per ogni geometria verranno applicati tre differenti condizioni al contorno, ovvero la normotensiva, l'ipertensiva e l’ipotensiva. Sono state eseguite e confrontate in totale sei simulazioni.

II. Materiali e metodi

Le simulazioni sono state eseguite in ANSYS Workbench, applicando ANSYS Fluent per simulazioni fluidodinamiche e Mechanical APDL per l'analisi strutturale. I risolutori interagiscono attraverso il componente System Coupling e i risultati sono stati analizzati da CFD-Post.

Una mesh tetraedrica di circa 700 mila elementi è stata scelta sia per la configurazione comune che per la configurazione dell'arco bovino nel dominio fluidodinamica, attraverso un'analisi di sensibilità. Cinque strati con elementi prismatici sono stati implementati accanto alla parete al fine di catturare con maggiore precisione le quantità emodinamiche di interesse, che in quest'area sono caratterizzate da un gradiente elevato. Il sangue è stato modellato come un fluido newtoniano incomprimibile con una densità di 1060 kg/m^3 e una viscosità di 0,00319

Pa*s, che rappresentano un valore tipico a livello di ematocrito normale (45%). Si presume che il flusso sanguigno sia laminare, che è una semplificazione comunemente accettata per i grandi vasi dove la velocità media si traduce in numeri di Reynolds relativamente bassi. Le condizioni al contorno implementate per questo studio sono state ottenute da un modello multidimensionale sviluppato da Computational Life Inc, Delaware, il che rappresenta un elemento innovativo introdotto da questo lavoro di tesi. Infatti, al momento il gold standard è l'uso di condizioni al contorno specifiche per il paziente, o l'imposizione di una divisione del flusso tra l'aorta discendente e il vaso sopra-aortico basato sulla letteratura. Le condizioni al contorno specifiche del paziente garantiscono la massima aderenza possibile alla realtà ma può essere difficile ottenere ed elaborare questo tipo di dati; al contrario la divisione del flusso è molto facile da modellare ma rappresenta una forte semplificazione del sistema. Le curve ottenute dal modello di Computational Life Inc, Delaware, possono rappresentare un buon compromesso per riprodurre accuratamente il sistema cardiovascolare senza complicare eccessivamente il processo per ottenere le condizioni al contorno. All'inlet è stato imposto un profilo di velocità piatto variabile nel tempo ed è stato applicato un profilo variabile nel tempo di pressione per ogni uscita. Le simulazioni sono state eseguite per due cicli cardiaci con un time-step di 0,001 s. la durata di un ciclo cardiaco è stata normalizzata a 1 s, in modo che un totale di 2000 time-step sono stati eseguiti per terminare una simulazione. I risultati sono stati estratti al secondo ciclo cardiaco.

Per il dominio strutturale, è stato imposto uno spessore della parete di 2 mm, che è stato discretizzato attraverso una mesh caratterizzata da un singolo strato di elementi shell. In particolare sono stati scelti elementi SHELL281 in quanto ideali per applicazioni non lineari caratterizzate da grandi deformazioni. Le mesh ottenute sono caratterizzate da circa 70 mila e 100 mila elementi, rispettivamente per la configurazione standard e per l'arco bovino. La parete è stata modellata come un materiale isotropo, incomprimibile, iperelastico con una densità pari a 1120 kg/m$^{3.}$ È stato scelto un modello costitutivo di Yeoh, che è caratterizzato dalla seguente funzione di energia di deformazione:

$$\psi = C_{10}(I_1 - 3) + C_{20}(I_1 - 3)^2 \qquad \textbf{(1.1)}$$

dove I_1 è il primo invariante del tensore di deformazione Cauchy-Greene, $C_{10} = 1.39\ MPa$ e $C_{20} = 0.5\ MPa$ sono parametri del materiale [9].

Sono stati imposti due ulteriori steps per ogni iterazione, in $s$quanto un $\Delta t = 0.001\ s$ non era sufficiente a garantire la convergenza dell'analisi strutturale. È stato introdotto uno smorzamento numerico di Rayleigh con $\alpha = 5650$ e $\beta = 0.1$, per migliorare la convergenza del sistema. Un supporto fisso è stato adottato all'ingresso e alle uscite, un'interfaccia solido-fluido è stata definita sulla superficie per consentire l'interazione con il dominio del fluido, e una pressione di 52 mmHg è stata applicata sulla superficie esterna per tenere conto del vincoli imposti dai tessuti circostanti.

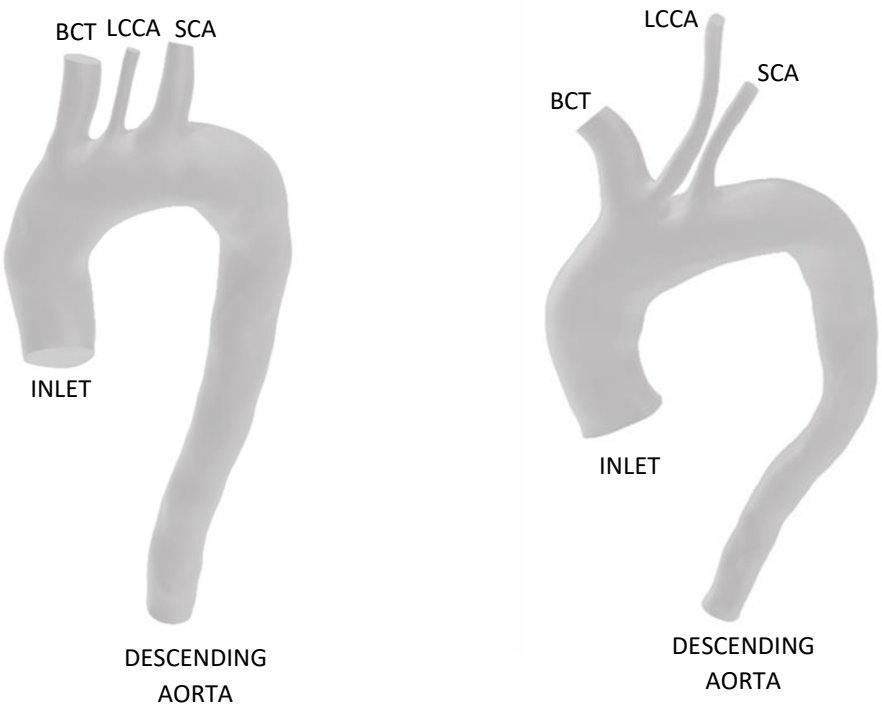

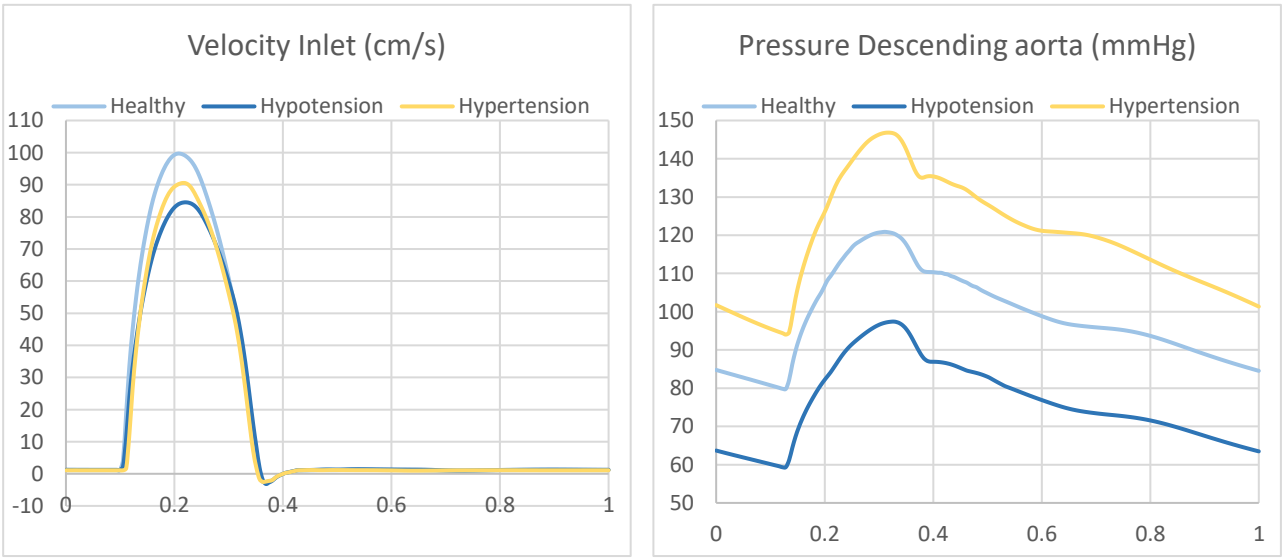

figura X condizioni al contorno imposte all'inlet e all'aorta discendente.

Con questo set-up, le simulazioni hanno raggiunto la convergenza con un tempo di esecuzione di circa 5-7 giorni. I modelli di flusso, i descrittori basati su WSS (time average wall shear stress, oscillatory shear index e il relative residence time) e gli stress principali massimi sono stati estratti, calcolati e confrontati.

III. Risultati

Grafici della portata

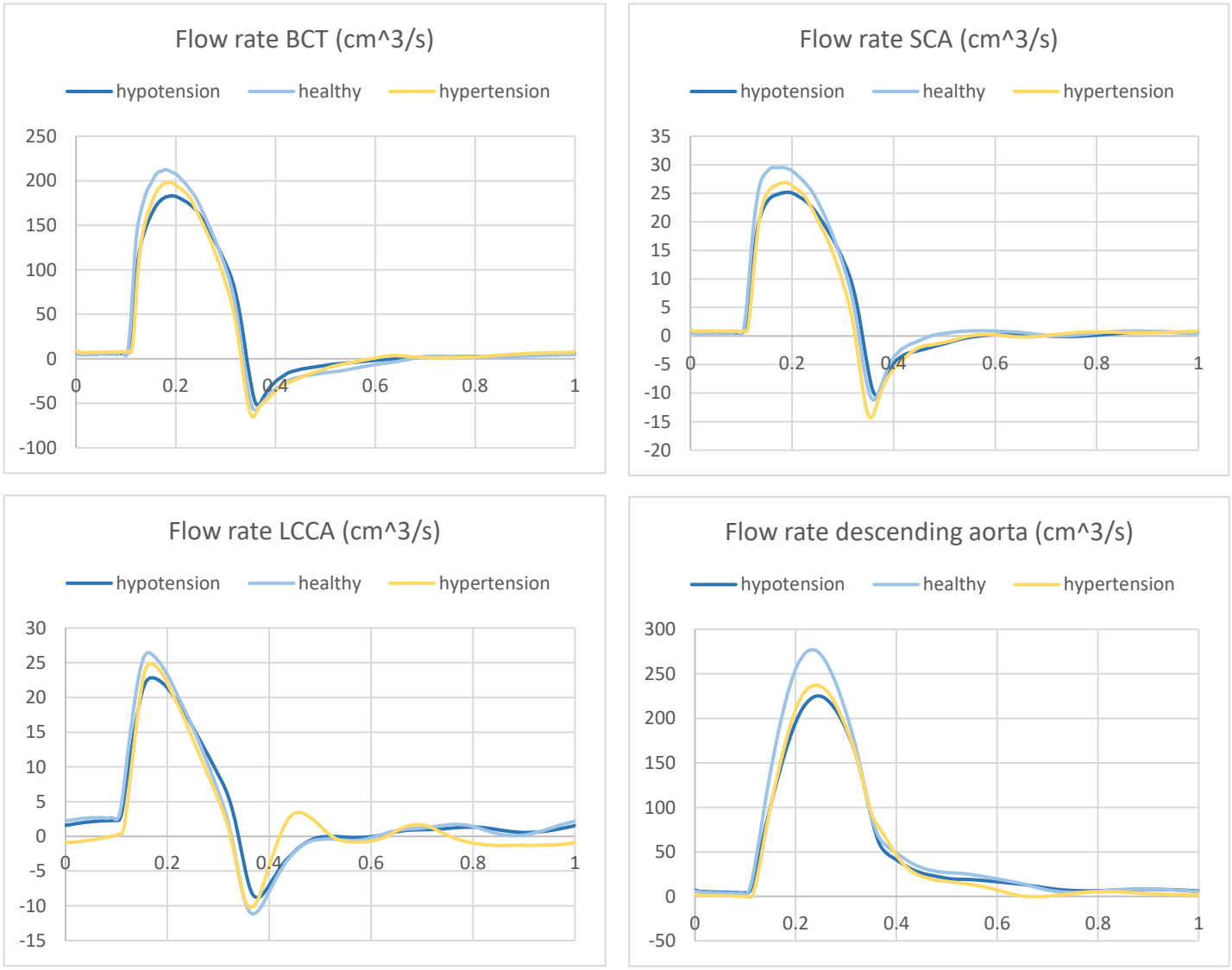

Figura XI Grafici della portata per la configurazione bovina per le tre condizioni al contorno.

Sono state tracciate le curve di portata agli outlet, al fine di valutare la somiglianza coi modelli fisiologici e di valutare le differenze generate dalle varie condizioni di pressione. Le curve riproducono fedelmente la forma tipica osservata durante il ciclo cardiaco, tuttavia la profondità del picco negativo per la SCA e la LCCA è eccessiva essendo quasi profonda e larga quanto quella del picco sistolico. Il confronto tra le condizioni limite evidenzia che la condizione ipertensiva presenta pattern oscillatori più elevati, specialmente per LCCA. Al picco sistolico per entrambe le configurazioni, viene misurata una diminuzione del 10-18% della curva di ipotensione rispetto a quella sana a seconda dell'outlet considerato; per la condizione ipertensiva, invece, il decremento osservato varia tra il 4% e il 17 % circa a seconda dell'outlet analizzato. Può sembrare sorprendente che la curva di ipertensione sia inferiore a quella sana, tuttavia lo sviluppo del flusso nell'aorta ascendente dipende fortemente dal post-carico (o dalla resistenza presente nella circolazione sistemica), che è più alto nel caso ipertensivo.

Confronto risultati per differenti BCs

Esaminando i risultati ottenuti sia per la configurazione standard che per la configurazione ad arco bovino, è possibile fare alcune considerazioni generali sugli effetti delle condizioni al contorno.

Concentrandosi sui risultati fluidodinamici, la prima cosa che si può notare è che per l'ipertensione il flusso viene reindirizzato verso la SCA, portando a valori di velocità più elevati in quest'area. In particolare, per la configurazione standard al picco sistolico (t=0,4 s), ci sono poche linee di flusso al BCT, suggerendo che il flusso incontra alcune difficoltà nel passare attraverso il primo vaso sopra-aortico, e un'accelerazione attraverso la SCA.

Figura XII Pattern di flusso al picco diastolico per la configurazione sana.

I TAWSS sono più elevati per il caso sano, in linea con il fatto che la velocità imposta per questa condizione di pressione all'ingresso è più alta rispetto agli altri due casi, specialmente per la configurazione dell'arco bovino. Infatti, come mostrato in ..., la misura del valore medio per la condizione sana è rispettivamente del 14% e del 17% superiore al valore misurato nel caso dell'ipertensione e dell'ipotensione.

Livelli pressione	**TAWSS**		**OSI**		**RRT**	
	Mean	Max	Mean	Max	Mean	Max
Ipotensione	1.79	14.10	0.10	0.50	1.17	126.71
Sano	2.10	17.24	0.09	0.49	0.97	64.88
Ipertensione	1.73	15.08	0.11	0.49	1.25	107.12

Tabella I Valore medio e massimo dei descrittori basati su WSS di per la configurazione ad arco bovino.

L'estensione delle aree caratterizzate da valori massimi del OSI è maggiore per le condizioni di ipertensione, specialmente in corrispondenza del vaso SCA. Ciò è evidente soprattutto per la configurazione standard.

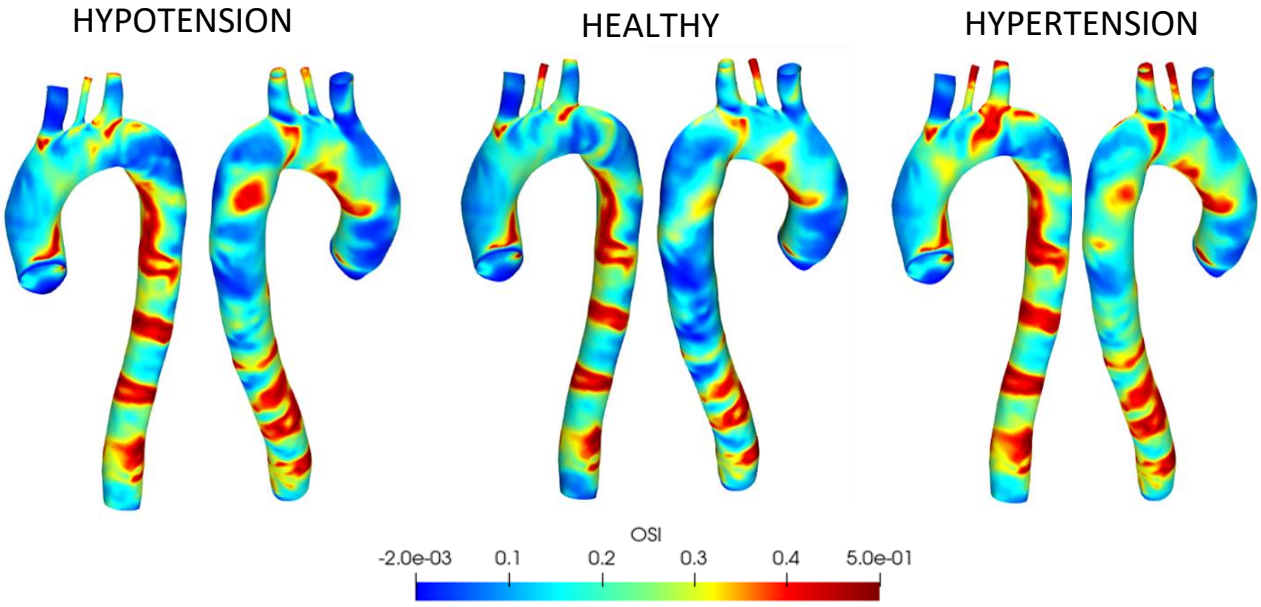

Figura XIII OSI per la configurazione standard.

Analizzando i risultati strutturali, una differenza significativa tra i risultati ottenuti per le diverse le condizioni al contorno, è nei valori dei PWS. Per la configurazione standard, presa la condizione sana come baseline, si osserva una diminuzione del 44% del valore massimo per la condizione di ipotensione e un incremento del 46% per quello dell'ipertensione. Nella configurazione ad arco bovino, invece, si osserva una diminuzione del 38% per il caso di ipotensione e un aumento del 37 % per quello ipertensivo. In entrambi i casi la differenza è significativa.

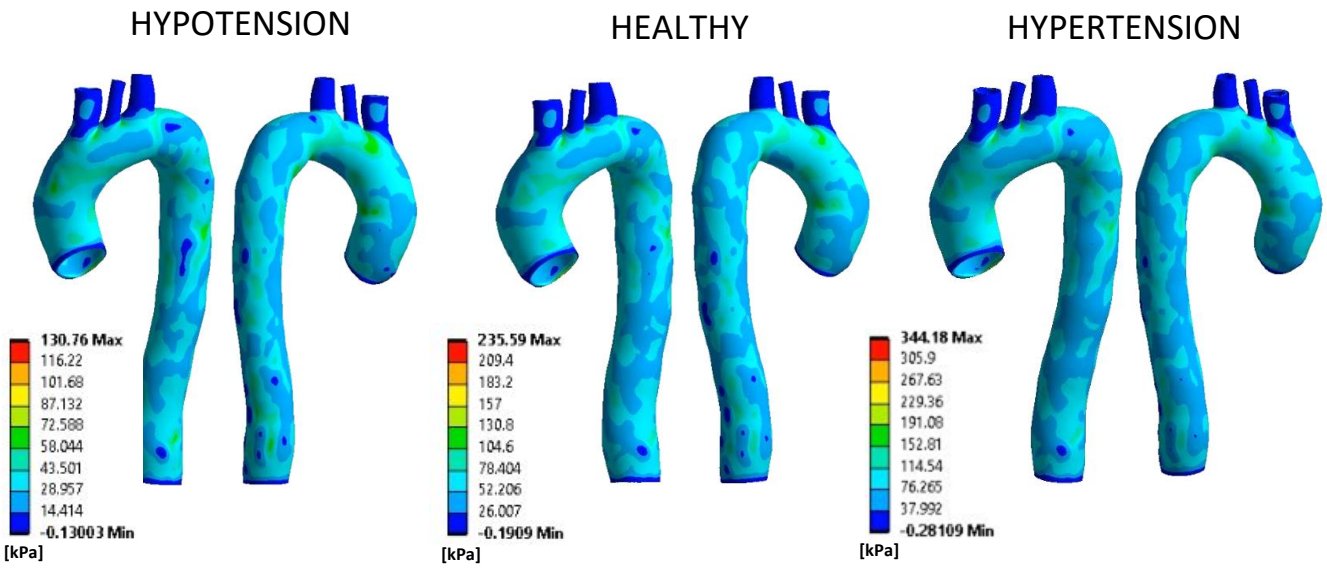

Figura XIV stress principali massimi per la configurazione standard.

I dati raccolti suggeriscono che la condizione di ipertensione è la più pericolosa per la formazione e la propagazione dell'AD, in quanto è caratterizzata da un'area più ampia con OSI massimo e da PWS più elevati.

Configurazione standard vs configurazione bovina

Si dimostra che la configurazione dell'arco aortico ha un impatto sui pattern delle quantità di interesse sia emodinamiche che strutturali.

Al picco diastolico (t=0,4 s) si può vedere una differenza sostanziale nell'organizzazione del flusso sanguigno. Nella configurazione standard il flusso tende ad essere più organizzato nell'aorta ascendente per poi creare ricircoli nell'aorta discendente, nel caso dell'arco bovino invece si osserva un comportamento opposto, con flusso disturbato nell'aorta ascendente che diventa più organizzato nel tratto discendente. Si ritiene che la mancanza di biforcazioni

nell'ultima parte dell'arco aortico abbia un ruolo nel favorire un flusso più organizzato nell'aorta discendente nella configurazione ad arco bovino.

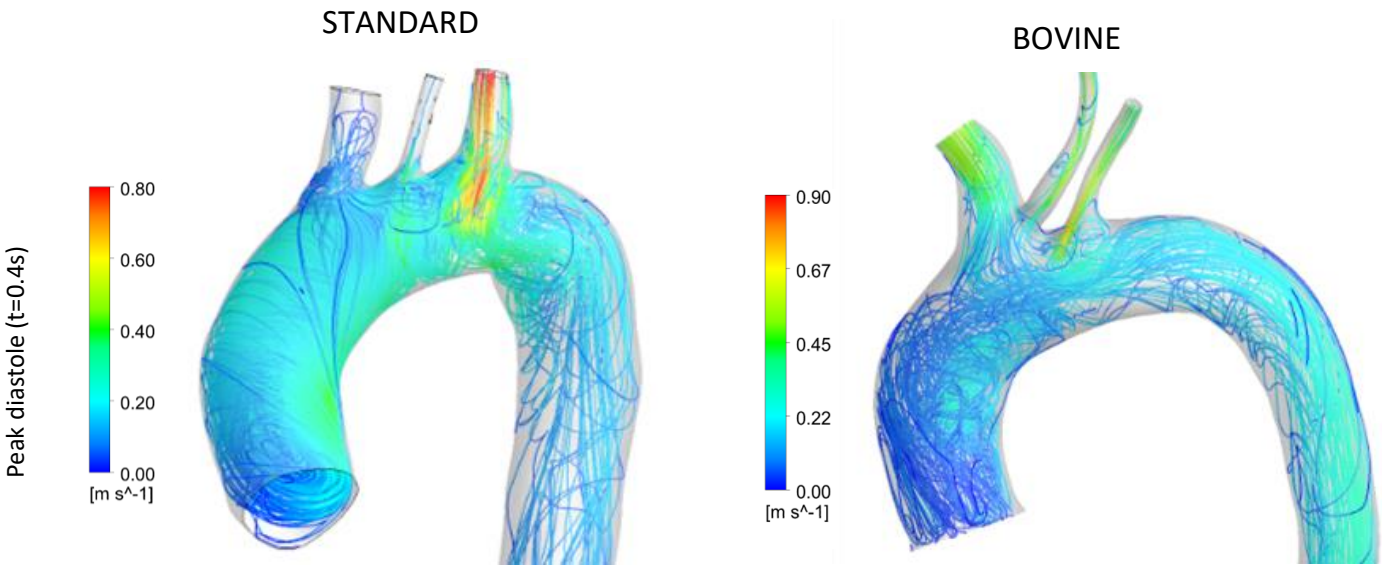

Figura XV Pattern di flusso per le due configurazioni al picco diastolico.

Inoltre, la Tabella II mostra che la geometria influenza la distribuzione della portata attraverso i vasi sopra-aortici. Non si notano grandi differenze per la LCCA, mentre vi è un chiaro incremento del flusso attraverso il BCT e una riduzione della SCA, passando dalla configurazione standard a quella bovina.

Arteria	**Flow rate (%)**	
	Standard	Bovine
BCT	26.24	37.63
LCCA	3.79	4.24
SCA	12.95	5.27

Tabella II Percentuale della portata nei vasi sovra-aortici.

Per confrontare i descrittori emodinamici tra le due configurazioni, le geometrie sono state divise in patch attraverso l'uso di VMTK. Ad ogni patch è associato un valore, calcolato facendo la media dei dati associati ai nodi appartenenti alla patch. La configurazione ad arco bovino presenta un valore TAWSS più elevato all'aorta discendente, alla porzione distale della BCT e per tutta la lunghezza della SCA. Per entrambe le configurazioni invece si registrano valori elevati in corrispondenza della biforcazione del BCT e della SCA. La distribuzione OSI è speculare per le due configurazioni, poiché l'arco aortico standard mostra valori di picco OSI in corrispondenza dell'aorta discendente, mentre la configurazione bovina presenta valori più alti nell'aorta ascendente. Entrambe le configurazioni hanno valori OSI elevati in corrispondenza delle patch accanto alla SCA e agli ingressi BCT.

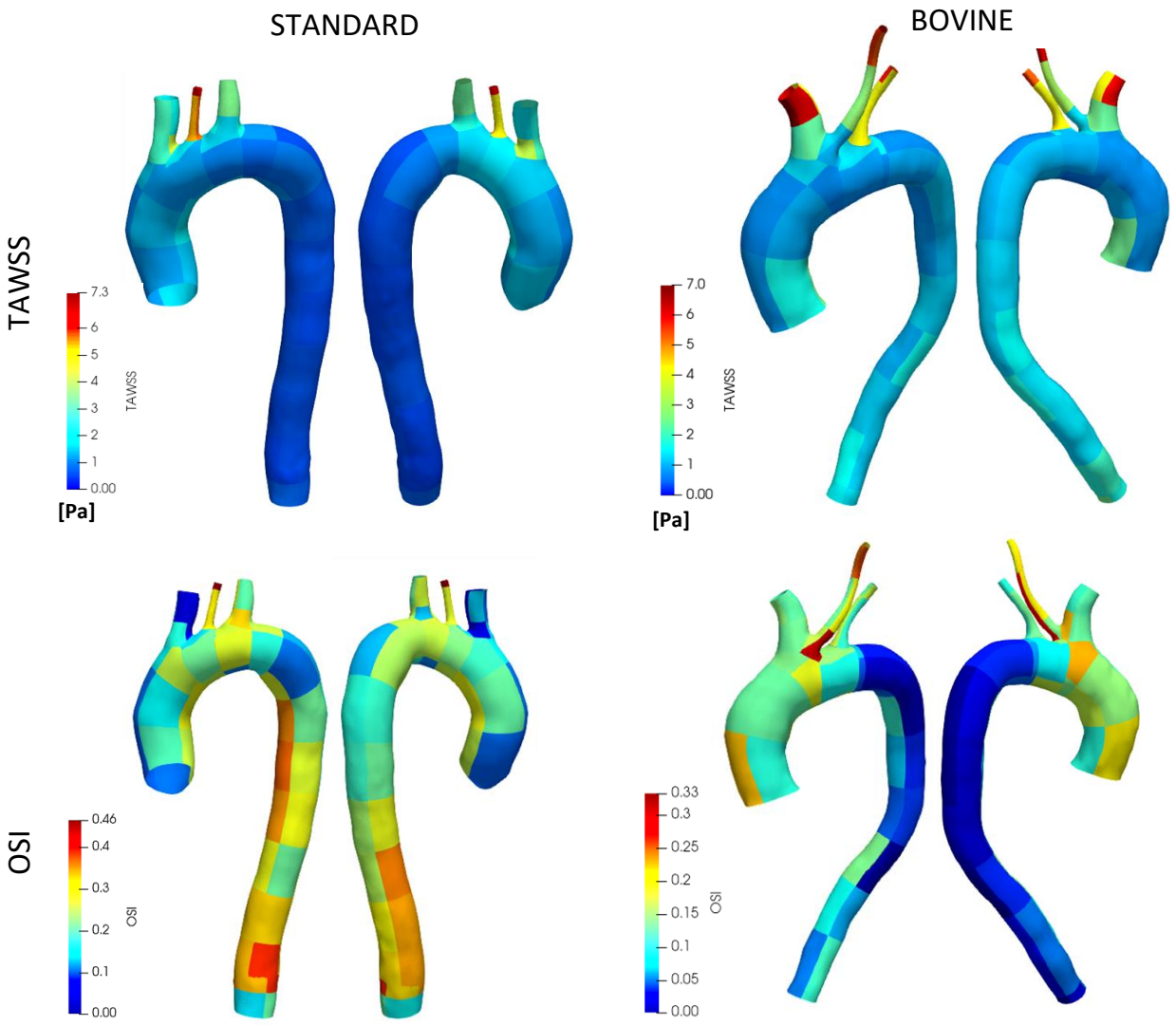

Esaminando i risultati strutturali, nel caso standard il valore massimo si osserva solo all'ingresso del BCT, mentre la configurazione ad arco bovino ha un massimo anche in nell'aorta ascendente e a in quella discendente a media altezza. Il valore massimo raggiunto dalla geometria dell'arco bovino è molto inferiore a quello ottenuto per la configurazione standard: si misura una differenza percentuale del 34% tra le due configurazioni. Ciò suggerisce che la configurazione standard presenta nel complesso una maggiore probabilità per l'AD di propagarsi.

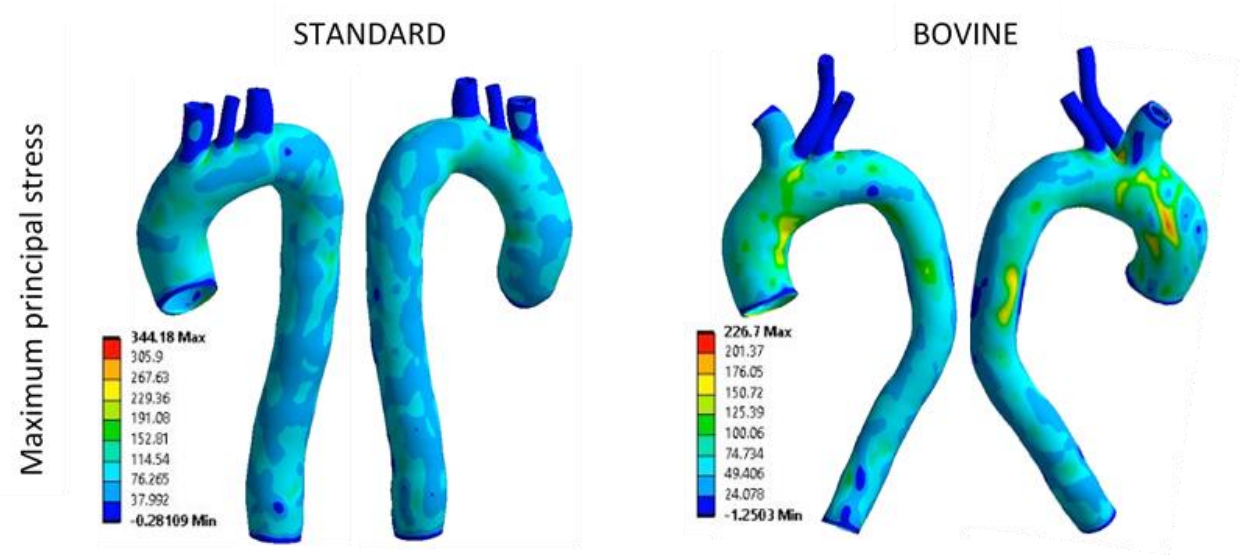

Figura XVII Stress principali massimi per le due configurazioni.

Il confronto tra le due configurazioni suggerisce che la geometria dell'arco bovino ha una maggiore probabilità di sviluppare il tipo B AD, e che la configurazione standard ha una maggiore probabilità per l'AD di svilupparsi se si verifica la lacerazione della tunica intima.

IV. Conclusioni

In questo lavoro di tesi sono state implementate simulazioni FSI di tipo 2-way al fine di valutare l'influenza delle diverse condizioni di pressione e di varie configurazione geometriche sullo sviluppo e la propagazione dell'AD. I risultati ottenuti suggeriscono che la variazione delle condizioni al contorno influisce sulla probabilità per il vaso aortico di sperimentare la patologia

della dissezione. Il caso di ipertensione è mostrato come la condizione più rischiosa per la patologia di dissezione aortica, il che è conforme ai dati clinici. Per quanto riguarda l'impatto della geometria dell'arco aortico, si osservano differenze significative nei flussi e nella distribuzione dei descrittoti basati sui WSS. Si può affermare che la configurazione standard ha una maggiore probabilità che l'AD inizi alla parete posteriore dell'aorta ascendente, all'area di biforcazione del BCT e dello SCA e lungo tutta la LCCA. Nella configurazione ad arco bovino, invece, la lacerazione ha una maggiore probabilità di verificarsi in corrispondenza delle biforcazioni del vaso sopra-aortico o nel tratto distale dell'aorta discendente. Questo studio è influenzato da alcune limitazioni, come la scelta di utilizzare un modello isotropico per il dominio strutturale o l'impossibilità di confrontare i risultati con l'esito clinico dei pazienti. Ciò apre le possibilità per ulteriori indagini.

V. Bibliografia

[1] Kurz SD, Falk V, Kempfert J, Gieb M, Ruschinski TM, Kukucka M, Tsokos M, Grubitzsch H, Herbst H, Semmler J, Buschmann C. Insight into the incidence of acute aortic dissection in the German region of Berlin and Brandenburg. International journal of cardiology 2017; 241: 326-329

[2] Criado FJ. Aortic dissection: a 250-year perspective. Texas Heart Institute journal 2011; 38: 694-700

[3] Khan IA, Nair CK. Clinical, Diagnostic, and Management Perspectives of Aortic Dissection. Chest 2002; 122: 311-328

[4] Nienaber CA, Clough RE, Sakalihasan N, Suzuki T, Gibbs R, Mussa F, Jenkins MP, Thompson MM, Evangelista A, Yeh JS. Aortic dissection. Nature Reviews Disease Primers 2016; 2: 1-18

[5] Khanafer K, Berguer R. Fluid–structure interaction analysis of turbulent pulsatile flow within a layered aortic wall as related to aortic dissection. Journal of Biomechanics 2009; 42: 2642-2648

[6] Chi Q, He Y, Luan Y, Qin K, Mu L. Numerical analysis of wall shear stress in ascending aorta before tearing in type A aortic dissection. Computers in biology and medicine 2017; 89: 236-247

[7] Pasta S, Rinaudo A, Luca A, Pilato M, Scardulla C, Gleason TG, Vorp DA. Difference in hemodynamic and wall stress of ascending thoracic aortic aneurysms with bicuspid and tricuspid aortic valve. Journal of Biomechanics 2013; 46: 1729-1738

[8] Campobasso R, Condemi F, Viallon M, Croisille P, Campisi S, Avril S. Evaluation of peak wall stress in an ascending thoracic aortic aneurysm using FSI simulations: effects of aortic stiffness and peripheral resistance. Cardiovascular engineering and technology 2018; 9: 707-722

[9] Gasbarro MD, Shimada K, Di Martino ES. Mechanics of abdominal aortic aneurysm. European Journal of Computational Mechanics/Revue Européenne de Mécanique Numérique 2007; 16: 337-363

1 Introduction

In this chapter an overview of the structure, the hemodynamic and the imaging techniques of the aorta will be given. The focus of the first section is on the description of the aortic dissection pathology, while the influence of the flow patterns and the pressure levels will be exploited in the second paragraph. Finally the most common ways to obtain medical images are presented.

1.1 Aortic structure

1.1.1 Anatomy and physiology

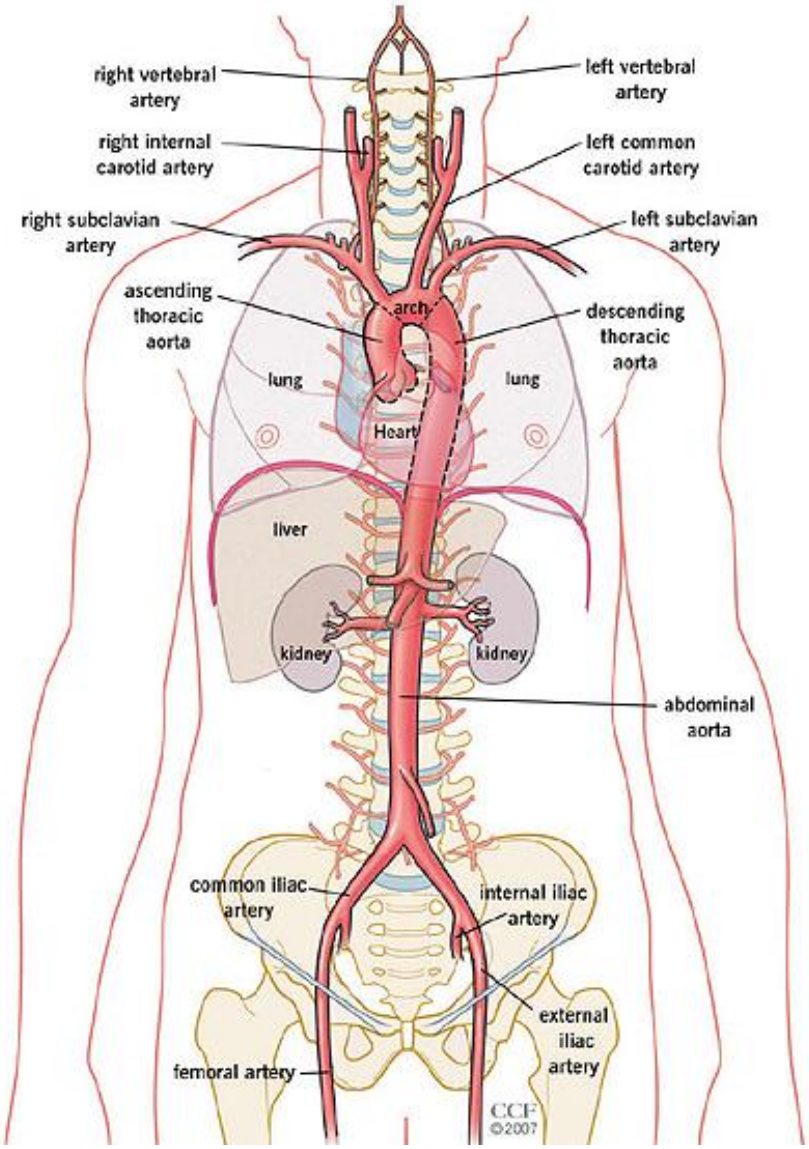

Figure 18 anatomy of the aorta [87].

The aorta (Figure 18) is the main artery of the human body, responsible for bringing the oxygenated blood to all the human body's districts through the systemic circulation.
It originates from the left ventricle of the heart, extending till the abdomen where it splits into the iliac arteries. Two portions of the aorta can be distinguished, the thoracic and the abdominal aorta, which are divided from one another by the diaphragm. The thoracic aorta is again divided

in sub portions: the aortic root, the ascending aorta, the aortic arch, and the descending aorta. The average diameter of the ascending aorta is around 3 cm, this value diminished to 2,5 cm in the descending aorta and to 2 cm in the abdominal one.

All the main arteries of the systemic circulation arise from the aorta or from one of the aortic branches. Moving from the proximal to the distal aorta the first two branches that can be observed are the right and left coronary arteries that originates from the aortic root, in particular from the Valsalva sinuses, to supply oxygenated blood to the myocardium. Then three large vessels arise from the aortic arch to oxygenate the upper part of the body (head, neck, and arms): the brachiocephalic trunk (BCT) or innominate artery, that bifurcate into the right common carotid artery and the right subclavian artery, the left common carotid artery (LCCA), and the left subclavian artery (SCA). In the chest, the descending aorta gives off branches to pericardium (the sac that encloses the heart), bronchi, oesophagus, part of the diaphragm, and intercostal spaces; while the abdominal aorta supply organs such as stomach, liver, spleen, pancreas, kidneys, intestine, and reproductive glands. Finally, at the L4 vertebra level, the aorta bifurcates into the iliac arteries, that oxygenate the lower body.

The aortic vessel belongs to the category of the so-called elastic arteries, meaning it presents a high percentage of elastin in the wall microstructure that gives the vessel a compliant behaviour. This characteristic allows the aorta to damp the pulsatory effect of the heart and generate a nearly steady flow at the capillary level, by storing part of the blood during the systole phase and releasing it during the diastole one. The aorta has also a regulatory function thanks to the presence of the baroceptors and chemoreceptors into the aortic arch. The baroceptors are mechanoreceptors which are sensible to the wall stretching, through which they control the blood pressure (BP) of the systemic circulation. When an excessive stretch of the wall occurs, reflexes of the sympathetic and parasympathetic nervous system are activated in order to control the cardiac output and the peripheral resistance and maintain a physiological pressure value. The chemoreceptors monitor the blood composition, detecting changes in the levels of oxygen (O_2), carbon monoxide (CO_2) and protons (H^+). Too low levels of O_2 (hypoxia) or too high quantities of CO_2 and H^+ (hypercapnia or acidosis) activate a response of the nervous system that adjust the respiratory functions and induce vasoconstriction.

1.1.2 Bovine aortic arch

The common configuration of the aortic arch branching with three vessels arising from the arch is observed in around 80% of subjects, meaning that there is a statistically significant portion of the population that instead presents a different branching pattern. According to many studies [] the most common variation is the bovine aortic arch that has an incidence of approximately 10-15%.

The bovine aortic arch is characterised by the presence of a common origin of the innominate and left carotid artery (CILCA), or, less frequently, by the origin of the left carotid directly from the innominate artery (type 2 CILCA) (Figure 19). The name "bovine" was given based on the apparent resemblance of the bifurcation pattern of the cattle's aortic arch, but this is now considered a misnomer because it has been observed that there are, instead, significant differences; for this reason recent guidelines have invited to find an alternative way to call this anatomical peculiarity and many research studies as adopted the acronym CILCA [1, 2]. The impact of the CILCA on pathological cardiovascular events is often underestimated, but there is evidence in the literature that it can be a potential determinant of the onset of thoracic aortic disease such as thoracic aortic aneurysms (TAAs) and aortic dissections (ADs) [2-4]. Also, CILCA has an in impact on the feasibility and the efficacy of the procedure of thoracic endovascular aortic repair (TEVAR) [1, 5]. Indeed the increased tortuosity and angulation of the proximal landing zone can affect the performance of the endograft.

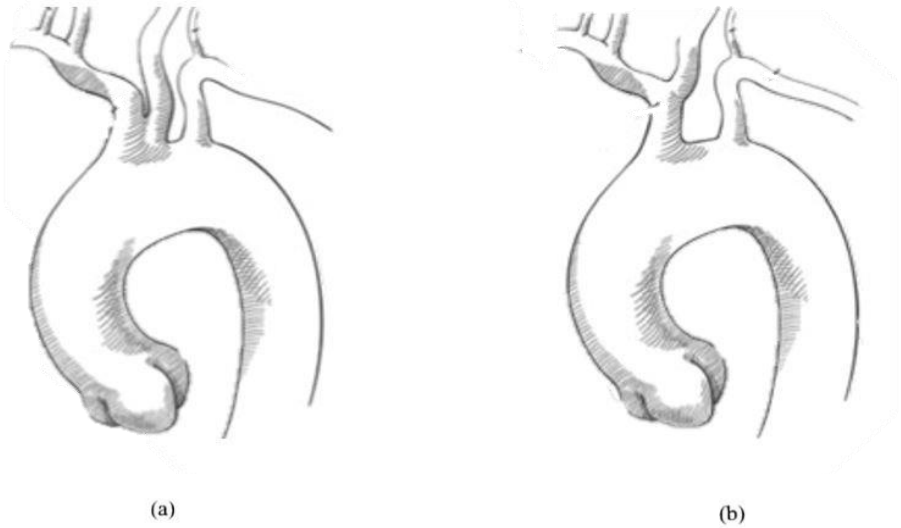

Figure 19 Anatomy of the bovine aortic arch. (a) common origin brachiocephalic trunk and left common carotid artery (type 1 CILCA). (b) left common carotid artery departing from brachiocephalic trunk (type 2 CILCA) (modified from[3]).

1.1.3 Wall microstructure

The aortic wall is constituted by three layers with different microstructure and function: the tunica intima, tunica media and adventitia (Figure 20).

The tunica intima, that is the innermost layer, is made of a sheet of endothelial cells (ECs) together with a basal lamina of collagen type IV and an additional sheet of muscle cells and connective tissue, that is present only in the elastic arteries. The ECs are directly in contact with the blood, creating a non-thrombogenic barrier that regulates exchanges of oxygen and other selected substance between the bloodstream and the surrounding tissues. Other then that they are sensible to the mechanical stimuli imposed by the flux and are able to transform these stimuli in chemical responses and structural changes of the aortic wall itself (mechanotransduction). A thin elastic lamina separates the tunica media from the intima, giving structural support and flexibility at the same time.

The media layer, which is the thickest layer, is formed by vascular smooth muscle cells (VSMCs), extracellular matrix (ECM), elastin, and type IV collagen, arranged in concentric layers or lamellar units. It is mainly responsible for the mechanical properties and for the viscoelastic behaviour of the aorta, allowing the regulation of the vascular tone and the vessel's response to the pressure loads. Another thin elastic lamina separates the media layer from the adventitia one.

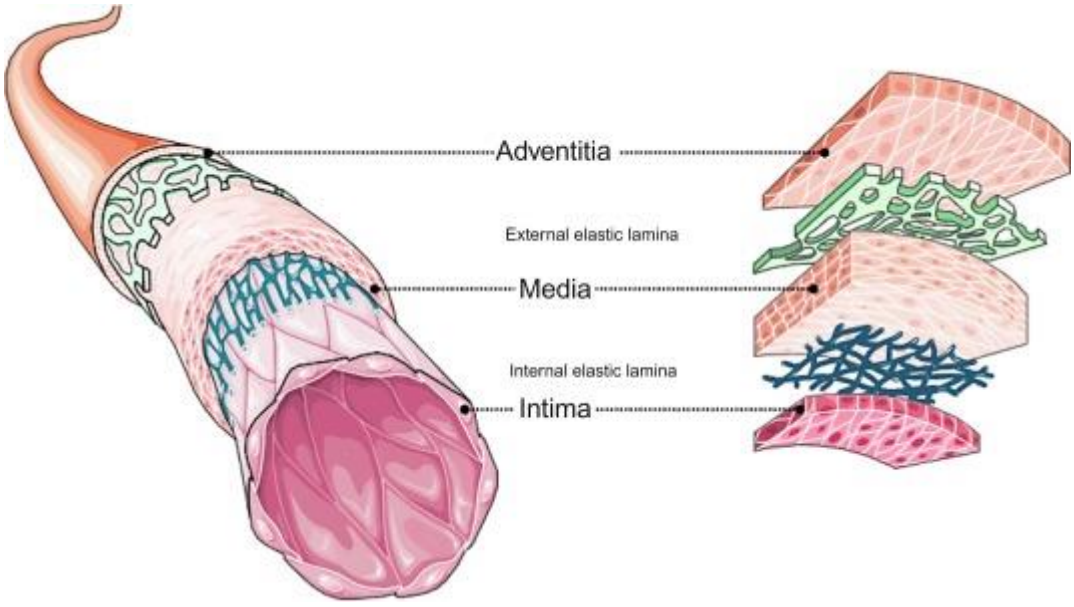

Figure 20 Aortic wall microstructure [88].

The tunica adventitia is a dense network of type I collagen fibers, containing nerves, fibroblast, and vasa vasorum that deliver oxygen and nutrients to the vessel itself. It contributes to the mechanical support to prevent overdistension of the vessel.

The wall microstructure is strictly related to the properties and functionality of the wall itself. Whenever one or more component of the different layers is corrupted, severe cardiovascular pathologies can occur, such as aneurysms and aortic dissection. In particular, if the wall gets stiffer the compliant behaviour of the vessel results compromised and, as consequence, wall's deformation occurs when further loads are applied [6-8]. Wall stiffening normally happens in elderly people, which indeed are more prone to this type of pathologies [9].

1.1.4 Aortic dissection

Aortic dissection (AD) is a life-threatening condition, characterized by a tear in the tunica intima and a false lumen in the tunica media through which blood can flow. The hemodynamic and the functionality of the dissected aorta are seriously compromised and, indeed, it cannot be left untreated.

1.1.4.1 Mortality rate and major complications

AD presents an acute phase, corresponding to the 2 weeks after the first symptoms show up, and a chronic phase that starts at the end of the 2 weeks. The mortality rate for patients with untreated acute aortic dissections has been reported to increase by 1 to 3% per hour after presentation and is approximately 25% during the first 24 hours, 70% during the first week, and 80% at 2 weeks [10-12]. These percentage are affected by the difficulties in the diagnosis of the pathology, whose symptoms (usually chest and back pain) can easily be confused with myocardial ischemia or other conditions, and by the velocity at which fatal complications occur [12]. Statistics say that about 20% of the patients die before they even get to the hospital [13]. The most common complications of AD are aneurysm formation, aortic rupture, cardiac failure (acute aortic regurgitation, acute myocardial infarction, or cardiac tamponade) and end-organs ischaemia. The latter results by a static or dynamic obstruction of the main arterial branches, that leads to a low or absent perfusion of one or more districts of the body. Static obstruction can occur when the dissection is associated with the origin of a branch vessel or extends into

the vessel itself and presents a thrombus that can compromise the blood flow at the vessel's entrance. Dynamic obstruction, instead, is observed when the pressure generated in the false lumen overcome the one in the true lumen, leading to the collapse of the true lumen in correspondence of an arterial branch's origin. This usually happens when a patent dissection presents a small exit site with respect to the entrance one, leading to blood accumulation in the false lumen and increment of blood pressure (BP). Dynamic obstruction often affects the coronary arteries in the diastole phase, leading to cardiac failure [13]. It has been shown that a dissection with an entry tear of 10 mm or more in diameter had a higher incidence of aortic expansion or rupture and true lumen collapse, while a false lumen diameter of 22 mm or more almost certainly leads to aneurysm formation [14, 15].

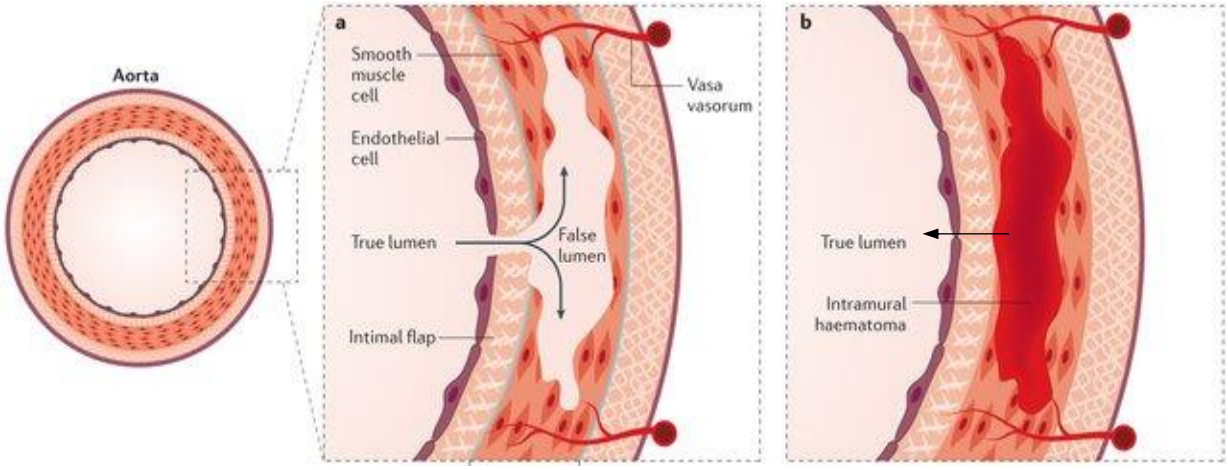

Figure 21 Aortic dissection formation. (a) Tear formation in the tunica intima followed by false lumen expansion in the tunica intima. (b) intramural hematoma that ruptures the tunica intima [96].

1.1.4.2 Histological changes and biomarkers

Aortic dissection formation usually starts with a tear in the tunica intima, which then propagate into the tunica media, causing the separation of the layers themselves and the formation of the false lumen (Figure 21, a). The entry tear can be the result of penetrating atherosclerotic ulcers, especially in the elderly patient, but there is not a strict correlation between the two phenomena. As an alternative AD can generate from an intramural haematoma, caused by the rupture of the vasa vasorum, which later ruptures into the aortic lumen (Figure 21, b). In both cases, a histological degeneration of the tunica media is a fundamental component of the underlying pathology of AD. Many patients, especially those with a pre-existing aneurysm, experience cystic medial necrosis, a pathological condition characterized by the loss

and fragmentation of elastic fibres, the loss of smooth muscle cells and the accumulation of proteoglycans in the medial layer of the aorta. The use of biomarkers that spot these histological changes, is currently being evaluated as a new technique for the detection of AD and identification of patients at risk [13, 16, 17]. At present, the most clinically used biomarker is the D-dimer, a fibrin degradation product generated by the fibrinolysis of a thrombus, that is highly predictive of acute AD with sensitivity of 98% and specificity of 54% at a cut-off value of 2.05 μg/mL. Other useful markers are the smooth muscle markers (myosin heavy chain and the calponin), which reflect the destruction and release of medial smooth muscle cellular components into the circulation at the time of dissection, and the inflammatory biomarkers (C-reactive protein), that are related to the extent of the aorta's damage and ongoing inflammation. Within this last category, IL-6 is an interesting biomarker that originates from the liver after stimulation with cytokines and give information on the severity of dissection and the time after presentation.

1.1.4.3 Pathogenesis

The pathogenesis of the AD is still poorly understood, being the final stage of a multifactorial process that can involve different causes and conditions, which are responsible for the damaging of the aortic wall structure. Chronic hypertension is considered to be a major risk factor, as it imposes a high loading condition at the wall continuously in time. Elevated stresses promote wall stiffening and the microstructural changes associated with the cystic medial necrosis condition. Another pathology that can contribute to AD is the atherosclerosis, an accumulation of fatty deposit that can be responsible for damages to the endothelium. Some studies have demonstrated that there can be also a genetic predisposition to the development of AD [12, 16]. This is the case of patients affected by the Marfan syndrome, a disorder of the connective tissue caused by a mutation of the FBN1 gene that code for the fibrillin, as well as the Loeys-Dietz syndrome characterized by a mutation of the genes TGFBR that code for TGF-β receptor of the connective tissue's growth factors. Other than that, males are more prone to AD, and habits such as smoking and drinking alcohol can increase the risk for the arising of this pathology.

1.1.4.4 Classification and treatments

ADs can be classified according to different schemes (Figure 22), but the most common one is the Stanford classification, that distinguishes between type A dissections, which involve the

ascending aorta, regardless of the origin location, and type B dissection that involve the aorta distal to the origin of the SCA. Type A dissections are the most common (50-60%) and dangerous ones [18]; they usually require intervention in the acute phase to avoid major complications or the death of the patient, and are typically treated surgically even in the most uncomplicated cases. Conventional surgical treatment involves the resection of the diseased part of the aorta containing the intimal tear, and the replacement of this segment with a synthetic (Dacron) vascular prosthesis (Figure 23, a). In cases of severe aortic insufficiency, aortic valve replacement or aortic valve-sparing resuspension will be done at the same time as surgery for the dissection. In some cases, such as with dilatated aortic root (>50 mm in diameter), it can be required also the re-implantation of the coronary arteries during the procedure.

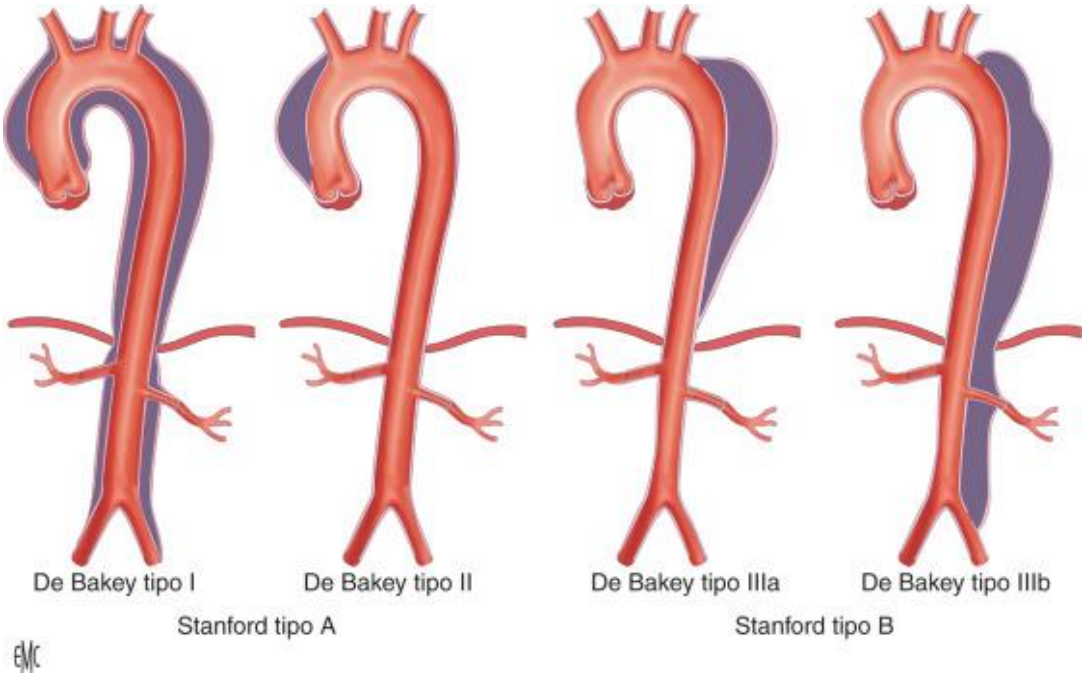

Figure 22 Aortic Dissection DeBakey classification and Standford classification [92].

Type B dissections are statistically less severe, happening to reach the chronic phase much more often than the type A ones. They still represent a critical condition for the patient but, if no co-morbidities or major complications are present, it can be managed through medical therapy. Medical therapy consists of β-blockers (propranolol, metoprolol, labetalol, esmolol) and vasodilators, that are used to contrast hypertension and maintain the systolic pressure between 100 mmHg and 120 mmHg. The patient should be maintained under strict supervision for the duration of the therapy in order to check the outcomes and spot possible complication that can arise. Positive outcomes are expected within three months; if after this amount of time

no significant improvement is observed, surgical procedure become mandatory to preserve the subject's health. Type B AD is suitable for a less invasive surgical procedure called endovascular repair (TEVAR). The core principle underpinning the TEVAR procedure for the treatment of AD, is to place a covered stent graft over the entry tear in the descending thoracic aorta (Figure 23, b). The stent graft is meant to prevent further blood flow in the false lumen, avoid the collapse of the true one and promote the thrombosis of the false lumen. The dissected wall is not resected in this procedure, the false lumen is left where it is and completely filled-up through thrombus formation. Complications that can induce the surgeon to choose to perform TEVAR are malperfusion issues, repetitive symptoms, or refractory or difficult-to-control hypertension; indeed these symptoms are particularly likely to develop complications of acute dissection with fatal consequences for the patient. Short-term outcomes of TEVAR procedure and medical therapy does not present significant different in uncomplicated type B AD, justifying the choice of medical treatment when possible [19]. However recent studies on long-term outcomes have shown that TEVAR gives better results [20, 21], suggesting TEVAR should be considered even for the treatment of uncomplicated type B AD. The debate on which choice is the best is still open, so no precise guidelines are present for these cases.

1.1.3.5 Hemodynamic patterns

Aortic dissection presents complicate hemodynamic patterns, characterized by blood splitting into two pressurized lumen and intimal flap motion in the blood flux. The blood entering the intimal tear is accelerated creating a jet that can impinge on the opposite wall of the false lumen, while a disturbed flow characterized by recirculation patterns is commonly observed in the lumen distal to the entry tear. The hemodynamic depends also on the presence or not of an exit tear distal to the entry one. When an exit tear is present (patent false lumen) an increase in the false lumen pressure is usually observed which can lead to its dilation or to dynamic obstruction [22, 23], while if the false lumen is closed blood stagnation occur with consequent thrombus formation. A complete thrombosis can help stabilize the AD, avoiding further dilatation, instead a partial thrombosis can increase the risk for static obstruction and end-organ ischemia [24].

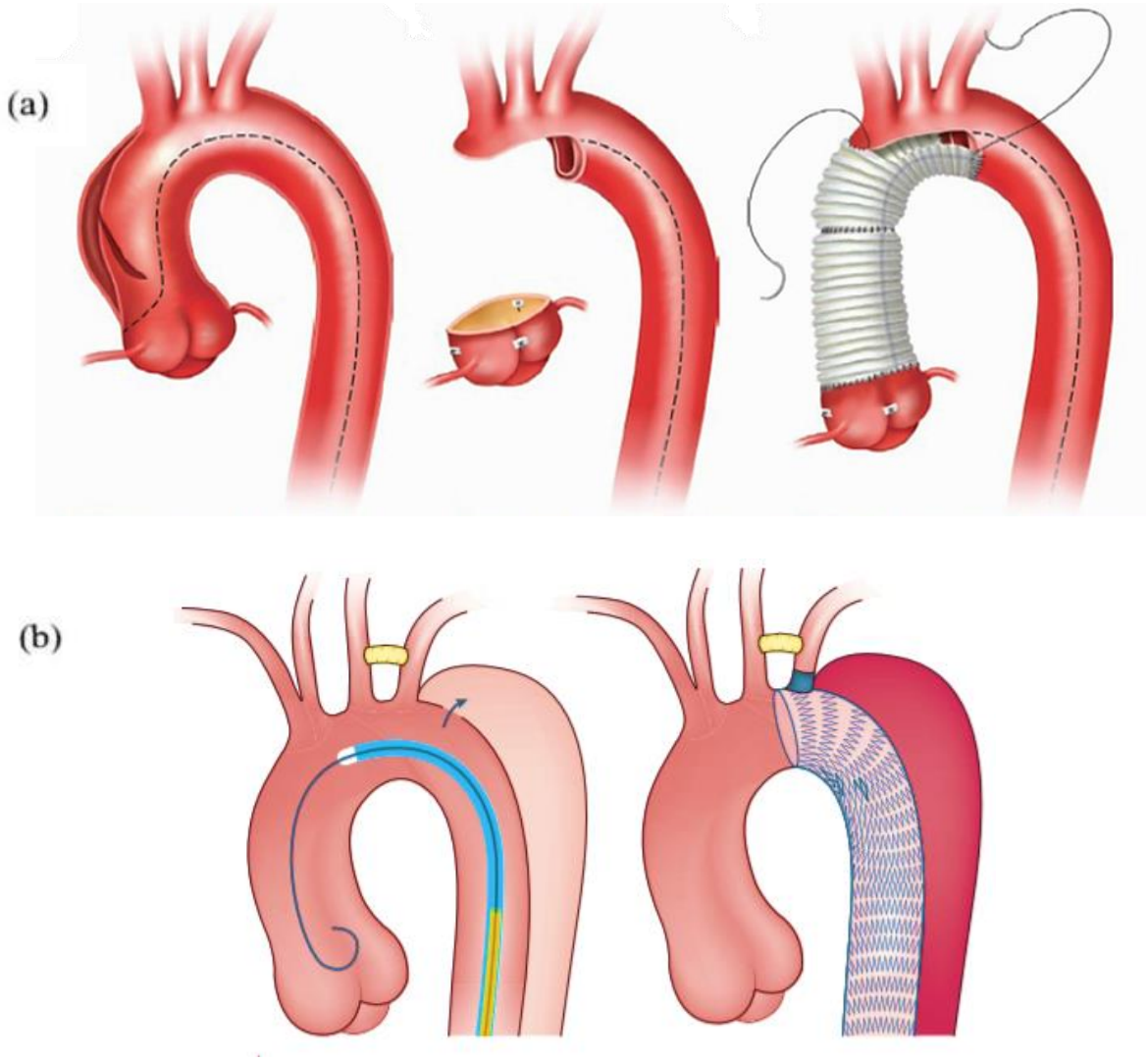

Figure 23 Aortic dissection management. (a) Surgical repair [89]. (b) TEVAR procedure [16].

Reported incidence of AD vary a lot between different studies, ranging from 2 to 15 cases over 10000 individuals per year [10, 25]. This numbers are not high enough to consider AD a diffuse pathology, however it affects a sufficient amount of people to maintain elevated the interest in studying this disease. A deeper knowledge of the process that leads to formation of the intima tear is pursued, in order to predict which subject should be taken under observation and intervene before major complications occur.

1.2 Aortic hemodynamic

1.2.1 Aortic flow

The aortic flow patterns in the aorta depend on many factors and change significantly moving from the ascending aorta to the descending one. The pulsatile nature of the cardiac cycle causes the inertial forces to be dominant in the ascending aorta, meaning that the velocity tends to have a flat profile and can be approximate as constant on the inlet sections in correspondence of the aortic valve. Moving away from the inlet the velocity develops in a parabolic profile due to the viscous nature the blood, being made for the 45% by cells suspension (hematocrit). Viscosity can be defined as the resistance to motion of a fluid and quantify the frictional forces that develop between adjacent layer of fluid in relative motion. Frictional forces developed at the wall are much higher of the ones at the centre of the vessel causing the fluid to slow down and to create a boundary layer. The frictional forces imposed on the wall generate the so-called Wall Shear Stress (WSS), stresses tangential to the flow direction whose magnitude directly depend on the viscosity of the fluid and the gradient of the fluid's velocity in the radial direction (Figure 24). It has been reported that vascular WSS can affect both the functional and the structural integrity of the endothelial cells (ECs) on which they are applied [26-28].

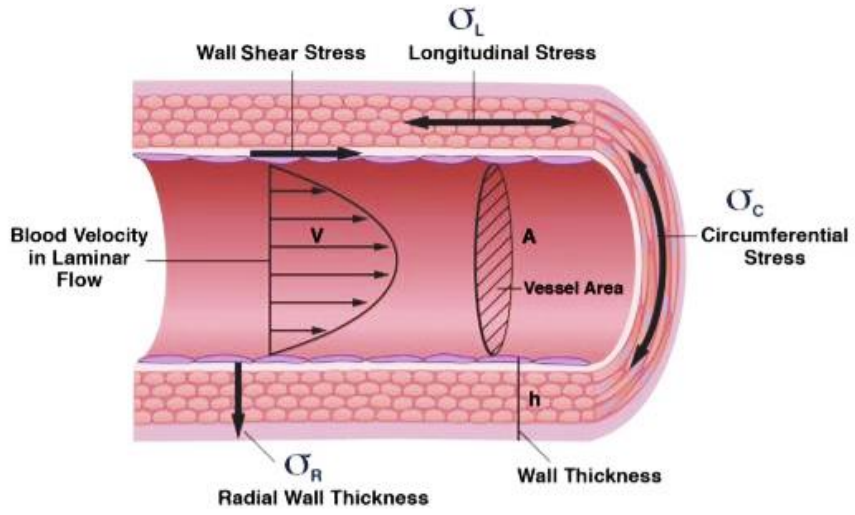

Figure 24 Velocity profile and Stresses imposed on the wall of a generic vessel [93].

ECs are sensitive to mechanical stimuli and respond to them through the process of mechanotransduction, which transform the mechanical inputs into biochemical signals. The transmission and transduction of hemodynamic forces is normally responsible for the regulation of vascular tone (vasodilation and vasoconstriction) to maintain the homeostasis, but in case of long-term flow alterations it leads to structural changes and wall remodelling. It regulates the production or the degradation of structural proteins (collagen and elastin) in the tunica media, altering the mechanical properties and resistance of the wall to further imposed stresses. Irregular WSS are responsible also for morphological changes of the ECs, causing them to switch from an elongate shape along with the flow direction to a polygonal shape. The unclear orientation of the polygonal configuration favour a lack of organization at the cytoskeletal level, which is involved in the mechanotransduction process, and a proliferation of cells, that can lead to atherosclerotic pathology.

One factor that influence the WSS imposed on the vessel's wall is whether the blood flow is laminar or turbulent. Laminar flow is characterized by a stable velocity field in which fluid typically flows in parallel layers or laminae, while on the contrary, turbulent flow is defined by stochastic variations of velocity and pressure, eddies formation and energy dissipation. The WSS are almost constant over time in the laminar case, while they tend to oscillate and change their magnitude and direction in turbulent one. The aortic flow is typically laminar, but there are some specific conditions in which the geometry causes the flow to disrupt in more complicated patterns, like where there is a high curvature, bifurcations, or a change in the section of the vessel (for example, a narrowing in the lumen caused by atherosclerotic condition). The curvature of the vessel causes both the inertial forces and the viscous ones to generate secondary flows, which are defined as flow patterns observed in the axial planes perpendicular to the primary flow direction. In the first tract of the aortic arch, where inertial forces are dominant, the fluid tends to move radially from the outer wall to the inner one because of the centripetal force, causing the peak velocity to shift inward on the axial plane (Figure 25, a). When the viscous forces outgrow the inertial ones, secondary flows develop in the opposite direction with the fluid moving radially to the outer wall and the velocity peak shifted outward. The fluid motion towards the inner wall or the outer one, is compensated by other fluid that move in the opposite directions along the wall itself, leading to the creation of two counter-rotating vortices on the axial plane (Figure 25, b).

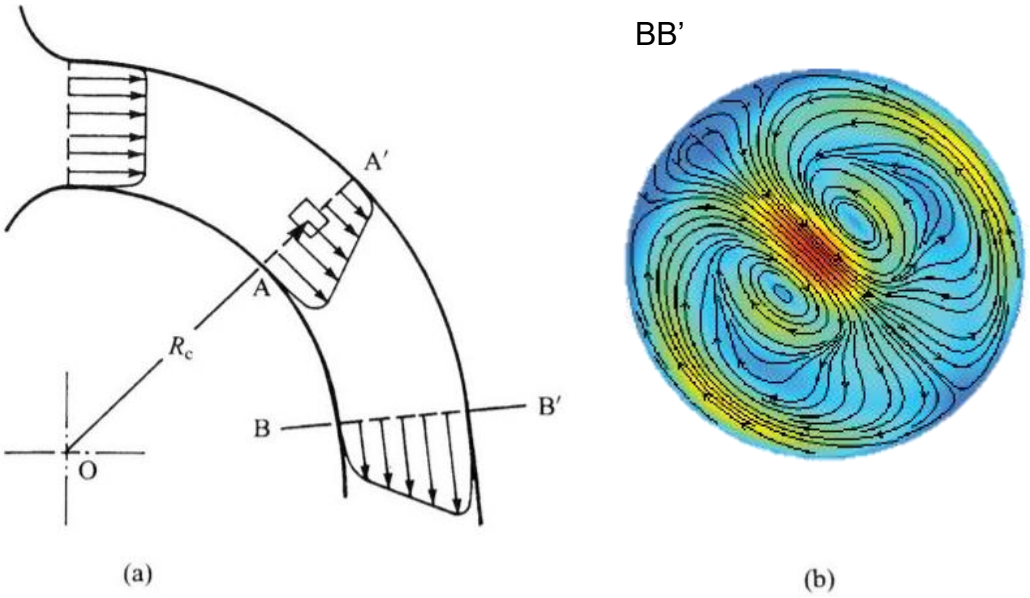

Figure 25 (a) Velocity profile in a curved vessel. (b) Secondary flows [91].

Another factor that influences the WSS is the aortic pressure, which determine the magnitude of the WSS imposed on the wall. The increase of the blood pressure (BP) leads to higher values of WSS, while the diminishing of the BP generates low WSS.

1.2.2 Aortic pressure

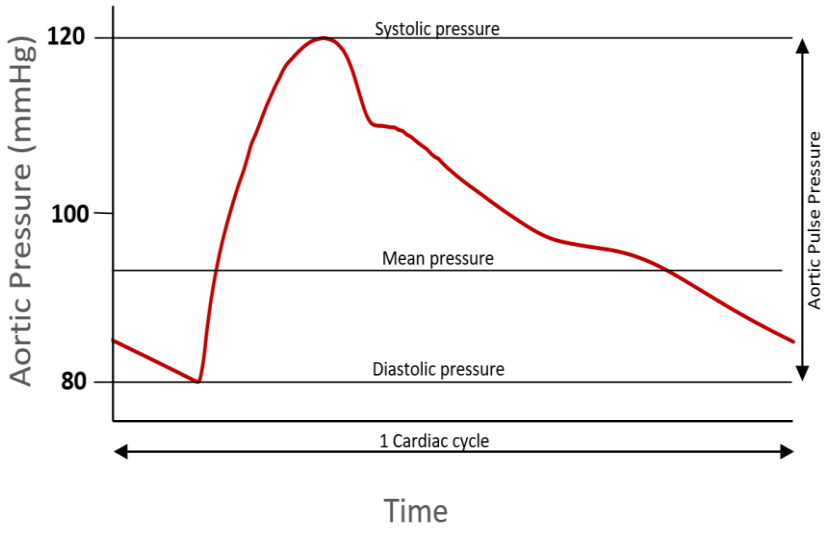

Figure 26 Aortic pressure profile.

BP is one of the most commonly measured clinical parameters, whose values are major determinants of therapeutic decisions. Aortic pressure varies over the cardiac cycle, increasing abruptly during the systolic phase and decreasing smoothly during the diastolic one. The maximum value reached is the systolic pressure while the lowest value is the diastolic pressure (Figure 26). Physiological values associated to the systolic pressure and the diastolic one, are respectively around 120 mmHg and around 80 mmHg. The difference between the systolic and diastolic pressures is the aortic pulse pressure, which typically ranges between 40 and 50 mmHg. Systolic pressure is directly proportional to the ventricular stroke volume, that is the volume of blood ejected in the systemic circulation. This is quite intuitive cause the pressure depends on the amount of blood that push against the aortic wall. Another major determinant of the pulse pressure is the aortic compliance. The vessel's ability to deform and increase the volume in which the blood is stored, allows to reduce the load imposed to the wall. Therefore, the more compliant the aorta, the smaller the pressure change during ventricular ejection.

The maintenance of the physiological pressure's levels is typically assured by the autoregulatory ability of the cardiovascular system. When baroceptors register even the slightest pressure change, the autonomic nervous system instantaneously compensates it by regulating the cardiac output (usually by increasing or decreasing the heart rate) and the peripheral resistance. When this mechanism is not able to maintain the pressure homeostasis, significant variations are observed which can affect the cardiovascular system functioning and promote major cardiovascular diseases.

1.2.3 Hypertension

Hypertension refers to a lasting increase in BP with heterogeneous genetic and environmental causes. The diagnosis of hypertension is made when a systolic pressure higher than 140 mmHg or a diastolic pressure higher than 90 mmHg, is observed for at least two subsequent BP measurement. As shown in Table 3 there are then different stages of hypertension which depends on the pressure ranges.

The BP level is similar within family members, suggesting that it is influenced by genes' expression or variation [29, 30]. The identification of variant (allelic) genes that contribute to the development of hypertension is complicated because the two major determinant of BP (cardiac output and total peripheral resistance) are controlled by multiple different factors, including the autonomic nervous system, vasopressor/vasodepressor hormones, the structure of the cardiovascular system, body fluid volume, renal function, and many others. Each of these complex mechanisms can be controlled by a significant number of genes, making it difficult to understand which ones are responsible for BP change. Other than that, there exist a number of factors that lead the pressure to increase above the inherited level, including obesity, insulin resistance, high alcohol intake, high salt intake (in salt-sensitive patients), aging and perhaps sedentary lifestyle, stress, low potassium intake, and low calcium intake. For this reason even people that present a normal or a high normal pressure level (Table 3) can be at risk of hypertension if one or more of these factors are added.

Category	Systolic, mm Hg		Diastolic, mm Hg
Optimal	<120	and	<80
Normal	<130	and	<85
High normal	130–139	or	85–89
Hypertension			
Stage 1 (mild)	140–159	or	90–99
Subgroup: borderline	140–149	or	90–94
Stage 2 (moderate)	160–179	or	100–109
Stage 3 (severe)	≥180	or	≥110
Isolated systolic hypertension	≥140	and	<90
Subgroup: borderline	140–149	and	<90

When a patient's systolic and diastolic blood pressures fall into different categories, the higher category should apply.
From JNC VI.[3]

Table 3 Definition and classification of Blood Pressure levels [29].

There is a strong positive and continuous correlation between high BP and the risk of cardiovascular diseases (stroke, myocardial infarction, heart failure) [31, 32], renal disease [33], and mortality [34, 35]. Treatment of hypertension has been demonstrated to be an effective way to reduce the incidence of cardiovascular diseases. For the patients with normal high pressure or first stage hypertension the first approach to lower BP is usually lifestyle's changes, which

are based on the elimination of those factors that cause the pressure to rise over the inherited level. Stopping excessive alcohol consumption (>30 mL ethanol per day for man and >20 mL ethanol per day for women) and restriction of caloric intake are by far the most effective lifestyle measures that consistently reduce BP. Indeed, 1 kg loss of weight entailed an average BP decrease by 1.6 mmHg systolic and 1.3 mmHg diastolic [36]. Also the introduction of a low salt diet (<6 g NaCl per day) and the engagement in regular aerobic physical exercise (at least 30 minutes on three days of the week) has been shown to effectively decrease the BP in many patients [30, 37]. Lifestyle measures are usually recommended also for patients who should undergo pharmacological treatment, in order to reduce the dose or number of drugs required. Antihypertensive drugs are usually classified into two categories, those that inhibit the renin-angiotensin system and those that do not. Angiotensin converting enzyme inhibitors, angiotensin receptor blockers and β blockers belong to the first category, and are usually prescribed to white patients younger than 55 years, who tend to have higher renin concentration. Older patients and black population, instead, are usually treated with calcium channel blockers or diuretics. In many cases one drug is not sufficient to control BP, so drugs are added stepwise till the right combination of treatment is found. If the prescription of three different antihypertensive drugs including a diuretic is not sufficient to lower the BP under the threshold value of 140/90 mmHg, the hypertension is classified as refractory or resistant.

Hypertension is widely diffuse in the developed world as it affects 25-35 % of the adult population and up to 60–70% of the people older than 70 years old [30]. A better understanding of the pathophysiology, of the possible consequences and of the available treatments, is then of great interest for the clinical world, as it would enhance the prevention of cardiovascular diseases and would improve many people's life.

1.2.4 Hypotension

Hypotension is a significant decrease of the systemic blood pressure (BP). There are no specific guidelines for the classification of low BP, but systolic and diastolic pressure respectively of 90 mmHg and 60 mmHg are considered the threshold values under which hypotension occurs. It is a relatively benign condition, that becomes a concern only if pumping pressure is not sufficient to perfuse key organs with oxygenated blood, as in the case of a systolic pressure

lower than 70 mmHg. There exist multiple causes that can compromise the pressure's homeostasis, so different typology of hypotension has been identified through years.

Acute hypotension is the most severe case of low BP, happening to be life-threating for the patient as it is typically related to a shock syndrome, i.e. a syndrome in which a low perfusion of some body districts is observed. The lack of fluids in the peripheral vessels typically results from a failure in the regulation of cardiac output and vessels' resistance to reach a situation of equilibrium. In particular, distributive shock happens when it is not reached a sufficient peripheral resistance, while the cardiogenic shock occurs when it is not achieved an adequate cardiac output. There are then the hypovolemic shock, caused by a massive loss in body liquids due to a major hemorrhage or an overuse of diuretic medications that lead to an excessive fluid volume loss via urine, and the septic shock, related to the occurrence of an infection with sepsis. Acute hypotension is a medical emergency that requires immediate treatment to save the patient's life. The intervention should be chosen based on the primary cause of the BP lowering, and it usually consists in administration of intravenous fluids, blood transfusion, oxygen, vasopressors, or postural changes (lying down the patient with legs above waist height to promote blood circulation).

The most diffuse type of hypotension is the orthostatic or postural one, especially in the elderly people. It is defined as a systolic BP decrease of at least 20 mmHg or a diastolic BP decrease of at least 10 mmHg within three minutes of standing up [38, 39]. Orthostatic hypotension can be classified depending on its etiology as neurogenic, non-neurogenic, or iatrogenic (caused by medication). When symptoms are not sufficient to give a clear indication of the category the hypotensive condition belongs to, first an evaluation of the medication the patient is undergoing should be done, followed by an assessment of non-neurogenic etiologies such as venous pooling, intravascular volume depletion and sepsis. Only if both these possibilities are ruled out the neurogenic causes should be considered. Orthostatic hypotension is not typically a life-threatening condition, so its management is usually meant to improve the patient's quality of life. Medical prescription's modification and lifestyle interventions are usually sufficient, but sometime anti-hypotensive drugs may be necessary. The most common drug therapies are the fludrocortisone, that increase BP through promotion of renal sodium reabsorption and expansion of plasma volume, and vasoconstrictors.

Hypotension is not a risk factor for cardiovascular diseases, nevertheless it should not be underestimated or left untreated. An evaluation of the etiologies should be always considered, especially for those patients that experience hypotension repeatedly in time, because, in that case, the low BP can be a symptom of underlying pathologies.

1.3 Aortic imaging

Imaging of the aorta is a key aspect in the diagnosis and assessment of aortic diseases. It allows to plan the pathology's treatment and to check how the patient is responding to medications or surgery, in the follow-up phase. The imaging modalities commonly used for the evaluation of the aorta include standard chest radiography (CXR), transthoracic echocardiography (TTE), transesophageal echocardiography (TEE), angiography, computerized tomography (CT) and magnetic resonance imaging (MRI) [40, 41].

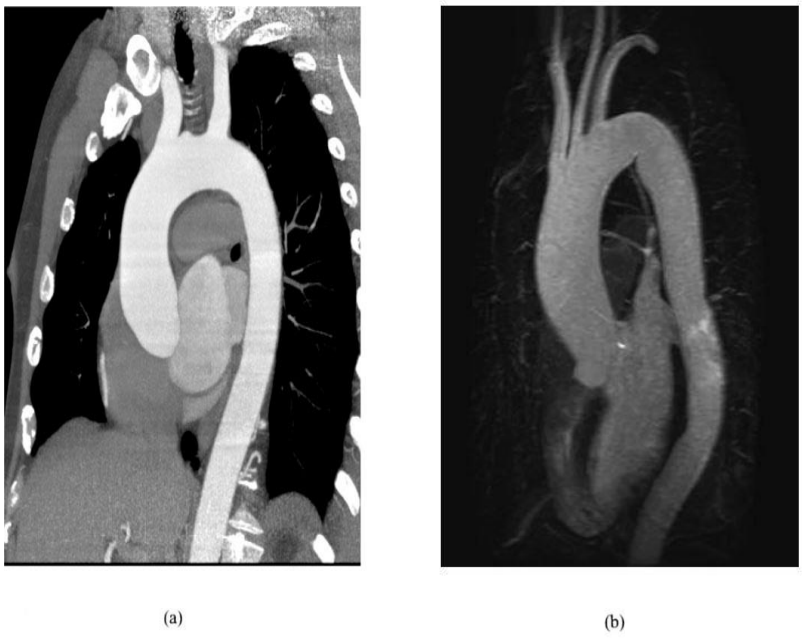

Figure 27 Imaging of the aorta. (a) Aortic reconstruction by CT angiography [42]. (b) Aortic reconstruction by MRA [95].

CXR is usually performed in emergency context when symptoms such as chest pain and dyspnea arise. It allows to assess if there are mediastinal abnormalities, but it is usually not enough accurate to discern different diseases, making further analysis necessary to obtain a diagnosis.

TTE is quick, cheap and easily available, but doesn't have a good resolution and could present artifacts, so again it is commonly followed by other analysis. It allows to evaluate left ventricular function, aortic valve competency and detect pericardial effusion.

TEE is characterized by a very good resolution that allows an accurate diagnosis, but it is limited to the assessment of pathologies of the aortic root and the aortic valve. It is an invasive procedure, that can cause the patient stress and discomfort with a consequent acceleration of the cardiac rhythm and an increase of the aortic pressure. It is usually performed under sedation and requires the intervention of specialists, so it other imaging techniques are usually preferred (except during surgical intervention).

MRI and CT are the most used imaging modalities, both being non-invasive and having a high resolution [42]. The main advantage of using MRI is the absence of ionising radiation, which is especially important when a patient has a pathology that needs to be checked over time and should undergo the imaging process multiple times. There are a number of MR techniques that are particularly useful for aortic imaging, all of which can be obtained in any prescribed plane. The so-called black-blood technique allows the assessment of the aortic wall, extracting anatomical details such as the thickness of the wall and, in case of AD, allowing to see the intimal flap and the entry tear location. The contrast-enhanced magnetic resonance angiography (MRA) is the most widely accepted method for comprehensive evaluation of the aortic disease (Figure 27, b). The procedure consists of the injection of a gadolinium-based contrast agent, that makes the blood bright in the images. The dosage and delivery rate should be adjusted according to individual patients, starting from a dosage's reference point of 10 to 20 mL, delivered at a rate of 2 to 3 mL/s. It is crucial to choose the right timing of imaging after the injection of the contrast agent to obtain the optimal image quality. MRA is characterized by high space resolution and quite good velocity of assessment but it only displays the lumen in which the blood is flowing, being the wall signal not enhanced. Another MRI-based technique largely used nowadays is the phase contrast MRI (PC-MRI), that allows a quantitative evaluation of the blood flow in the cardiovascular system. It relies on the use of two magnetic gradients, equal in magnitude but opposite in direction, applied one consecutive to the other. The movement of the fluid causes each proton to accumulate a phase shift along the direction of the gradient, which can be related to the velocity of the proton itself, through the VENC (velocity encoding) parameter. VENC is set by the operator depending on the amplitudes of the gradients used, and determinate the range of detectable velocities encoded by a PC sequence. The main

disadvantages of using MRI are the impossibility to use it for patients with pacemaker or any type of metallic device, the long acquisition time, and the limited availability.

CT is usually preferred in emergency situation in which a fast acquisition is needed. There are two techniques that can be useful for the evaluation of the aorta: the non-contrast CT and the CT angiography (CTA), also known as contrast enhanced CT. Non-contrast CT is usually performed only as an initial test, that allows to identify some specific pathologies such as the intramural hematoma (IHM) and to make some hypothesis, that can be verified with further analysis. To diagnose aortic pathologies or to make a complete characterization of the aorta it is instead used the CTA (Figure 27, a), which is based on the administration of iodinated contrast agent to opacified the aorta. One major limitation in the use of aortic CTA is the potential for development of nephropathy due to the iodine-based contrast agents. Patients that present severe aortic diseases often suffer of renal insufficiency, hence a risk assessment should be done before starting the treatment and an alternative technique should be chosen for the high-risk patients. To generate high-quality CTA images, electrocardiographic gating (ECG-gated CT) is crucial for reducing motion artifact, particularly in the aortic root, ascending aorta, and proximal arch.

The selection of the imaging modalities should be evaluated case by case, taking in considerations multiple factors as the availability, the clinical scenario of the patient (radiation issues, metallic components, risk of nephrotic development…) and the severeness of the pathology. In a situation of emergency CT and ultrasound are the best choices, while MRI is preferred for chronic diseases which required constant controls or for the follow-up assessment.

2 State of art

In this chapter an overview of the Fluid-Structure Interaction approach and of a multi-dimensional model for the computation of the boundary conditions is presented. The results obtained in previous works available in the literature, regarding the FSI simulations in the aortic vessel were reported. Three cases in particular have been analysed and presented in detail. Finally the objectives of this thesis work were stated.

2.1 Numerical simulations

Numerical simulations are engineering tools, that use computer modelling for the assessment of complex problems. Computer simulations have many applications in the biomedical field, as they reproduce the complexity of the human body's structure and the non-linear properties it is characterized by. The evaluation of tissues' response to healthy or pathological loading conditions and the assessment of the hemodynamic characteristics of a cardiovascular system, are two of the numerous investigations that can be performed. Furthermore, computational analysis can give great support to surgical planning. The outcomes of new medical devices can be estimated without needing the implantation into a patient, and the best way to perform a surgical procedure, avoiding complications or device failure, can be found. Several possibilities can be exploited by simply changing few parameters of a simulation, resulting in a very time and money saving approach.

There are three main types of numerical simulations, which allow to solve different sets of differential equations and, as a consequence, different type of problems. Finite Element analysis (FEA) allows mainly to solve structural problems, Computational Fluid Dynamic (CFD) is used for fluid dynamic problems, while Fluid-Structure Interaction (FSI) combine the structural analysis with the fluid one. Each of these simulations can give significant results when applied to the cardiovascular system. FEA measure stress, strains, and deformation applied on the vessel wall or on the leaflets of heart valves (usually the aortic one). These quantities can be generated both by a device implanted, typically stents and prosthetic valves inserted through catheter (Transcatheter Aortic Valve Replacement – TAVR), or simply by the pressurized blood. Also the dynamic of the valve's leaflets can be interesting to be assessed, especially when calcification or other pathologies cause stenosis or insufficiency. CFD simulations, instead, are used to calculate time-varying flow-related quantities such as velocity, pressure, and WSS, in the reconstructed geometry of the vessel with the assumption of rigid wall. The effect of disease onset or prosthesis implantation on the vessel hemodynamic can be assessed through CFD, as well as the effect of fluid dynamics on the development of aortic wall pathologies. FSI is the most complete approach as it permits to evaluates all the quantities mentioned above, taking into consideration also the reciprocal influence of the structural and fluid domain. FSI is able to model the wall motion according to the loads imposed by the blood flow and to account for the changes imposed by the wall displacement on the vessel hemodynamic. The drawbacks of

the FSI approach are the high computational cost and the difficulty in the setup of the simulation, that can encounter convergence and coupling problems.

2.2 Fluid-Structure Interaction

2.2.1 Overview

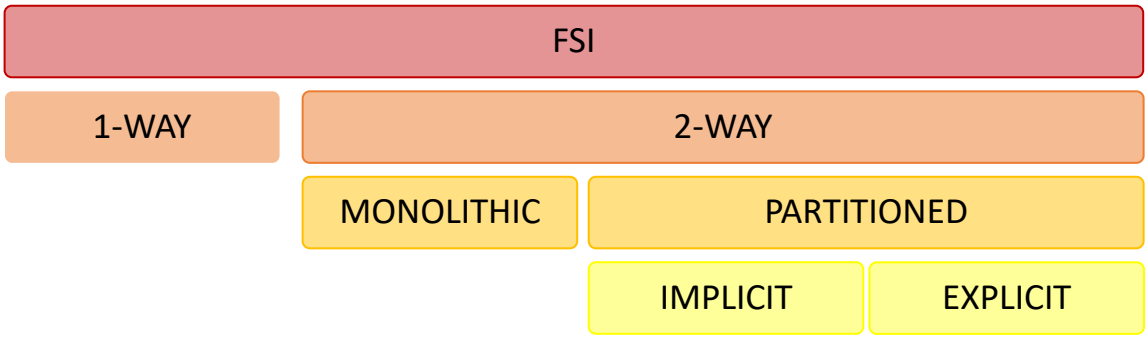

Figure 28 Schematic representation of FSI classification.

Fluid-Structure Interaction (FSI) methods allow the coupling between fluid dynamics and structural mechanics. The degree of physical coupling between the fluid and solid solution fields allows the classification in 1-way FSI and 2-way FSI (Figure 28).

1-way FSI refers to a system in which the fluid motion imposes a deformation on the structural domain, that is not significant enough to affect the fluid patterns. This system, that is defined as uncoupled, present a solution that can be calculated by first running the fluid dynamic simulation and then using the results as boundary condition for the structural domain. Also the opposite can happen, meaning that the structural domain affects the fluid one but not vice versa; anyway this case is not usually observed in the cardiovascular field.

2-way FSI refers to a system in which the fluid motion imposes a deformation on the structural domain, that is consequently responsible for changes in the fluid dynamic. It is a coupled problem, whose solution can be obtained through different approaches: the monolithic approach and the partitioned one (Figure 28). A monolithic or direct approach is when the equations governing the flow and the displacements of the structure are solved simultaneously, through the discretization of the problem into a unique, large matrix of equations. Fields are tightly coupled allowing a larger stability than other approaches, but at the same time presenting

a higher computational cost and a higher complexity in the setting up. In a partitioned approach, instead, the equations governing the flow and the displacement of the structure are solved separately with two distinct solvers, which then interact trough a coupling system. Within the partitioned approach it is possible to determine two subgroups depending on how strongly the two solvers are coupled (Figure 28). The choice of an explicit algorithm determines a loose coupling, being characterized by a single bidirectional exchange of solved variables for time step. This approach often presents instabilities, therefore it is not recommended for complex problems, such as the ones that present vorticity, complex geometries, highly deformable materials in the structural domain and so on. To implement a strongly coupled system it is preferable to us the implicit approach, in which the dependency between fluid and structural domains is converged withing a time step. The two solvers exchange multiple times the results they calculate, in order to reach a convergence target for the transferred quantities before moving to the next time step. The 2- way implicit FSI algorithm for a transient problem presents three levels of iteration (Figure 29): the time loop, which is responsible for the time advancement, the coupling loop, that iterates to convergence the quantities exchanged at the fluid structure interface, and the field loop, that calculate the solution within each solver. This structure is responsible for long simulations and high computational cost as to move from on time step to the nest one, thousands of iterations can be performed by the solver.

The choice of the model to apply is not unique and depends on the problem the user is trying to implement. Different algorithms are used by different solvers, ADINA and Comsol use the monolithic approach while ANSYS, Abaqus and AcuSolve use the partitioned one.

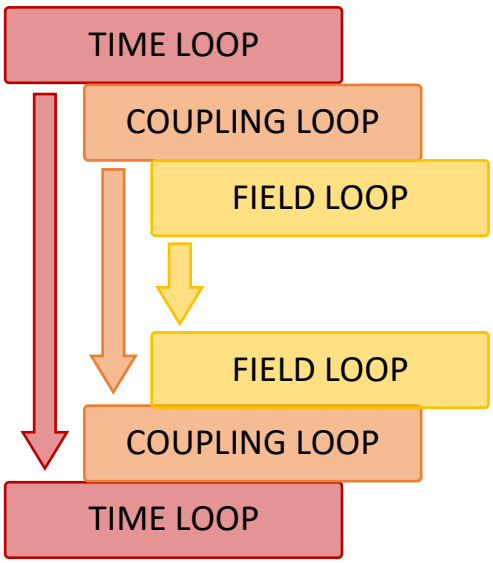

Figure 29 Schematic representation of the three FSI levels of iteration.

2.2.2 Governing equations

Governing equations are a set of equalities that permits to convert a physical problem into a mathematical model. FSI involves multiple equations due to the fact that each of the two domain is characterized by its own mathematical model. Other than that some conditions at the fluid solid interface should be imposed to guarantee the continuity between the domains. A description of the formulas that regulate the FSI system is reported below.

The mathematics behind fluid dynamics problems is based on the conservation laws, namely the conservation of mass, the conservation of momentum and the conservation of energy. To describe the hemodynamics of human vessels, the energy equation is not necessary and the continuity equation is reduced owing to the blood approximation to an incompressible, Newtonian fluid. Hence, the governing equations are the following ones:

- Conservation of mass (or continuity equation)

$$\nabla * \boldsymbol{v}_f = 0 \qquad \textbf{(1.1)}$$

- Conservation of momentum (or Navier-Stokes equation)

$$\rho_f \left(\frac{\partial \boldsymbol{v}_f}{\partial t} + (\boldsymbol{v}_f * \nabla)\boldsymbol{v}_f \right) = -\nabla P + \mu_f \nabla^2 \boldsymbol{v}_f + \rho_f \boldsymbol{b} \qquad \textbf{(1.2)}$$

The vector $\boldsymbol{v}$ represents the fluid velocity, ρ_f and μ_f are respectively the density and the dynamic viscosity of the fluid and P is the pressure. The left-hand side of the Navier-Stokes equation account for the rate of change of the momentum, considering both the variation in time (acceleration term) and the variation in space induced reciprocally by the moving particles of fluid (convective term). The right-hand side of the equation describes the forces applied on the fluid that induce the change in the momentum, i.e. the pressure gradient ∇P, the diffusion term $\mu \nabla^2 \boldsymbol{v}$ which accounts for the viscous forces of a Newtonian fluid, and the body forces $\boldsymbol{b}$ acting on the fluid such as the gravity. The equations **(1.1)** and **(1.2)** must be completed by proper boundary conditions.

To model a structural domain characterized by an uncompressible material, it is only necessary to solve a governing equation that guarantee the conservation of momentum, as the conservation of mass is ensured by the incompressibility condition itself. The relation between

the deformations observed in the structure and the forces imposed by the fluid motion, is modelled as follow:

$$\rho_s \frac{\partial^2 \boldsymbol{d}}{\partial t^2} = \nabla \cdot \boldsymbol{\sigma}_s + \rho_s \boldsymbol{b}_s \qquad \textbf{(1.3)}$$

Where ρ_s is the solid density, $\boldsymbol{d}$ is the displacement vector, $\boldsymbol{\sigma}_s$ is the Cauchy stress tensor and $\boldsymbol{b}_s$ represent the body forces applied to the structure. The Equation **(1.3)** must be completed with a proper set of boundary conditions, especially on the surfaces shared with the fluid domain.

The coupling between the domain happens at the fluid-solid interface, where the continuity of kinematic and dynamic quantities is guaranteed through the imposition of two equations, one for the velocity and the other for the traction vector:

$$\boldsymbol{v}_f = \boldsymbol{v}_s \qquad \textbf{(1.4)}$$

$$\boldsymbol{\sigma}_f * \hat{n}_f = \boldsymbol{\sigma}_s * \hat{n}_s \qquad \textbf{(1.5)}$$

The vectors $\boldsymbol{v}_f$ and $\boldsymbol{v}_s$ are respectively the velocities in the fluid and the solid domain, $\boldsymbol{\sigma}_f$ and $\boldsymbol{\sigma}_s$ are the stress tensors, $\hat{n}_f$ and $\hat{n}_s$ are the normal to the fluid-structure interface. By multiplying the stress tensor by the normal the traction vector is obtained. As an alternative to the equation **(1.4),** the continuity between displacements in the two domains can be set.

2.2.3 Kinematic descriptions

The kinematic description is meant to describe the continuum motion with respect to finite mesh grid. The choice of a proper kinematic description determines the ability of the numerical method to deal with large distortions and provide an accurate resolution of material interfaces and mobile boundaries. There are two main approach that can be used for the description of motion, the Lagrangian description or the Eulerian description.

The Lagrangian description is based on the idea that the mesh grid moves according to the continuum motion. Each node of the computational mesh is associated with a material point for the total duration of the simulation, evaluating the kinematic and dynamic variations of that

specific particle. This approach is mainly applied in structural simulations and is particularly indicated for problems that imply materials with an history dependent behaviour.

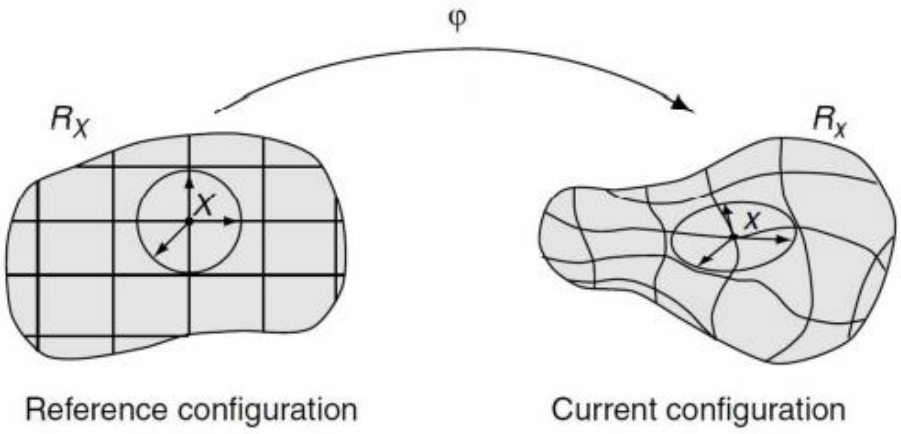

Figure 30 Correlation between reference and current configuration through the application φ.

The Lagrangian approach accurately tracks the material displacement, allowing to describe precisely free surfaces motion, however when large deformation of the domain occur the results can lose accuracy, due to the fact that the quality of the mesh is compromised by an excessive distortion. Large deformation often can lead also to convergence issues and simulation failure. The link between the spatial coordinates, $\boldsymbol{x}$, and the material ones, $\boldsymbol{X}$, can be expressed by the following law of motion:

$$\boldsymbol{x} = \boldsymbol{x}(\boldsymbol{X}, t) \quad t = time \tag{2.1}$$

The spatial coordinates depend on the material coordinates and on the time t, which is measured by the same variable in both the material and spatial domains. The correlation between the reference configuration and the current one is defined through the application φ as shown in Figure 30.

The Eulerian description presents a fixed mesh configuration, that is associated with a different material point at each time step. The physical quantities calculated at a certain location of the mesh grid are referred to the material point it is passing through it in that instant, so they do not depend on the initial configuration of the continuum but only on the current configuration and on the time t. This dependence is given by the following equality written for a general physical quantity f.

$$f = f(\boldsymbol{x}, t) \tag{2.2}$$

The Eulerian approach is usually implemented for fluid dynamic problems, as the control volumes generated by the fixed mesh grid allow to examinate the physical quantities of the fluid particles which are moving through the domain. It allows to deal with large distortions of the continuum, but at the expense of precise interface definition and resolution of flow details. Also, it introduces numerical difficulties, due to the fact that the relative motion of the continuum with respect to the mesh generates convective effects.

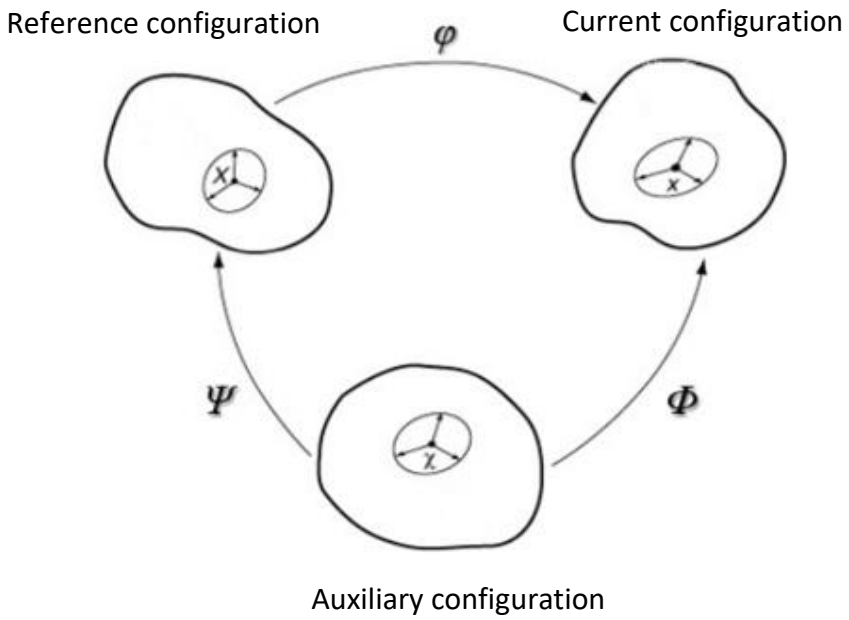

Figure 31 Correlation between reference, current and auxiliary configuration through the applications φ, ψ, Φ.

A third algorithm has been developed as a combination of the Lagrangian approach and the Eulerian one. It is called Arbitrary Lagrangian Eulerian (ALE) and is meant to summon the advantages of the two approaches, minimizing disadvantages. This approach is ideal for the FSI system as it permit to have a unique generalized kinematic description for both the fluid and structural domains. The mesh grid is not fixed, but at the same time it does not follow the continuum motion. The nodes position is optimized to have the best accuracy but at the same time minimize the convergence problem that large deformation can generate. A third domain is needed, the auxiliary configuration characterized by the auxiliary coordinates $\boldsymbol{\chi}$ is introduced to identify the grid points. It is related to the reference configuration and the current one respectively through the applications ψ and Φ, as shown in Figure 31. The fundamental ALE relationship for a random physical quantity $f(\boldsymbol{x}, t)$ is written as follow:

$$\left.\frac{\partial f}{\partial t}\right|_{\boldsymbol{X}} = \left.\frac{\partial f}{\partial t}\right|_{\boldsymbol{\chi}} + \frac{\partial f}{\partial \boldsymbol{x}} \cdot \boldsymbol{c} \qquad \textbf{(2.3)}$$

where $\boldsymbol{c}$ is the particle velocity with respect to the fixed mesh as seen from the auxiliary configuration. Equation **(2.3)** shows that time derivative of physical quantity in the reference configuration is given by the time derivative calculated at the auxiliary configuration, plus a convective term that accounts for the relative velocity $\boldsymbol{c}$.

The conservation equations of mass, momentum and energy can be rewritten in the ALE differential form by modifying the equations in the Eulerian form:

$$\left.\frac{\partial \rho}{\partial t}\right|_{\chi} + \boldsymbol{c} \cdot \nabla \rho = -\rho \nabla \cdot \boldsymbol{v} \qquad \textbf{(2.4)}$$

$$\rho \left(\left.\frac{\partial \boldsymbol{v}}{\partial t}\right|_{\chi} + (\boldsymbol{c} \cdot \nabla)\boldsymbol{v} \right) = \nabla \boldsymbol{\sigma} + \rho \boldsymbol{b} \qquad \textbf{(2.5)}$$

$$\rho \left(\left.\frac{\partial W}{\partial t}\right|_{\chi} + \boldsymbol{c} \cdot \nabla W \right) = \nabla \cdot (\boldsymbol{\sigma} \cdot \boldsymbol{v}) + \boldsymbol{v} \cdot \rho \boldsymbol{b} \qquad \textbf{(2.6)}$$

where, ρ denotes the mass density, $\boldsymbol{v}$ is the material velocity vector, $\boldsymbol{c}$ is the relative velocity, $\boldsymbol{\sigma}$ is the Cauchy stress tensor, $\boldsymbol{b}$ is the specific body force vector and W is the specific total energy. The right-hand side of the three equations is written in classical Eulerian form, while the arbitrary motion of the computational mesh is only reflected in the left-hand side, where the convective velocity $\boldsymbol{c}$ is observed and the time derivative is referred to the auxiliary domain. For this reason, the ALE approach is also known as the quasi-Eulerian description.

A comparison between Lagrangian, Eulerian and ALE description is reported in Figure 32.

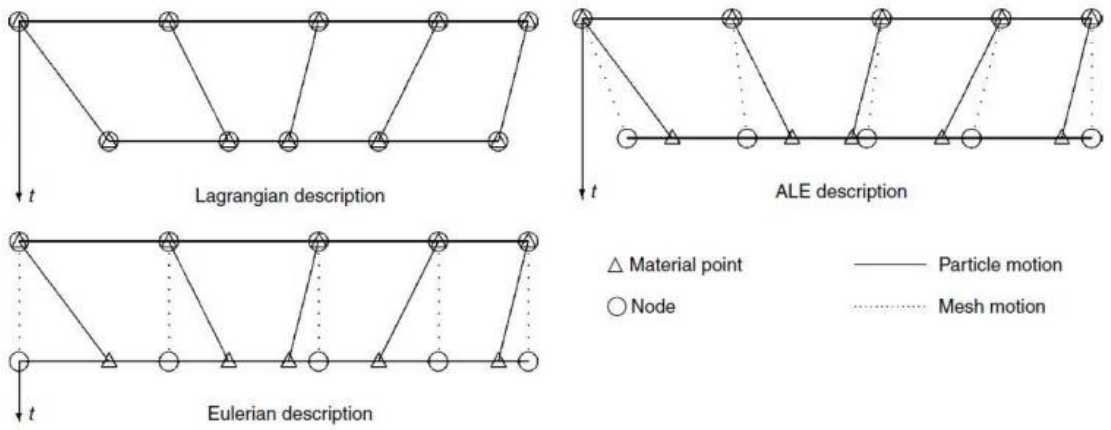

Figure 32 One dimensional example of Lagrangian, Eulerian and ALE mesh and particle motion.

2.3 Boundary conditions

The aorta is a complex system that can be modelled in several different ways. The choice of the models to implement and the parameters to set for the description of the physical properties is not unique and should be optimized to guarantee the adherence to reality, lowering as much as possible the computational cost. In particular, the choice of appropriate boundary conditions that allow to reproduce accurately the hemodynamic patterns in the aortic vessel is fundamental. Multiple approaches can be used, but in the last decade, the coupling of 0-D or 1-D lumped parameter models with the 3-D fluid domain has been demonstrated to be an effective way to reproduce realistic flow rate and pressure fields at the outlets [43-45]. Wiendkessel model, that is the most common one, parametrize the systemic circulation downstream the outlets through two resistances and one compliance. Studies have demonstrated the results obtained by coupling the computation domain with lumped parameter models present a much higher coherence with the in vivo data, compared to the results obtained when a fixed flow division or a constant pressure values are imposed at the outlets [46-48]. However a good accuracy can be obtained also by using patient specific pressure waveforms at the outlets [[48]].

In this context, the start-up Computational Life Inc, Delaware, developed a multi-scale mathematical model of the whole cardiovascular system (starting from previously validated models [49-52]), which is able to predict physiological and pathological flow related quantities. A viscoelastic, one-dimensional model (1D) of the main arteries and veins belonging to both systemic and pulmonary circulation, was combined with compartmental models that simulate microcirculation and heart chambers to create a closed network that includes 388 vessels and 137 compartments. Using this model, it is possible to study and analyse pressure and flow waveforms propagation, variation of vessels' cross-sectional area and blood speed throughout the entire network of arteries and veins, as well as pressure and volume of each cardiac chamber and microcirculation region.

The system of equations on which one-dimensional modelling relies is the following:

$$\begin{cases} \partial_t A + \partial_x Au = 0 \\ \partial_t (Au) + \dfrac{A}{\rho}\partial_x p + \partial_x (Au^2) = -\dfrac{f}{\rho} \end{cases} \qquad \textbf{(3.2)}$$

where x is the axial coordinate along the longitudinal axis of the vessel, t is time, ρ is the blood density, f is the friction force per unit length, A is the cross-sectional area of the vessel and p is the average internal pressure over a cross-section. The closure of the system is achieved by the adoption of a viscoelastic tube law to relate blood pressure to vessels' cross-sectional area (further details in [49, 53]). The system **(3.2)** and the viscoelastic tube law have been written in quasi-conservative formulation and resolved with a numerical method based on the path-conservative framework proposed by Pares [54] and on the Roe-type HEOC solver for the generalized Riemann problems proposed by Castro and Toro 2014 [55]. A summary of the numerical method can be found in Toro et al. 2019 [56].

The resistance R, the compliance C, and the fluid inertia L, of the microcirculatory regions peripheral to the 1-D domains were simulated using the three-element (RCL) Windkessel/inertial model shown in the following Figure 33.

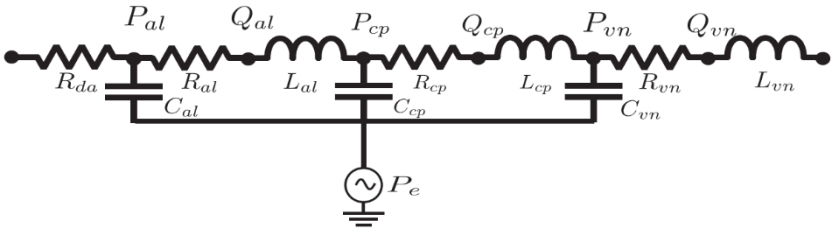

Figure 33 Modelling of microcirculation regions (al=arterioles, cp=capillaries and vn=venules, da=distal arteries) as RCL complexes [50].

The pressure and volume dynamics of the four cardiac chambers were computed in our model according to the equations introduced by Burkoff et al. [57, 58] . The equation that describes the pressure and volume dynamics of the four cardiac chambers is the following:

$$P(t,V) = P_{ed}(V) + e(t)\big(P_{es}(V) + P_{ed}(V)\big) \qquad \textbf{(3.3)}$$

where $e(t)$ is a time-varying function that allows the modification of the dynamics between diastolic and systolic states, V is the volume at the current time step, $P_{es}(V)$ and $P_{ed}(V)$ are two functions describing the end-systolic and end-diastolic PV dynamics, expressed by the equations **(3.4)** and **(3.5)** respectively.

$$P_{es}(V) = E_{es}(V - V_0) \quad \textbf{(3.4)}$$

$$P_{ed}(V) = \alpha(e^{\beta(V-V_0)} - 1) \quad \textbf{(3.5)}$$

where E_{es} is the end systolic elastance, V_0 is the volume in the initial configurations and α, β are coefficients.

The main features of the dynamics that develop in a healthy scenario are well captured by this model, which has been validated by comparing numerical predictions with data reported in the literature and some in vivo measurements (see Figure 34 for details). Starting from the healthy scenario, it is than possible to model other pressure levels. The hypotension condition can be obtained imposing a reduction in the resistances of the compartments corresponding to systemic arterioles (R_{al}, -50% with respect to the healthy scenario) and decreasing the left ventricular systolic elastance (E_{es}, -35% with respect to the healthy scenario). The hypertension condition, instead, can be obtained by increasing the peripheral resistances of the 1D models of the systemic arteries (R_{da}, doubled with respect to the values used to simulate the healthy human) and the stiffness of the systemic arteries (+50%); the cardiac parameters were left unchanged.

(a)

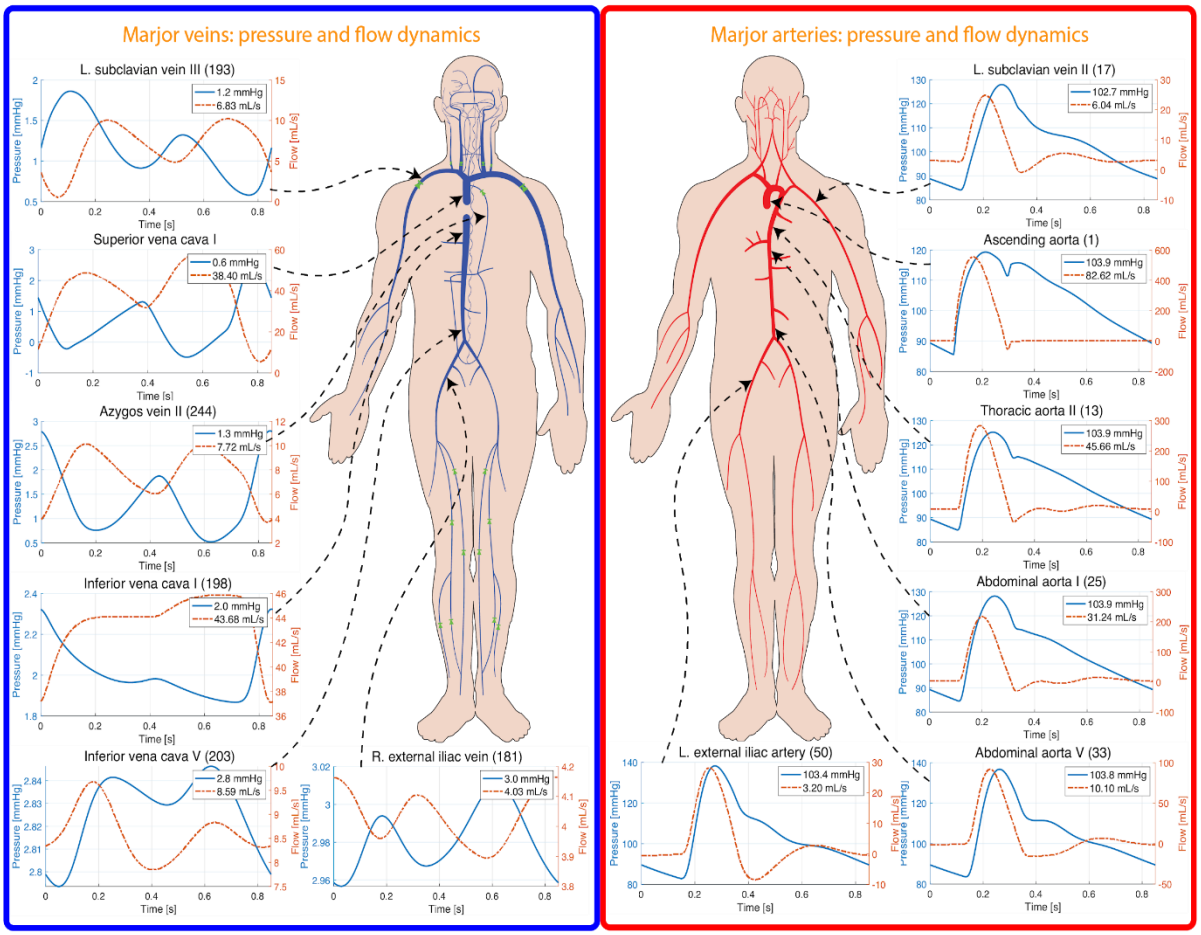

(b)

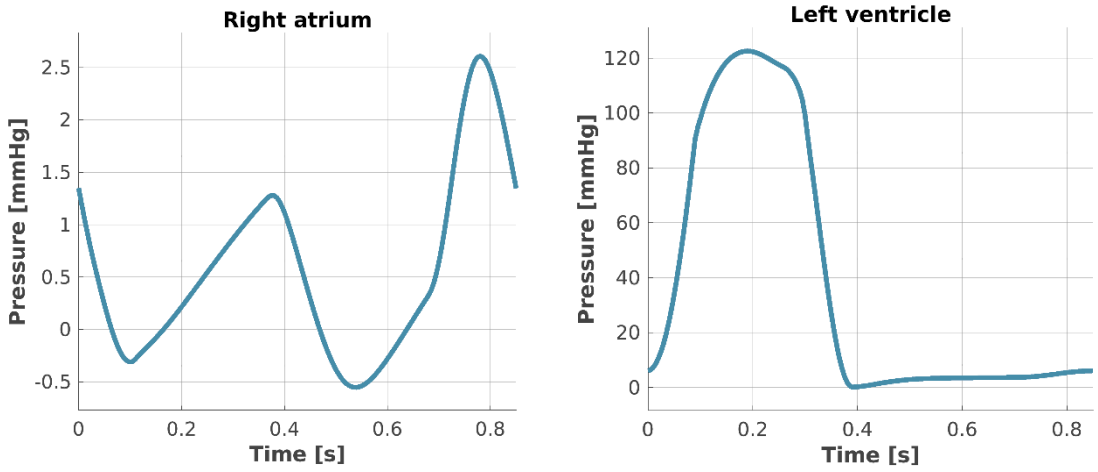

Figure 34 Pressure and flow dynamics predicted by the cardiovascular model developed by Computational Life in a healthy human. (a) Blood pressure and flow dynamics in the major veins (LEFT) and arteries (RIGHT) of the systemic circulation. (b) Pressure waveform inside the right atrium (LEFT) and left ventricle (RIGHT). Inside the legend of each plot are reported the mean pressure (blue line) and the mean flow rate (red line) of the corresponding vessel.

2.4 FSI studies of the aorta

The studies that use FSI for aortic modelling are increasing. The choice of FSI over CFD for fluid dynamics assessment presents several advantages, such as the possibility to model the compliant behaviour of the aorta and to find the values of the stresses and strains imposed at the aortic wall. Multiple studies [59-63] focus on comparing the CFD and FSI numerical approaches, through the calculation of physical quantities like velocity and WSS. It has been observed that CFD tends to overestimate WSS values, especially in the ascending aorta where significant wall deformation occur leading to a diameter change of 10-15 % between systole and diastole [59, 60]. Moreover, differences in the WSS spatial and temporal gradient can occur [59]. In general FSI present a higher level of accuracy [62], a characteristic that can be essential for some type of investigations.

The relevant quantities that are usually calculated in the FSI studies of the aorta are WSS, velocity and pressure in the fluid domain, and stresses and strains in the structural one. Numerous analysis evaluate how these parameters are affected by pathological conditions[64, 65], anatomical configuration[28, 66], or wall properties [67-69]. For example, it has been observed that patients with bicuspid aortic valve (BAV) present increased flow helicity and eccentric blood flow jet angle at the entrance with respect to subjects with a normal tricuspid aortic valve (TAV) [64]. Results obtained for geometries with aortic aneurysm, instead, shows increased wall stresses owing to wall stiffening, and decreased WSS caused by recirculation patterns in the dilatated aorta [65]. Other studies calculate hemodynamic and structural quantities in order to assess how they affect the aortic wall properties and try to predict eventual complications, such as dissection and rupture [43, 65, 70, 71]. In particular it has been shown that elevated WSS correspond to the location at which tear formation can occur[28, 72]. For the purpose of this study the correlation of aortic hemodynamic and structural mechanics with AD initiation and propagation is crucial; for this reason, a deeper insight on the result obtained by researchers on this topic will be reported below.

Pasta et al. [65] developed a 2-way FSI model to evaluate how the hemodynamic in dilatated aortas is influenced by BAV and TAV morphology and to assess how it affect further aneurysm dilatation or dissection initiation. Five patient-specific geometries were obtained through segmentation (two BAV and three TAV) and two layers characterized by different material properties have been modelled at the aortic wall. They hypothesize that aneurysm dilatation happens in correspondence of high WSS while AD initiation occurs when peak wall stresses (PWS) outgrow the adherence forces between the two layers.

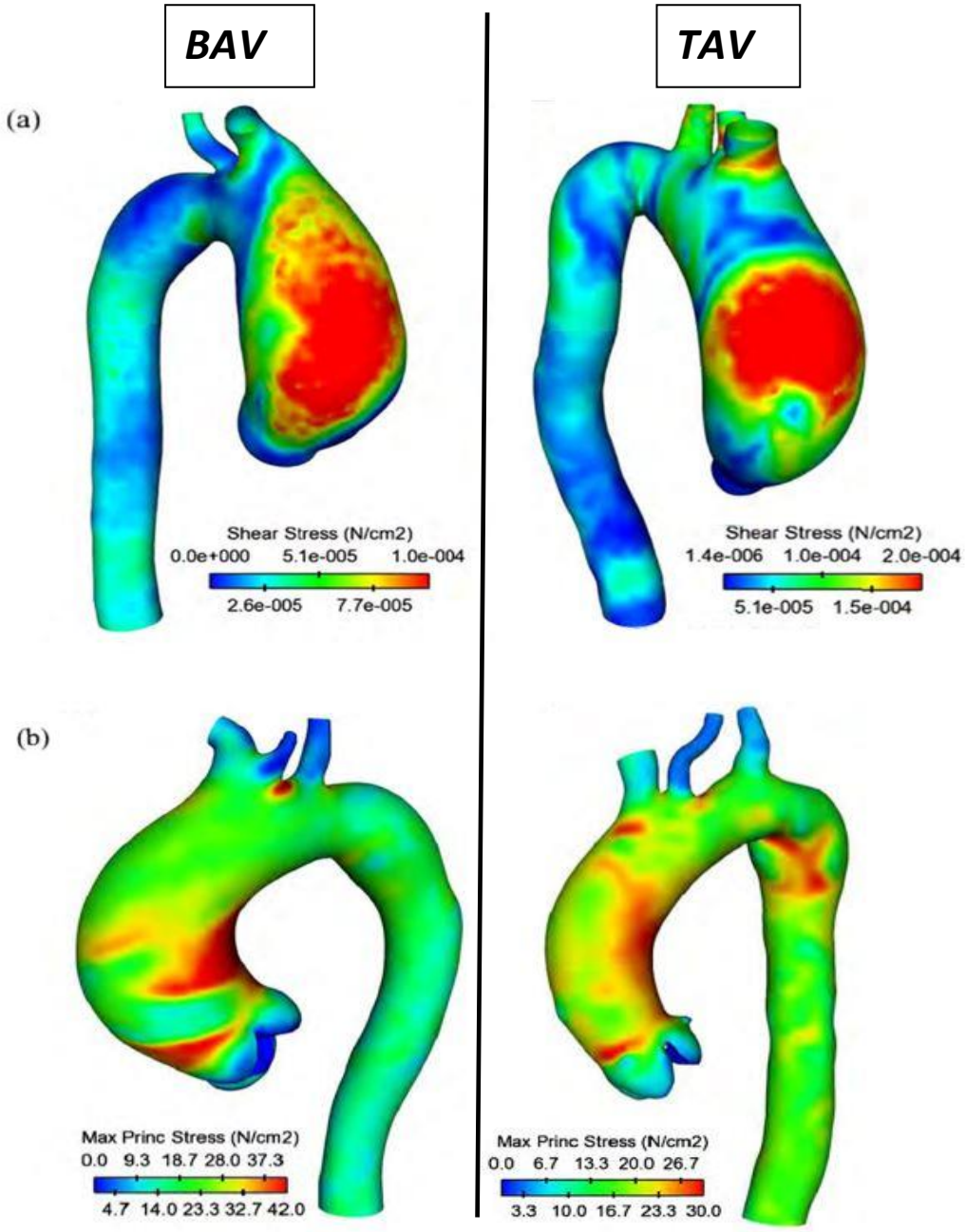

Figure 35 Comparison between the results obtained for BAV and TAV patients. (a) Comparison between WSS distribution. (b) Comparison between PWS distribution.

Maximum WSS were observed in the anterolateral region both for BAV and TAV patients, with the only difference that BAV patients present a larger extension of the areas characterized by maximum WSS (Figure 35, a). These findings suggest that anterolateral region of aneurysmal aorta is critical for aneurysm development and enlargement. Local maxima of PWS occurred on either the anterolateral or posterolateral regions of the ascending aorta. These results are consistent with clinical observations of AD location, indeed type A dissection frequently develop above sinotubular junction. High maximum principal stress can be observed even in the aortic arch distal to the ostia of the supra-aortic vessels, exactly where type B dissections frequently occur. The maximum principal stresses observed for the BAV patients are slightly higher, suggesting they are more at risk of AD development (Figure 35,b). The discussed results are obtained at the systolic peak.

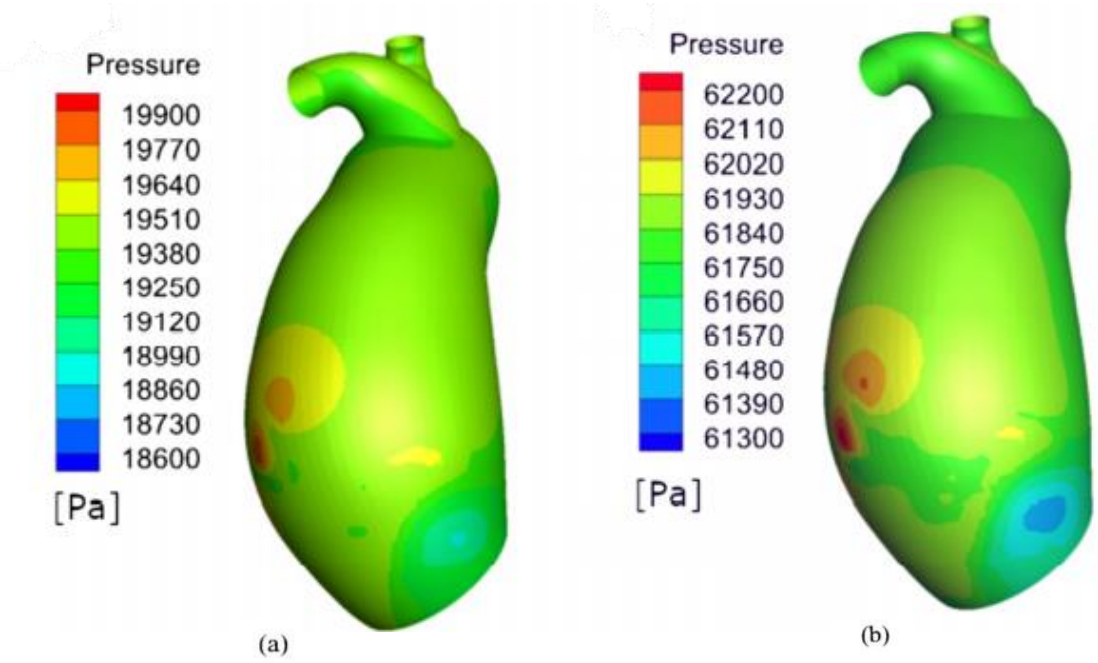

Figure 36 Comparison between pressure values calculated with E = 10 MPa and R = $1.69 * 10^9\ kg \cdot m \cdot s^4$ *(a) or* $R = 1.69 * 10^{10}\ kg \cdot m \cdot s^4$ *(b).*

Campobasso et al. [43] set up a 2-way FSI simulation in order to evaluate the role played by peripheral resistance variation on the PWS measured at the aortic wall for different stiffness values, in a geometry presenting ascending aorta aneurysm. Four different cases were identified through the combination of two different stiffness value ($E = 2\ MPa$ and $E = 10\ MPa$) and two different peripheral resistance values ($R = 1.69 * 10^9\ kg \cdot m \cdot s^4$ and $R = 1.69 *$

$10^{10}\ kg \cdot m \cdot s^4$). Changes in the peripheral resistance significantly affect the PWS and the pressure values when the wall is stiffer. Indeed the pressure increase from a maximum of 20 kPa to a maximum of 62 kPa (3 times higher) (Figure 36) and the PWS go from 105 kPa to 702 kPa (7 times higher). These results suggest that patients with aortic aneurysm that experiment a sudden increase in the peripheral resistance have a higher probability to experience AD or the rupture of the aneurysm. For the more compliant wall instead the difference is much lower as the vessel has a better ability to adapt to the new fluid dynamic conditions. The reported results referred to the systolic peak (0.2s). In all cases the PWS were observed on the anterior or posterior region of the ascending aorta, with the values slightly higher on the posterior area. These results are consistent with the ones obtained by Pasta et al.[65].

Chi et al. [28] set up a CFD simulation to they establish a relationship between aortic morphology and tear location of type A AD. Seven patient-specific geometry were selected, five of them presented AD or aortic enlargement, while two are taken from a healthy subject. The pre-dissection or pre-dilation geometries were reconstructed through image processing procedures, then CFD simulations were run in order to find the location of WSS peak values in the different geometries. It is expected that the maximum values of WSS correspond to the tear location. Results show that the WSS values increase proportionally with the diameter dimension and that the diameter of the patient that experienced AD were much higher than the ones associated with the geometries of the control patients (Table 4).

	AD Group					Control Group	
	Subject 1	Subject 2	Subject 3	Subject 4	Subject 5	Subject 1	Subject 2
High WSS region one (Pa)	12.46	9.26	11.95	9.18	8.87	5.58	5.77
High WSS region two (Pa)	13.35	10.00	8.19	4.43	3.89	2.48	6.51
High WSS region three (Pa)	13.44	10.32	11.95	5.37	18.50		3.06
Diameter at ascending aorta (mm)	49.36	45.64	46.20	28.23	31.72	25.00	25.67

Table 4 Wall shear stress value at the high WSS region and the diameter of ascending aorta for all subjects.

Other than that, it was observed that the deflection angle of the supra-aortic vessels with respect to the aortic arch has an influence on the WSS values at the bifurcation: the lower is the angle the higher are the WSS measured. All the patients that experienced dissection present at least one angle that measure between 45 and 60 degree, while the control patients present branches deflection angle of 75 degrees or more.

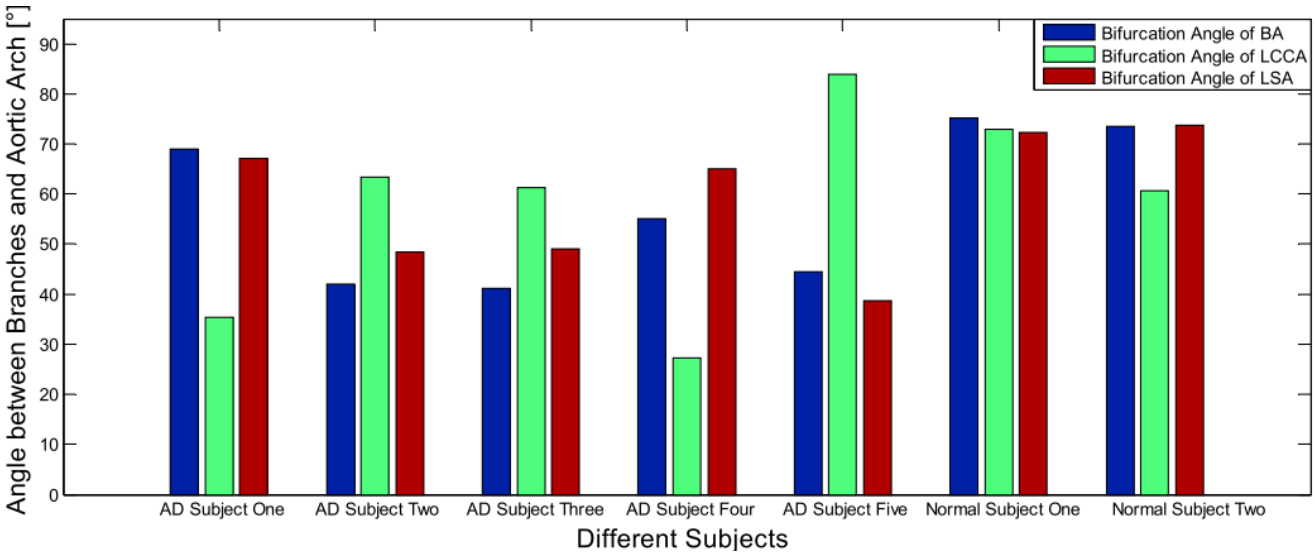

Figure 37 Comparison of the bifurcation angles between AD subjects (1–5) and normal subjects (normal subject 1 and 2).

Finally, the aortic arch tortuosity is shown to have a role in increasing the risk for AD. According to this paper the WSS threshold value at which tear formation can occur is of 10 Pa; the results are coherent with this theory as the WSS peak values for the control patients are always below this threshold while for the AD patients they reach vales around 12-13 Pa.

The mentioned studies are not sufficient to explore the relation between aortic hemodynamic and AD, a lot of aspects have still not been considered and others need further examination. To the author's knowledge, the correlation between different boundary conditions and the location of a possible dissection tear has not been discussed yet. Both Pasta et al. [65] and Chi et al. [28] investigations consider only flow rate and pressure curve associated to a healthy patient, with normotensive pressure values; Campobasso et al. [43], instead, modelled the hypertensive condition by varying the peripheral resistance, but it only compared the WPS to assess the risk level of AD onset, without looking at the WSS patterns. Moreover, the correlation between morphology and tear location needs further investigations that go beyond the results obtained by the Chi et al. study. The evaluation through the FSI computational tool and the exploration of other anatomical configurations can give a better insight on the topic. Campobasso et al. [43] used a CILCA configuration of the aortic arch but no comparison was made with the standard configuration nor the effect of this morphological feature on the WSS was evaluated. Starting from these considerations the current work has been developed.

2.5 Objectives

The aim of this thesis work is to implement multiple 2-way FSI simulations to assess the impact of different boundary conditions and different aortic arch geometries on the local stress concentrations and fluid disturbances that could facilitate AD formation and propagation. Two geometries of non-dilatated aortic vessel are considered, one presents the CILCA configuration at the aortic arch while the other presents the common configuration. Three sets of boundary conditions will be applied for each geometry, i.e. the normotensive, the hypertensive and the hypotensive condition. A total of six simulations will be performed and analysed, and the results will be compared between the two geometries when the same boundary conditions type is applied or for different boundary conditions within the same model. In detail two objectives have been identified for the comparison of the two geometry configurations and two for the different boundary conditions:

- Comparison of the WSS-based descriptors calculated at the outer wall of the aortic arch of the two configurations. Higher descriptors values are expected in the bovine arch configuration at the BCT, both at the entrance of the vessel and at the location where the LCCA depart.
- Comparison of the hemodynamic patterns in the aortic arch and in the supra-aortic vessel of the two configurations. A lower flow rate and a greater vorticity are expected to be observed in the carotid vessel of the bovine arch configuration.

- Comparison of the hemodynamic patterns in the aortic lumen for the different boundary conditions, in particular in the ascending aorta where a jet flow impingement is usually observed on the anterior region and at the end of the aortic arch where a significant vorticity is usually assessed which can lead to tear formation.
- Comparison of the maximum principal stresses at the wall for the different boundary conditions, to determine whether they affect the areas in which the AD tear could propagate or not. The boundary conditions are supposed to influence more the magnitude of the stresses than their distribution.

3 Materials and Methods

In this chapter the setting process of the FSI system is discussed. In particular, it is presented the process for the preparation of the computational domain, (segmentation and meshing), the choices made for the numerical implementation of the physical problem in Fluent and Mechanical APDL, and the WSS-based descriptor necessary for the post-processing phase.

3.1 Introduction

2-ways FSI simulations have been performed in ANSYS Workbench, applying ANSYS Fluent for fluid dynamic simulations and Mechanical APDL for the structural analysis. The solvers interact through the System Coupling component and the results were analysed by CFD-Post. In Figure 38 a schematic representation of the workflow applied for each simulation is reported. Three phases can be identified: the pre-processing phase in which the computational domain is extracted from medical images and discretized through meshing, the simulation phase in which FSI is actually performed, and the post-processing phase for the results processing. A comprehensive description of each of the steps is reported in the next paragraphs.

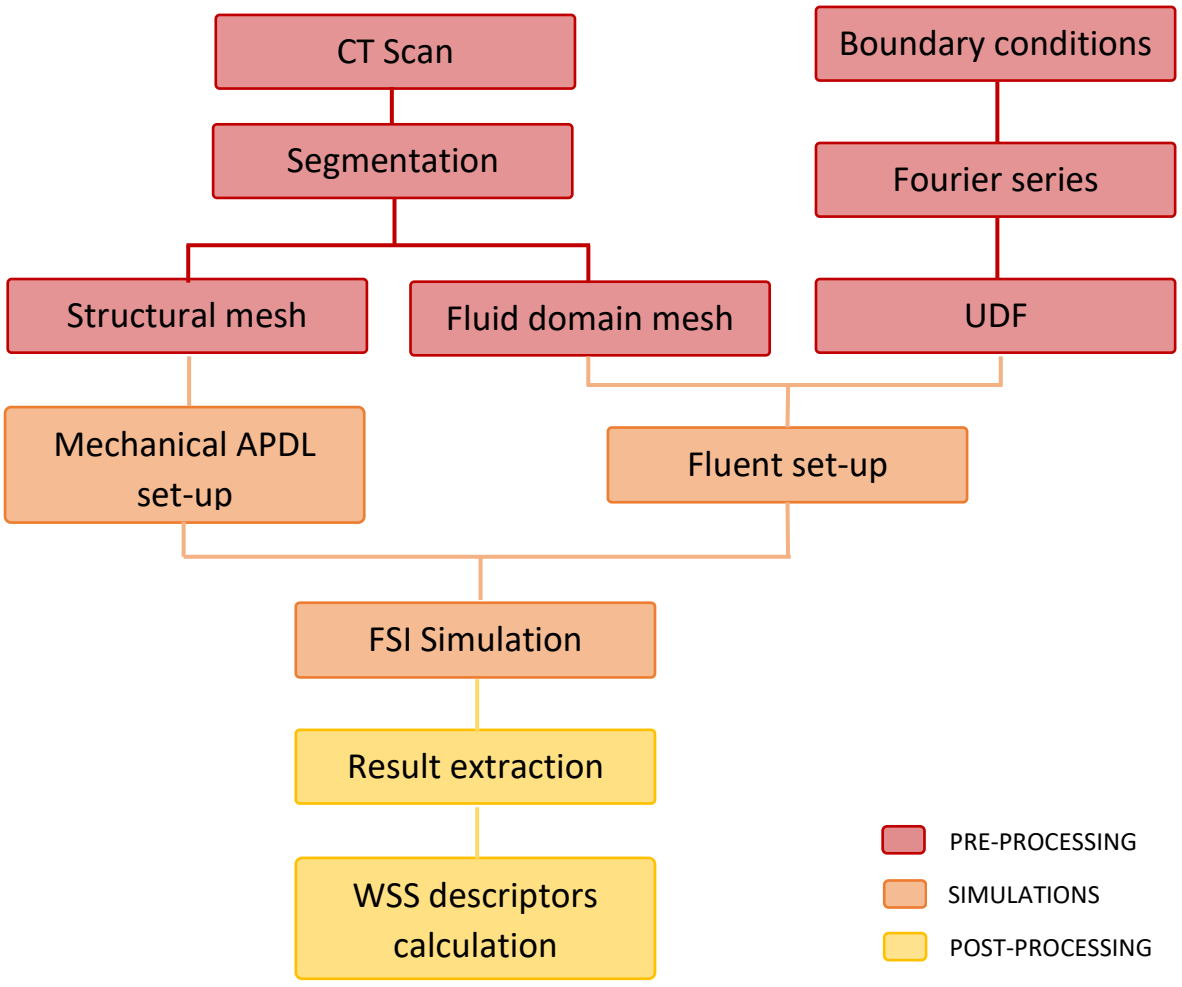

Figure 38 Schematic representation FSI workflow

3.2 Patient-specific geometry reconstruction

Patient-specific domains can be reconstructed through the segmentation of medical images. Two patients were chosen in a pool of CT images collected at the Policlinico San Donato in Milan, one with a standard configuration of the aortic arch and one with a type 2 bovine arch configuration. The subjects did not present any aortic wall pathology at the moment the images were acquired and no follow-up on their conditions is available. The segmentation of the standard configuration had already been performed, and the STL file containing the 3D reconstruction of the healthy aorta was provided directly. Two independent experts realized a binary mask of the aorta through itk-snap, 3D slicer and Materialise Mimics software, which than have been combined through the STAPLE algorithm [73]. The segmentation of the bovine arch configuration, instead, was made by the author using the 3D Slicer software. A semi-automated segmentation process, based on greyscale thresholds and manual correction, guided the definition of a 2D mask on each CT slice. The aortic lumen was identified in some slices of the CT image by panting them (Figure 39), then the tool *growing from seeds* was used to compute the full segmentation. This tool fills the voids between the painted areas and define the boundaries of the computational domain, placing them where an abrupt change of the pixel intensity occurs. A refinement of the binary mask obtained can be made by imposing threshold values on the pixel intensity that should be considered, or by re-drawing manually the boundaries where they are not precise.

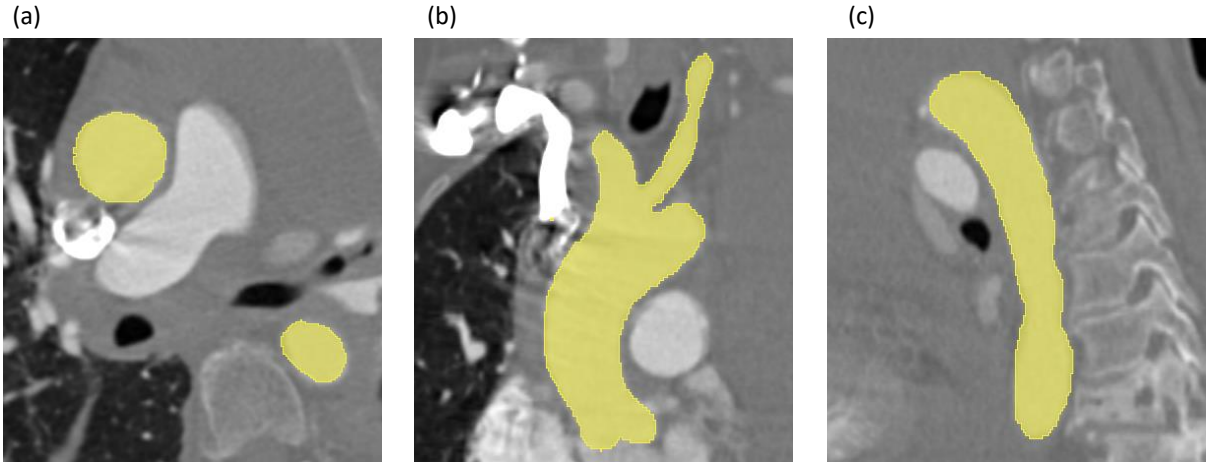

Figure 39 Aortic arch identification on CT Scan slices. (a) CT Scan slice in the horizontal plane. (b) CT Scan slice on the frontal plane. (c) CT Scan slice in the lateral plane.

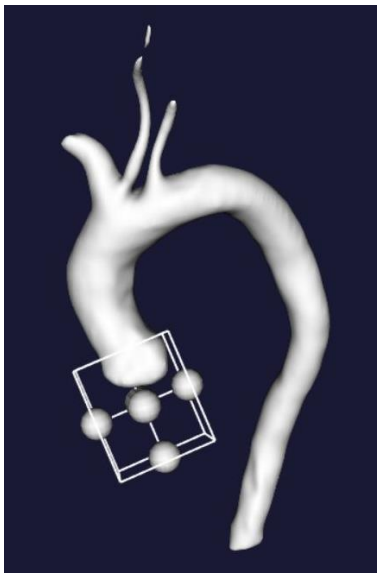

Figure 40 Clipping tool in VMTK applied to bovine arch configuration.

The segmented geometry was imported in VMTK (the Vascular Modelling Toolkit [74]), a collection of tools and libraries for vascular images processing. The terminal section of the geometry were clipped in order to open the computational domain, preparing it for subsequent meshing. The clipping was performed manually using a cube in which should be placed the portion of the geometry that need to be clipped (Figure 40). The clipping surface should be orthogonal to the centreline, so that in the FSI analysis the velocity vectors imposed at the boundaries will be parallel to the vessel axis. No flow extensions were added, the supra-aortic vessel were considered long enough to guarantee the flow is sufficiently developed. The reconstructed geometry are shown in Figure 41.

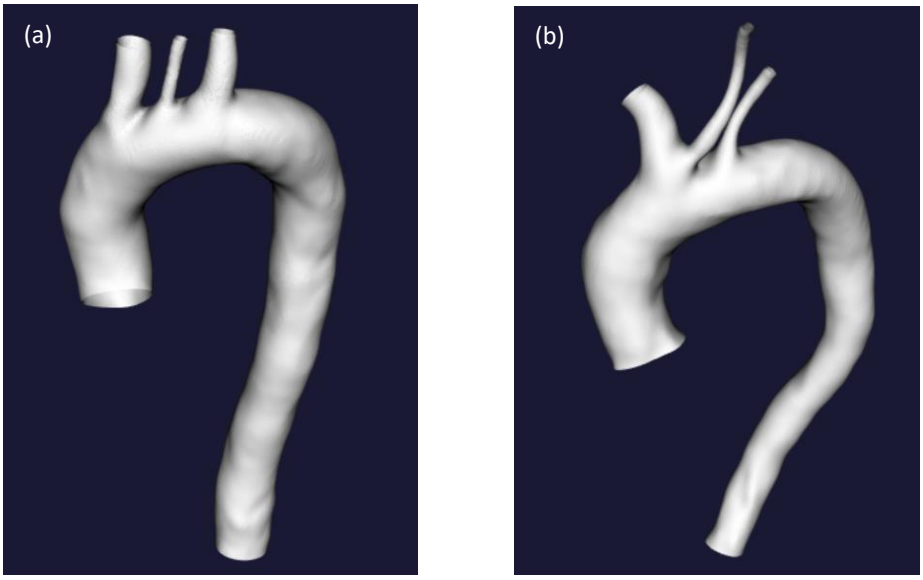

Figure 41 Computational domains extracted. (a) Standard configuration and (b) bovine arch configuration.

3.3 Mesh generation

The discretization of the computational domain is fundamental for the numerical solution of the governing equations in both domains. A grid is created by dividing the geometry in small volumes called cells, which can have different shapes. The most common type of cells are the hexahedral and the tetrahedral, which constitute respectively the so-called structured and unstructured meshes. Structure grid, in which cells are organized in arrays, are associated to high convergence and result accuracy, but present a limited flexibility and are not able to capture complex morphological details. The unstructured grid are suitable for complex geometries and present a greater mesh refinement capability, with the only drawback of an increased computational cost. When one dimension is much smaller than the other two, shell elements can be used, which allows to significantly reduce the computational cost. The conventional shell elements, indeed, discretized the geometry by reducing it to a reference surface. The choices made in this study for the discretization of the fluid and solid domains are described in the next paragraphs.

3.3.1 Fluid domain

The fluid domain model was imported and meshed in ICEM, the meshing tool embedded in the ANSYS Workbench. A tetrahedral mesh was created using an Octree method, that is based on a top-down meshing approach. This means that first a coarse mesh that encloses the geometry is created based on the given sizing parameters, then recursive spatial subdivision of the elements occur in order to capture curvature and complex morphologies. This approach ensures refinement of the mesh where necessary, but maintains larger elements where possible, allowing for faster computation. A surface mesh is created for each of the boundaries and all the nodes that cannot be match with a material point are eliminated. Finally, the mesh is smoothed by moving nodes, merging nodes, swapping edges and in some cases, deleting bad elements. Because the regions next to the aortic wall are characterized by elevated gradients of fluid dynamic quantities, five prism layers were implemented next to the wall to improve the accuracy. The layer expands away from the wall with an expansion ratio of 1.2. The generation of a hybrid mesh with tetrahedral core and prismatic elements at the near wall region represents a good compromise between the accuracy of a structured mesh and the refinement of an

unstructured mesh. A smoothing process was iteratively applied to the generated mesh in order to improve the quality of the elements. The threshold value at which the mesh was considered acceptable is a quality of 0.2.

The mesh size strongly influences the results accuracy and the computational cost of the simulation. To optimize the cells dimension, a mesh sensitivity analysis is performed, trying to find the coarser possible mesh that gives an acceptable accuracy, which guarantees the minimization of the simulation computational cost. For the standard configuration, twelve different mesh sizes were computed by changing the scale factor option in ICEM. In particular the coarser mesh obtained presents 300 thousand elements while the finer one is constituted by 5 million elements. For the bovine configuration, instead, only eight different meshes were created, assuming that a similar dimension to the standard case would be necessary to obtain a good accuracy and so avoiding studying meshes with a greater number of elements. For each mesh, a steady state simulation was run in ANSYS Fluent aiming to collect the WSS values (both the mean value and the maximum one were taken into consideration). The average value of the velocity over the cardiac cycle was assigned at the inlet, while an outflow boundary condition was set at the outlets, imposing a flow division of 63% at the descending aorta, 9% both at the LCCA and the SCA, and 19% at the BCT. Assuming the results obtained for the finer mesh are the most accurate, the relative percentage difference with respect to that mesh was assessed through the following formula:

$$E(j) = \frac{\left|WSS(j) - WSS_{fine}\right|}{\mathrm{WSS}_{fine}}\% \qquad \textbf{(3.1)}$$

A threshold value of 5% was established to consider the mesh sufficiently accurate. The results obtained are shown in Figure 42 for the standard configuration of the aortic arch, and in Figure 43 for the bovine arch configuration. For each of the quantities of interest the WSS and the E(j) values are reported on the left figure; furthermore the relative percentage difference E(j) was represented through a graph on the right figure, to highlight when the convergence to the 5% threshold is reached. It is expected that the graph reach a plateau and does not oscillate over the threshold value from that point on.

In the standard configuration, the mean WSS graph reached convergence for a mesh of 700 thousand elements, suggesting this mesh is the best compromise between accuracy and computational cost. The maximum WSS analysis was, instead, inconclusive as the results continue to increase with the number of mesh elements without reaching a plateau. By mapping the WSS on the aortic geometry, it was observed that the maximum value were located next to the boundaries. The values calculates in those areas are not reliable as they can be affected by systematic errors in the setting; for example if the inlet surface is not exactly perpendicular to the centreline of the vessel, the velocity vector might impose a higher stress at the wall as a consequence of flow impingement. In order to overcome these imprecisions that compromise the mesh sensitivity analysis, the 99th percentile was considered. A percentile is a statistic measure that expresses the value under which a certain percentage of the results fall. In this case, the 99th expresses a WSS value such that 99% of the elements present a WSS value equal or lower than the one expressed by the percentile. In this way a value close to the maximum was calculated without considering the compromised values measured at the boundaries. The results, reported in Figure 42/c , are consistent with the ones obtained for the mean WSS, leading to the choice of the mesh with 700 thousand elements for the FSI simulation.

(a)

scale factor	elements	mean WSS (Pa)	E mean (%)
1.5	425916	0.1474891	7.743604596
1.3	588191	0.1502988	5.986099843
1.2	706119	0.15713806	1.70805167
1.1	866722	0.15539007	2.801442684
1	1083962	0.15933131	0.336144599
0.9	1386008	0.15931877	0.343988536
0.8	1836547	0.15940644	0.289149784
0.7	2530072	0.15968112	0.117333787
0.65	3033460	0.15996247	0.058654383
0.6	3680578	0.16014836	0.174931053
0.55	4561902	0.16032144	0.283194897
0.5	5776662	0.1598687	0

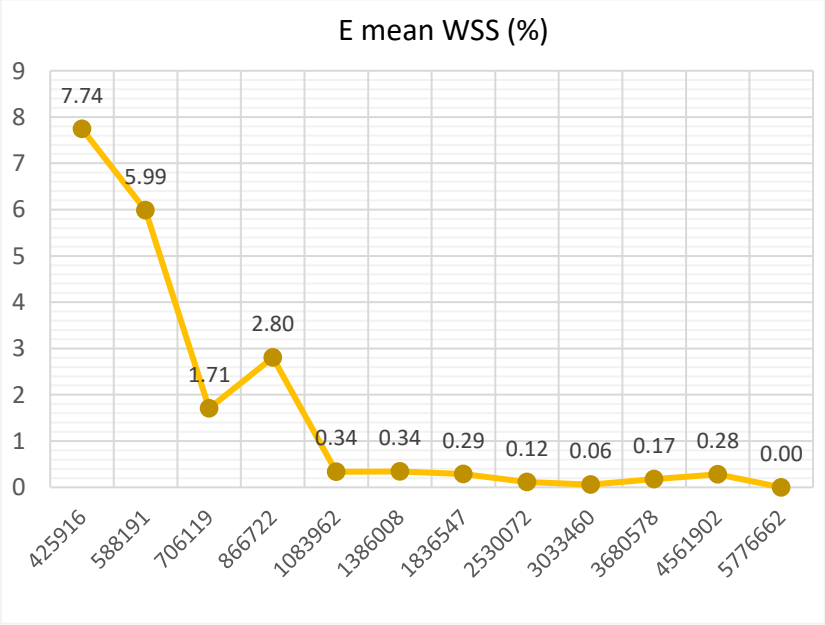

(b)

scale factor	elements	max WSS (Pa)	E max (%)
1.5	425916	3.571468	32.68034093
1.3	588191	3.486729	34.27761146
1.2	706119	3.7627425	29.07495117
1.1	866722	3.7738233	28.86608589
1	1083962	3.6780324	30.67167696
0.9	1386008	3.7749872	28.84414719
0.8	1836547	3.5635765	32.82909015
0.7	2530072	3.6479118	31.23942908
0.65	3033460	4.0926776	22.85590667
0.6	3680578	4.4960923	15.2518234
0.55	4561902	5.011764	5.531774655
0.5	5776662	5.3052378	0

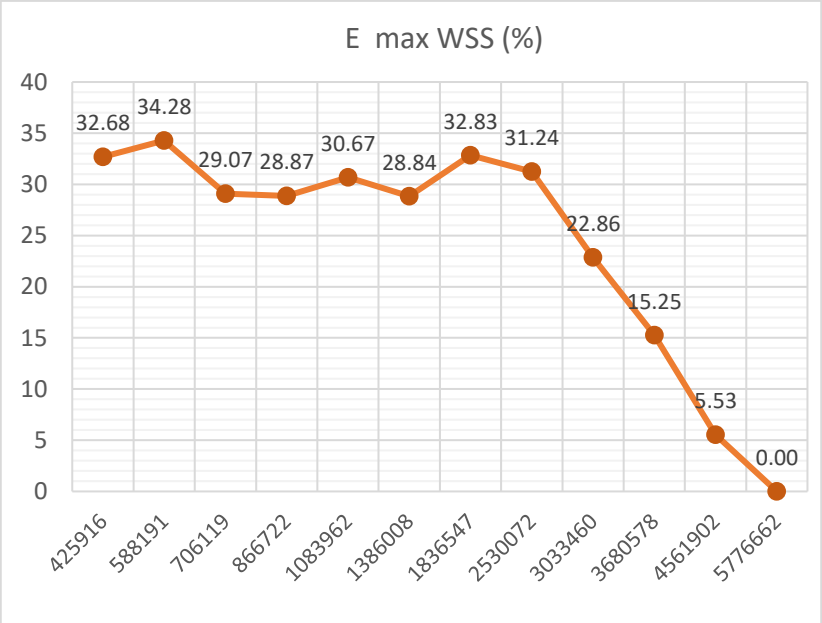

(c)

scale factor	elements	99_perc (Pa)	E 99_perc (%)
1.5	425916	1.509509773	12.73932456
1.3	588191	1.603860071	7.28518914
1.2	706119	1.670613768	3.426338526
1.1	866722	1.662210086	3.912132632
1	1083962	1.65123019	4.546850744
0.9	1386008	1.675975727	3.116378165
0.8	1836547	1.707199753	1.311401713
0.7	2530072	1.727938505	0.112550597
0.65	3033460	1.730795663	0.052614006
0.6	3680578	1.718712398	0.64588685
0.55	4561902	1.718712398	0.64588685
0.5	5776662	1.729885501	0

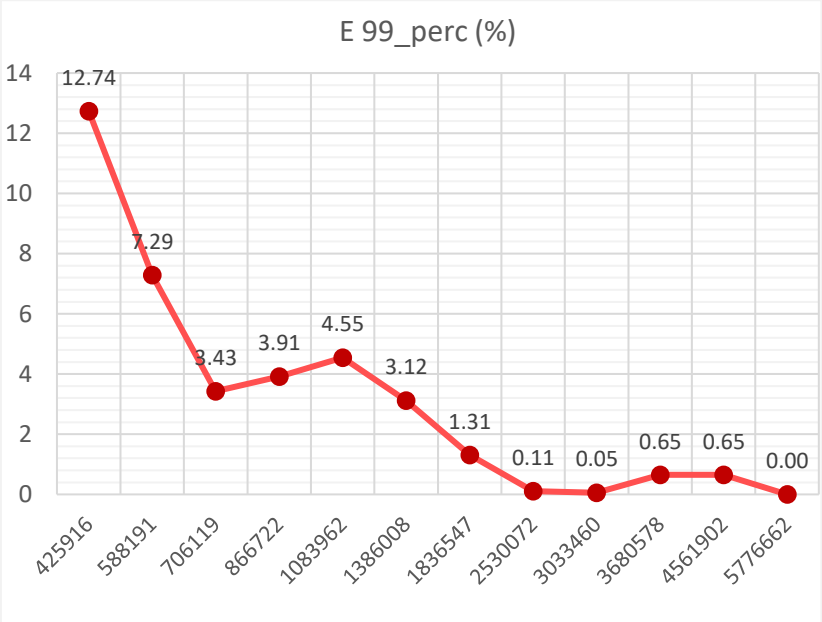

Figure 42 Sensitivity analysis standard configuration. (a) Mean WSS values and associated relative percentage difference (LEFT), mean WSS relative percentage difference as a function of mesh elements (RIGHT). (b) Max WSS values and associated relative percentage difference (LEFT), max WSS relative percentage difference as a function of mesh elements (RIGHT). (c) 99th percentile of the WSS and associated relative percentage difference (LEFT), 99th percentile relative percentage difference as a function of mesh elements (RIGHT).

Similar considerations were made for the study of the bovine arch case. The maximum WSS did not increased steadily but instead presented an oscillatory pattern; the result is still inconclusive so again the 99th percentile was calculated. The mesh chosen for the FSI analysis consists also in this case of around 700 thousand elements.

(a)

scale factor	elements	mean WSS (Pa)	E mean (%)
1.3	397594	0.3593404	6.103549895
1.2	476825	0.3596285	6.028268721
1.1	582752	0.3608595	5.706605668
1	722277	0.3718808	2.826715332
0.9	925375	0.3692812	3.505996625
0.8	1214688	0.3740454	2.261100511
0.7	1662251	0.379466	0.844685609
0.65	1978455	0.3826986	0

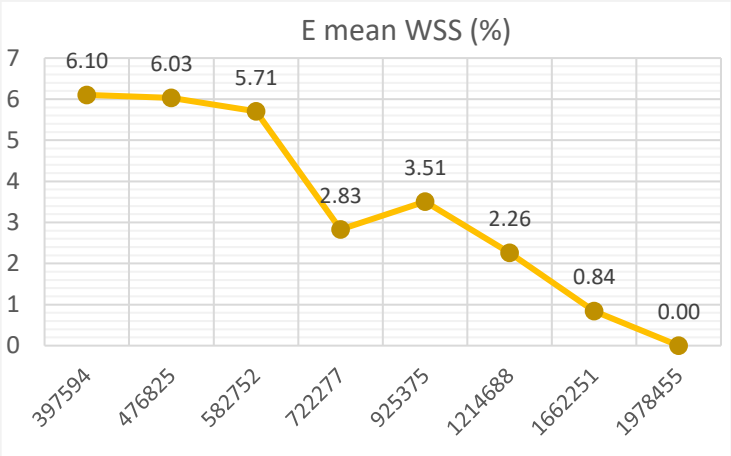

(b)

scale factor	elements	max WSS (Pa)	E max (%)
1.3	397594	5.82242	3.35016422
1.2	476825	7.331274	21.69620676
1.1	582752	6.156664	2.198152066
1	722277	6.570977	9.075581625
0.9	925375	5.990294	0.563523179
0.8	1214688	5.897672	2.101011214
0.7	1662251	6.509813	8.060283767
0.65	1978455	6.024242	0

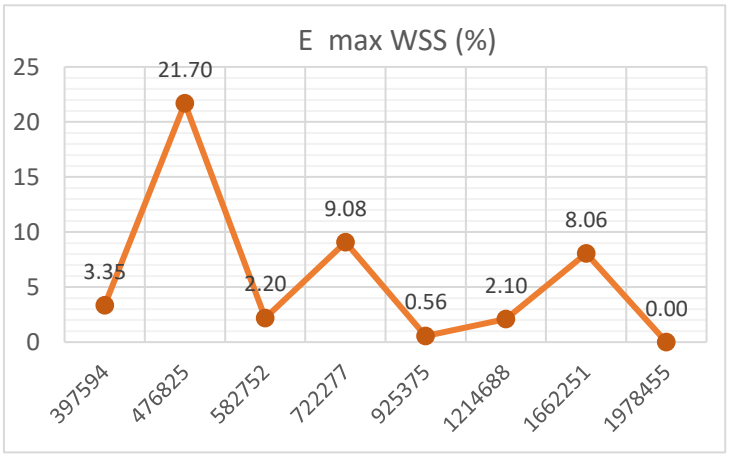

(c)

scale factor	elements	99_perc (Pa)	E 99_perc (%)
1.3	397594	2.543543858	4.916972599
1.2	476825	2.527790533	5.505865067
1.1	582752	2.540767637	5.020753591
1	722277	2.561460394	4.247214764
0.9	925375	2.580879876	3.521273607
0.8	1214688	2.625350383	1.858872386
0.7	1662251	2.662388319	0.474316328
0.65	1978455	2.675076644	0

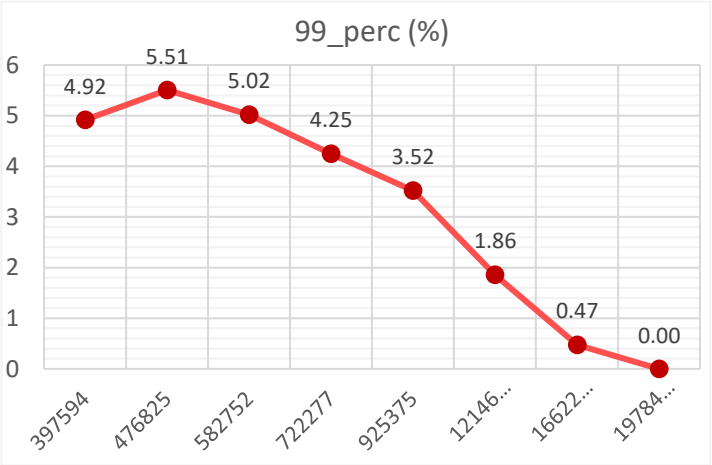

Figure 43 Sensitivity analysis bovine arch configuration. (a) Mean WSS values and associated relative percentage difference (LEFT), mean WSS relative percentage difference as a function of mesh elements (RIGHT). (b) Max WSS values and associated relative percentage difference (LEFT), max WSS relative percentage difference as a function of mesh elements (RIGHT). (c) 99th percentile of the WSS and associated relative percentage difference (LEFT), 99th percentile relative percentage difference as a function of mesh elements (RIGHT).

A top view of the chosen meshes and a cut plane that shows the elements in the domain are reported for both models in Figure 44.

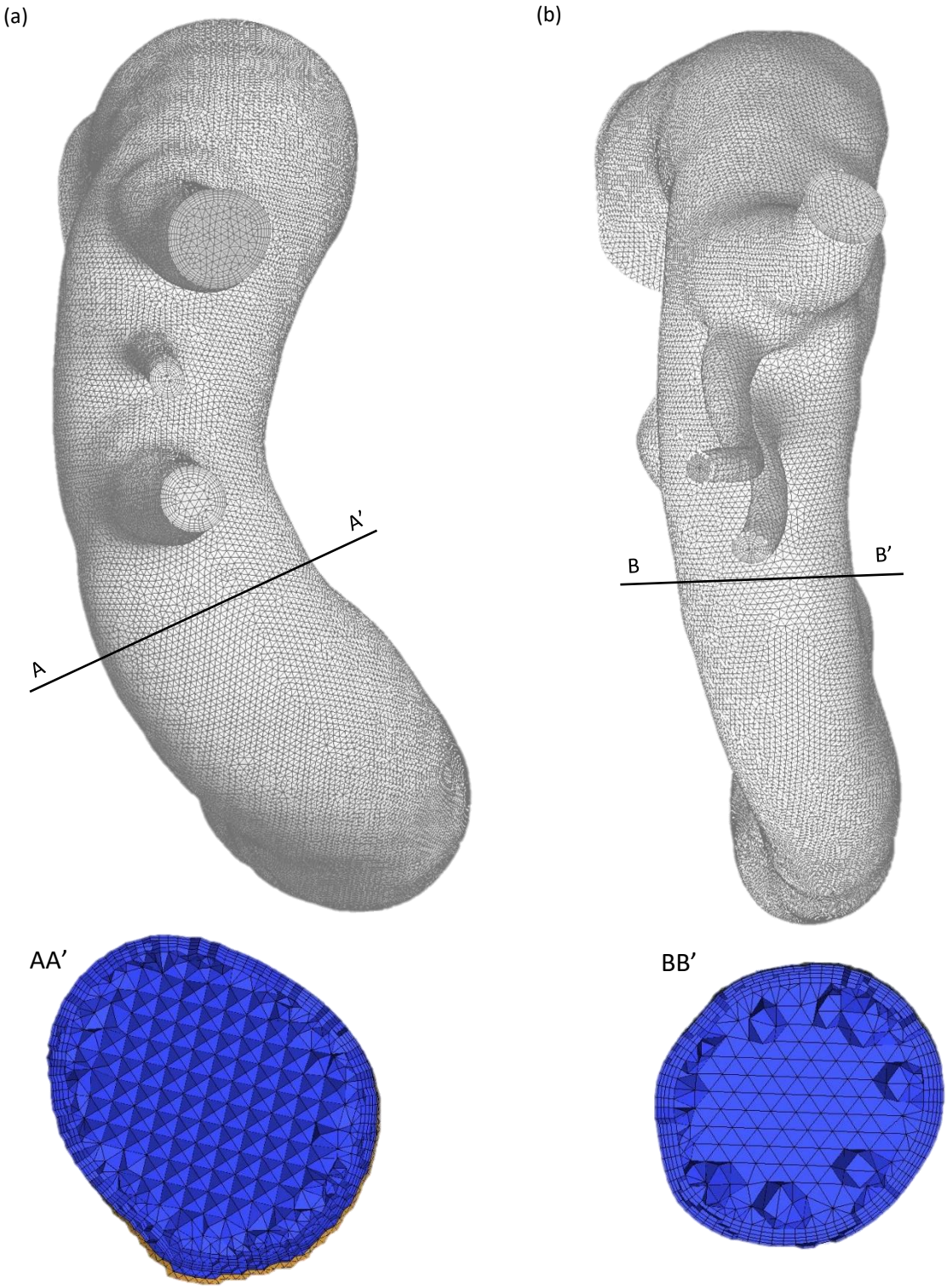

Figure 44 Mesh grids. (a) Top view of the mesh in the standard configuration (TOP) and cut plane AA' through the aortic arch (BOTTOM). (b) Top view of the mesh in the bovine arch configuration (TOP) and cut plane BB' through the aortic arch (BOTTOM).

3.3.2 Solid domain

The structural domain was meshed in Mechanical APDL, the ANSYS Workbench component for the structural analysis. A wall thickness of 2 mm was imposed, which was discretized through a single layer mesh of shell elements. In particular SHELL281 elements were chosen as they are ideal for non-linear applications characterized by large deformations. The element has eight nodes with six degrees of freedom at each node: translations in the x, y, and z axes, and rotations about the x, y, and z-axes. Five integration points have been implemented through the thickness to help the model to converge. The meshes obtained were characterized by approximately 70 thousand and 100 thousand elements for the standard and the bovine arch configuration, respectively. detail at of the mesh at the supra-aortic vessels is reported in Figure 45 for both configurations.

(a)

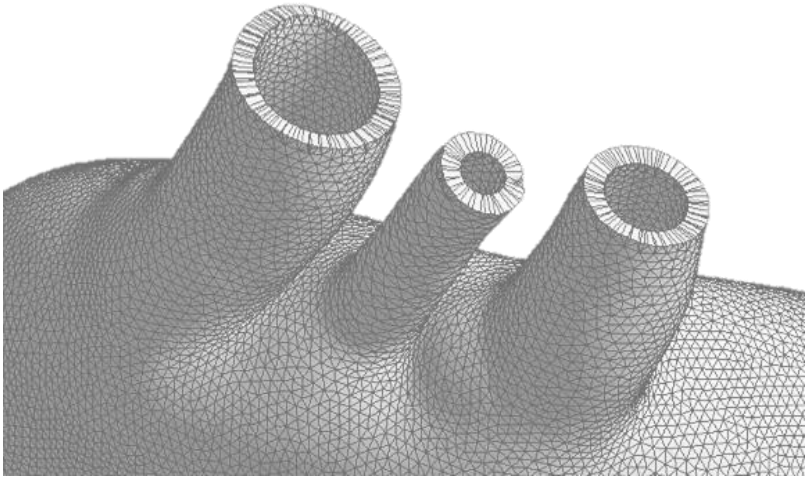

(b)

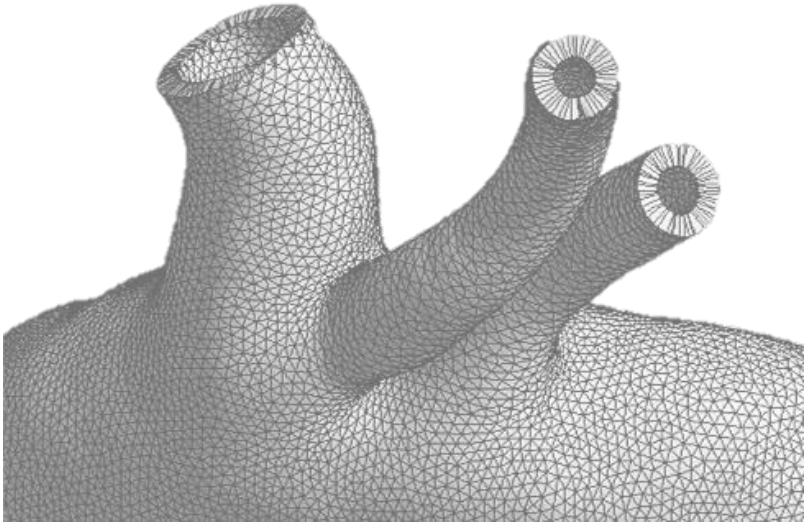

Figure 45 Structural mesh at the supra-aortic vessel in the standard configuration (a) and in the bovine arch configuration (b).

3.4 Fluid model

3.4.1 Blood rheology

Blood is a two-phase suspension of particles, including red blood cells (RBCs), white blood cells and platelets, in an aqueous solution of organic molecules, proteins, and salts called plasma. Blood is a non-Newtonian fluid with a shear-thinning behaviour, which means that its viscosity decreases as the shear rate increases. At low shear rates (<100 s^{-1}) the viscosity is high due to the RBCs that tend to aggregate in stack called rouleaux. Increasing the shear rate values the RBCs disaggregate and deform leading to a decreased viscosity value. Being the viscosity the slope of the shear stress–shear rate relation, the curve in Figure 46 is obtained for shear-tinning fluids.

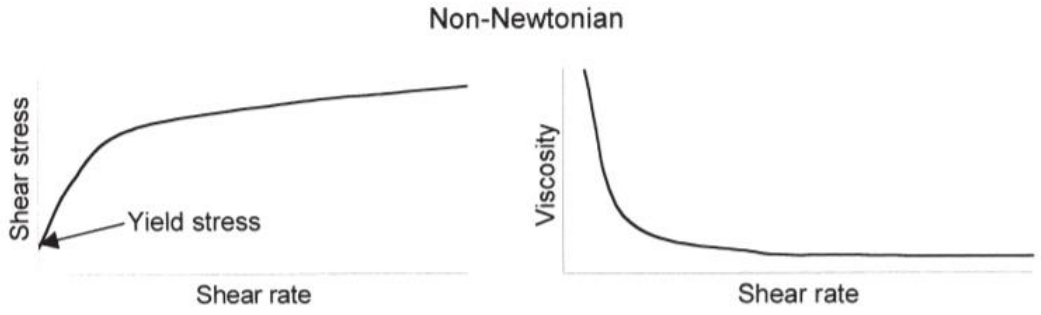

Figure 46 Shear-tinning behaviour of the blood. (a) Shear stress - Shear rate relationship. (b) Viscosity - Shear rate relationship. [94]

In this study, it was chosen to model the blood as a Newtonian fluid. This assumption is made considering that the shear rates in the aorta are elevated and the rouleaux formation is strongly unlikely under pulsatile flow conditions [75]. Some investigation has shown that this hypothesis is reasonable, as it leads to minor differences in the results obtained [76]. For this thesis, a constant viscosity of 0.00319 Pa*s was assumed, which represent a typical value at normal hematocrit level (45%).

The blood density can be calculated as the average between the density of plasma (1035 kg/m3) and the density of the RBCs (approximately 1090 kg/m^3 for a 45% hematocrit). A constant density of 1060 kg/m^3 was assumed for this study. The blood flow was assumed to be laminar, which is a commonly accepted simplification for large vessels where the average velocity results in relatively low Reynolds numbers.

3.4.2 Boundary conditions

The boundary conditions curves used for this study were obtained from the model developed by Computational Life, Delaware. The blood pressure, flow rate and velocity were computed for healthy, hypotension and hypertension conditions and saved at the inlet/outlet interfaces of the arteries connected with the ascending and descending aorta (vessels 1, 3, 11, 12 and 15 in Figure 47). The geometrical characterization of these vessels and of the aortic arch (vessel 2 and 10 in Figure 47) is reported in Table 5.

Artery (Nr, Name)	**Radius [cm]**	**Length [cm]**
1, Ascending Aorta	1.4725	2
2, Aortic Arch (1st section)	1.381	3
3, Brachiocephalic artery	0.635	3.5
10, Aortic Arch (2nd section)	1.294	4
11, Left Carotid artery	0.385	20.8
12, Descending Aorta (1st section)	1.185	5.5
15, Left Subclavian artery	0.416	3.5

Table 5 geometric characterization of the vessel of interest in the Computation Life model.

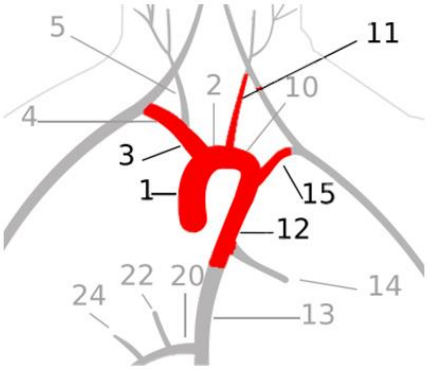

Figure 47 1D model of the aorta [50].

Given the data obtained from the 1D computational model, a flat time-varying velocity profile was imposed at the inlet, and a pressure profile was applied for each outlet. All the data were normalized to a time interval of 1 s. A User-Defined Function (UDF) was implemented in Fluent, in which the profiles were modelled through the Fourier series:

$$f(t) = \frac{a_O}{2} + \sum_{n=1}^{N} [a_n \cos(nt) + b_n \sin(nt)] \qquad \textbf{(3.6)}$$

where a_O, a_n and b_n are Fourier coefficient that should be tuned to correctly approximate the function $f(t)$, and N is the number of coefficients. As a higher number of coefficients correspond to a greater accuracy in the approximation of the curve of interest, 100 coefficients were used for each BC curve.

Preliminary CFD simulations were run in order to both check if the model correctly resembled the aortic behaviour in physiological or pathological conditions, and to obtain a result file that could be used for the initialization of the FSI simulation. Some issues arose in this phase because of the boundary conditions. Looking at the flow rate through the outlet surface of the supra-aortic vessels, it was observed reversed flow throughout the diastolic phase of the cardiac cycle (Figure 48, obtained for a healthy patient). No convergence problem was encountered, but the physiology of the vessel was not correctly reproduced. Also, the shape of the flow rate curves present a shape slightly different from the expected one, especially for the carotid and the subclavian vessels where a shorter systolic peak and a larger backflow phase are observed. Anyway, these irregularities have been considerate as acceptable.

(a)

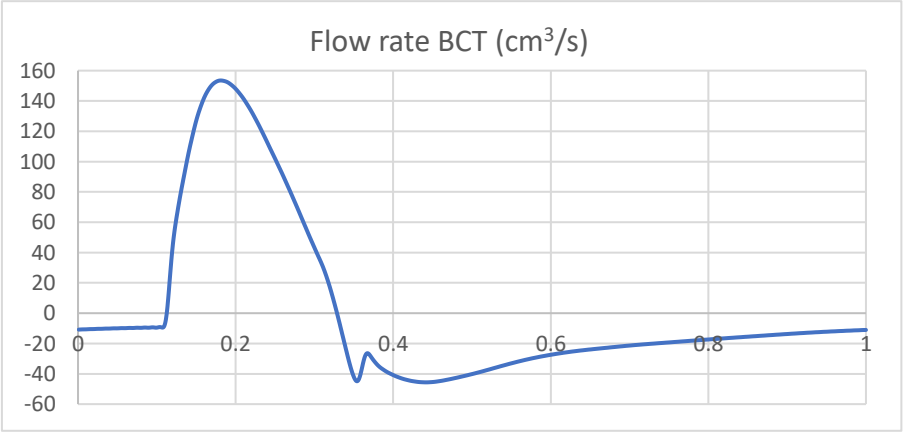

(b)

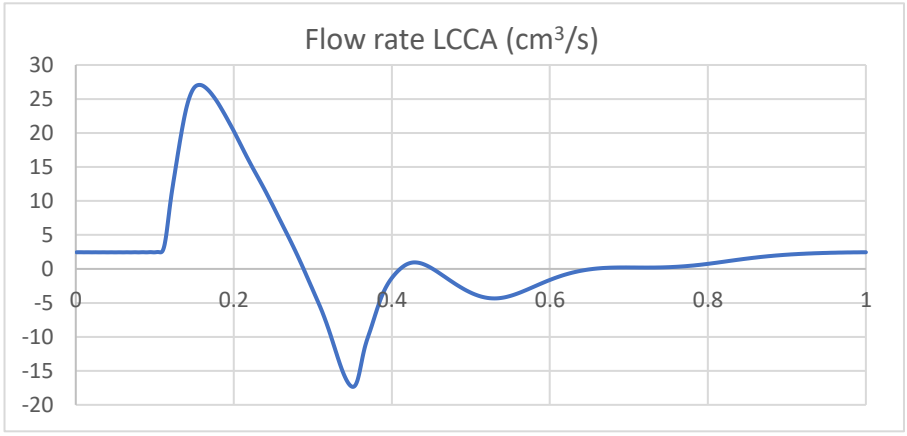

(c)

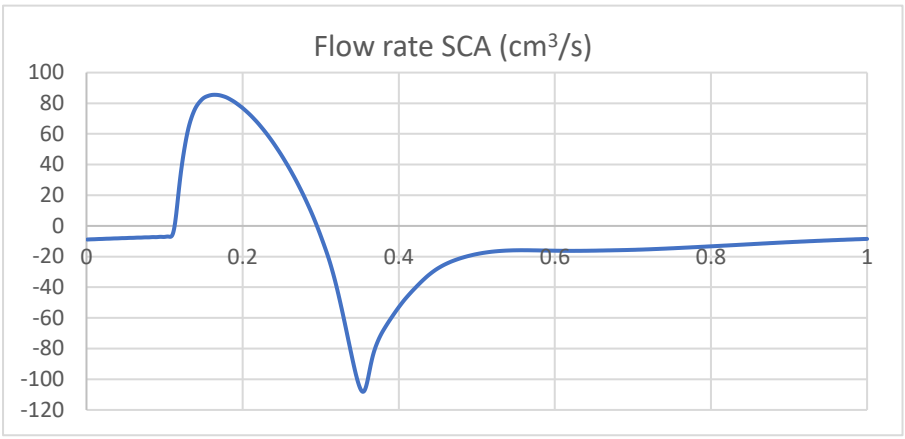

Figure 48 Flow rate of the supra-aortic vessels obtained through CFD calculation. (a) Flow rate LCCA. (b) Flow rate BCT. (c) Flow rate SCA.

It is supposed that the problem is given by the differences existing between the 1D model and the FSI settings, such as the fact that the aorta modelized by the Computational life software is connected to a close loop which takes into account the resistance of the vessels downstream, or the difference in the elasticity of the vessel within the two models. Some minor modification of the pressure curves of the supra-aortic vessel were made in order to solve this problem, paying attention to not change the condition that had to be tested. The systolic pressure was decreased by 2/3 mmHg in order to increase the ΔP with the inlet pressure, ensuring a higher driving force towards these vessels. These adjustments have been made for all the three sets of boundary conditions. The final curves used in the simulations for each patient are reported in the figures below (Figure 49, Figure 50).

(a)

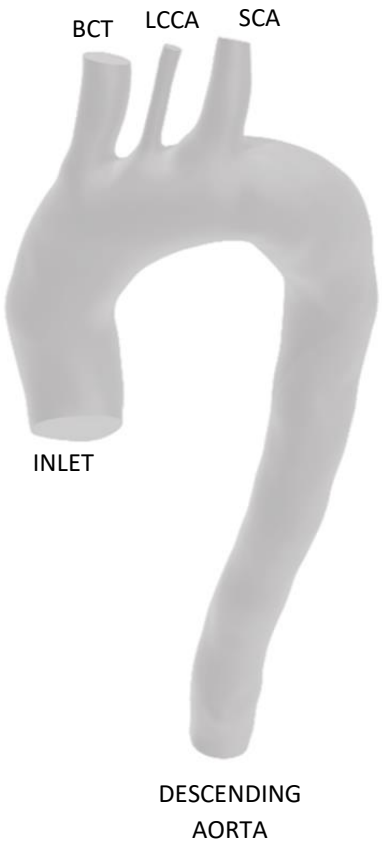

(b)

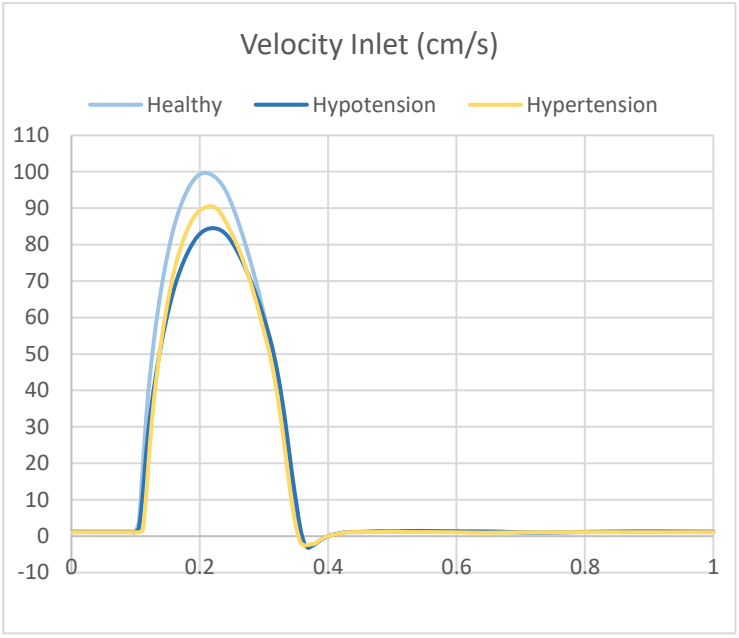

(c)

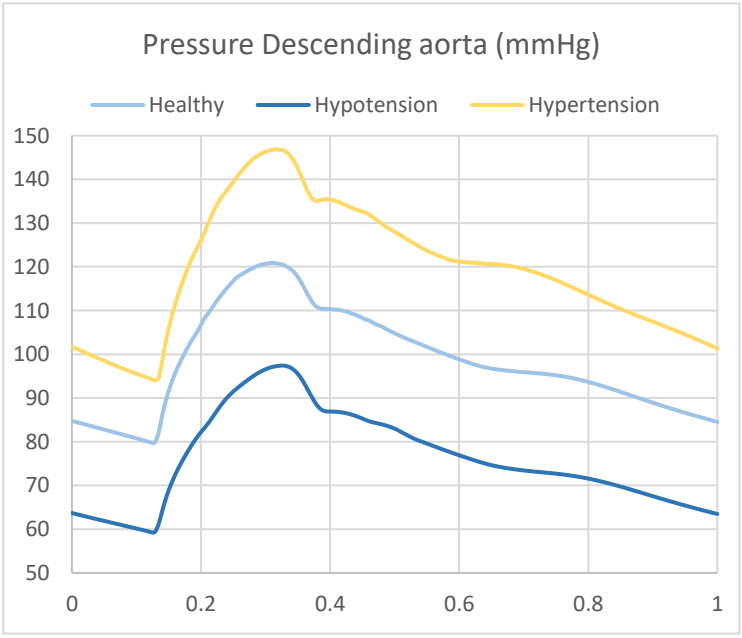

Figure 49 Boundary conditions applied for the healthy, hypertensive and hypotensive cases. (a) Geometrical reference of the boundaries in the model. (b) Velocity curves applied at the inlet. (c) Pressure curves applied at the descending aorta.

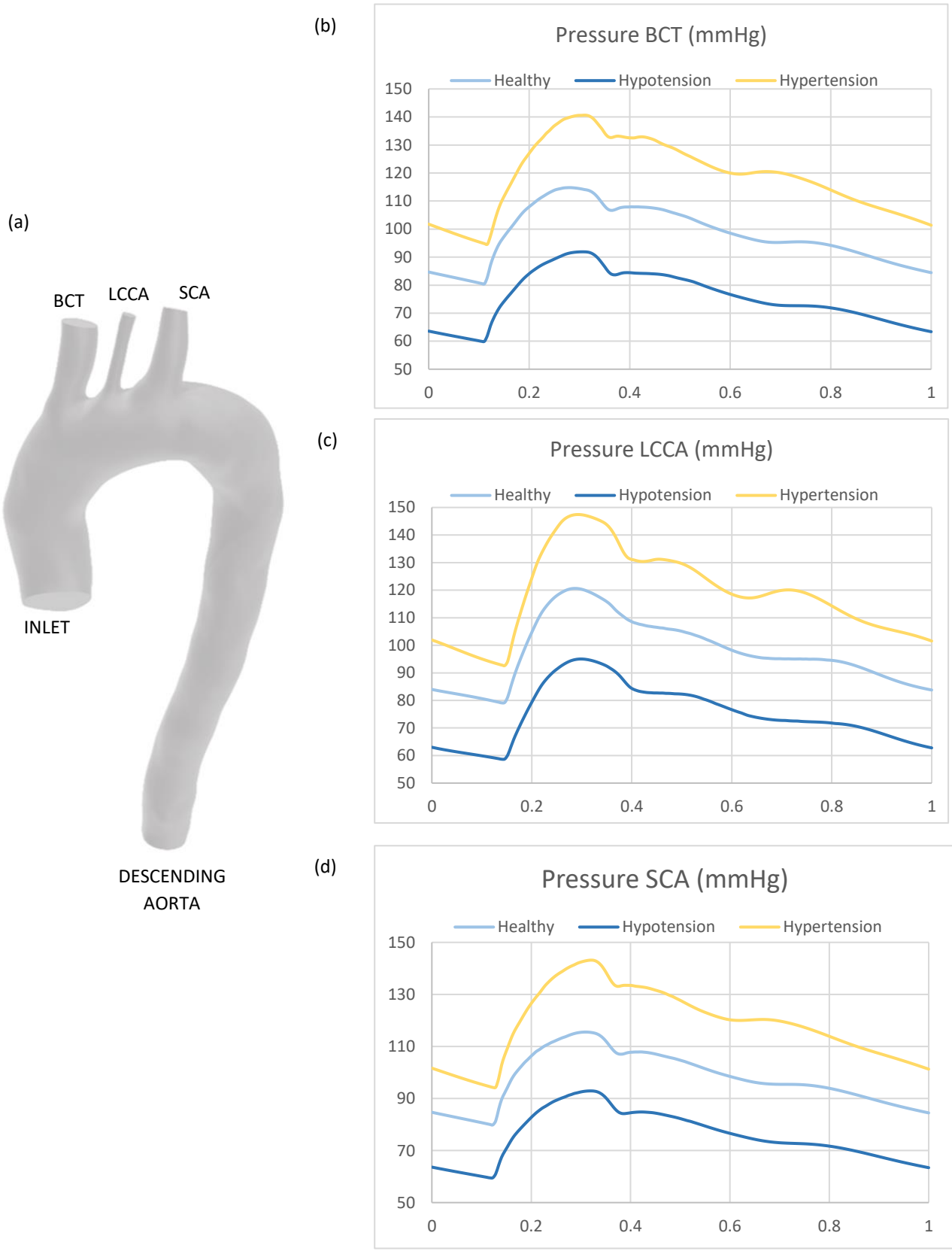

Figure 50 Boundary conditions applied for the healthy, hypertensive and hypotensive cases. (a) Geometrical reference of the boundaries in the model. (b) Pressure curve applied to BCT. (c) Pressure curve applied to LCCA. (d) Pressure curve applied to SCA.

3.4.3 Numerical settings - Fluent

ANSYS Fluent solver relies on the finite volume method for the numerical implementation of the fluid dynamic problems. This approach first approximates the transport equations with their integral form on the mesh volumes in which the computational domain is divided, then by means of Gauss's divergence theorem, converts the volume integrals into surface integrals over the bounding surface that defines each control volume, and finally transform the equations in a system of algebraic equations through different discretization schemes. The equations are solved iteratively for each volume and the results are stored at the cell centre.

Discretization schemes can be set manually under the *method* section of the Fluent Software. As face values of field variables are needed to solve the discretized form of surface integrals for the convection and diffusion terms, spatial discretization schemes are employed to interpolate face values from cell centre values. For the current work, the following spatial discretization schemes were chosen:

- A Least Square Cell Based scheme for the diffusive term. It is based on the assumption of linear variation of the variable of interest between cell centres (linear interpolation), and can be expressed as

$$(\nabla\varphi)_{C_0} \cdot \Delta r_i = \left(\varphi_{Ci} - \varphi_{C_0}\right) \qquad \textbf{(3.7)}$$

  where φ is the quantity of interest, c_0 and c_i are the centroid of two cells and Δr_i is the distance between the centroid of the two cells.

- A first-order Upwind scheme for the convective term. This scheme approximate the face value to be equal to the cell-centre value located upstream according to the flow direction. It is defined as

$$\varphi_{face} = \begin{cases} \varphi_{c_0} & if \quad \boldsymbol{v} * \boldsymbol{n} > 0 \\ \varphi_{c_i} & if \quad \boldsymbol{v} * \boldsymbol{n} < 0 \end{cases} \qquad \textbf{(3.8)}$$

  where $\boldsymbol{v}$ is the fluid velocity vector and $\boldsymbol{n}$ is the face normal.

- A linear scheme for the pressure, which assume the face value as the weighted average of the cell-centre value of the adjacent cells. It is based on the following equations:

$$\varphi_{face} = \lambda_{face}\varphi_{C_0} + \left(1 - \lambda_{face}\right)\varphi_{C_i} \quad \textbf{(3.9)}$$

$$\lambda_{face} = \frac{\Delta r_{face}}{\Delta r_i} \quad \textbf{(3.10)}$$

where Δr_{face} is the distance between the face and the centroid c_0.

Because this study is based on time dependent simulation, a time discretization scheme is also needed. The time domain T is subdivided in a finite number n of time steps Δt at which the approximate solution is obtained. For this study a second order implicit scheme was implemented, which can be described as

$$\frac{3\varphi^{n+1} - 4\varphi^{n} + \varphi^{n-1}}{2\Delta t} = f(t^{n+1}, \varphi^{n+1}) \quad \textbf{(3.11)}$$

The function $f(t^{n+1}, u^{n+1})$ represents all the terms related to the spatial discretization. The solution of this equation is obtained iteratively so this method is absolutely stable, but computationally expensive. The choice of the appropriate time step was made by means of the Courant–Friedrichs–Lewy condition which is reported here:

$$C = \frac{\boldsymbol{v} \cdot \Delta t}{\Delta x} < C\text{max} \quad \textbf{(3.12)}$$

where $\boldsymbol{v}$ is the fluid velocity vector, Δx is the average dimension of the mesh elements, C is the Courant number and Cmax is the maximum acceptable Courant number to not have numerical instability. By imposing Cmax equal to 1[77], an optimal time step of 0.001 was obtained for both geometries. This value will be imposed in the system coupling solver and will be valid also for Mechanical APDL.

Furthermore to guarantee the pressure-velocity coupling a coupling scheme should be set. A SIMPLE (Semi-Implicit Method for Pressure-Linked Equations) algorithm was chosen, which is a staggered algorithm, meaning that the momentum and the pressure correction equations are solved sequentially. For each iteration, the algorithm updates the velocity value and the pressure

value adding a correction term; the results obtained are then used to solve the continuity equation on which the convergence is checked. If the convergence is reached the system moves to the next time step otherwise it starts another iteration. In the simulations performed, a convergence threshold of 10^{-3} on the residual error was established. The update of velocity and pressure at each iteration can be modulated multiplying the correction terms by the under-relaxation factors (URF). These parameters highly affect convergence and computing time but they do not alter the accuracy. A correct choice of these factors is essential; indeed values of the URF that are too large may lead to oscillatory or even divergent iterative solutions, while value that are too small will cause extremely slow convergence. For this research URF of 0.7 and 0.3 were set respectively for pressure and momentum.

In order to allow the deformation of the fluid mesh according to the structural domain motion, a dynamic mesh was enabled at the fluid-solid interface, selecting both the smoothing and the remeshing methods. The smoothing method absorbs the motion of the deforming wall by moving the interior nodes, without changing the number of nodes and their connectivity. A diffusion smoothing was applied with a diffusion parameter equal to 2. Diffusion smoothing is the most indicated for large deformations, due to the fact that it generates higher quality meshes. The remeshing method, instead, creates a new mesh with a different number of nodes and a different connectivity between them. The remeshing method is activated when the size or the quality of the element exceed specific limit, in order to avoid convergence problems and negative volume issues. The limits imposed were of 0,5 and 2,5 mm as minimum and maximum dimension of the element, and 0.8 as maximum acceptable skewness.

3.5 Structural model

3.5.1 Constitutive model aorta

The complex multi-layered structure of the aortic wall, together with the histological composition of each tunica, are responsible for the anisotropic hyperelastic behaviour typical of the aortic vessel. By anisotropy it is meant that the material response changes according to the direction on which the load is applied. This is observed when the material is not homogeneous, presenting fibres or components oriented in space, like the collagen fibres

observed through the thickness of the aortic wall. For the aortic wall material, hyperelasticity describes a load-stiffening behaviour at high strains, according to which higher stress level should be imposed to generate further deformation. This is caused by the progressive recruitment of the collagen fibres with increasing of the load imposed. The aortic wall material is also considered to be incompressible, with a density equal to 1120 kg/m^3. The wall properties can change significantly between different subjects, as they depends on multiple factors such as age and pathological conditions that alter the hemodynamic. It is then difficult to choose a constitutive model that replicate accurately all the vessel properties, and usually the same assumptions are made.

For this investigation, an incompressible, isotropic, hyperelastic constitutive model was implemented. The isotropic assumption was demonstrated to guarantee a good approximation of the hemodynamic patterns in a large vessel [78]. A Yeoh constitutive model was chosen, which is characterized by the following strain energy function:

$$\psi = C_{10}(I_1 - 3) + C_{20}(I_1 - 3)^2 \qquad \textbf{(3.13)}$$

were I_1 is the first invariant of the Cauchy-Green strain tensor, $C_{10} = 1.39\ MPa$ and $C_{20} = 0.5\ MPa$ are material parameters [79]. The stress-strain relationship obtained for the chosen parameters is reported in Figure 51.

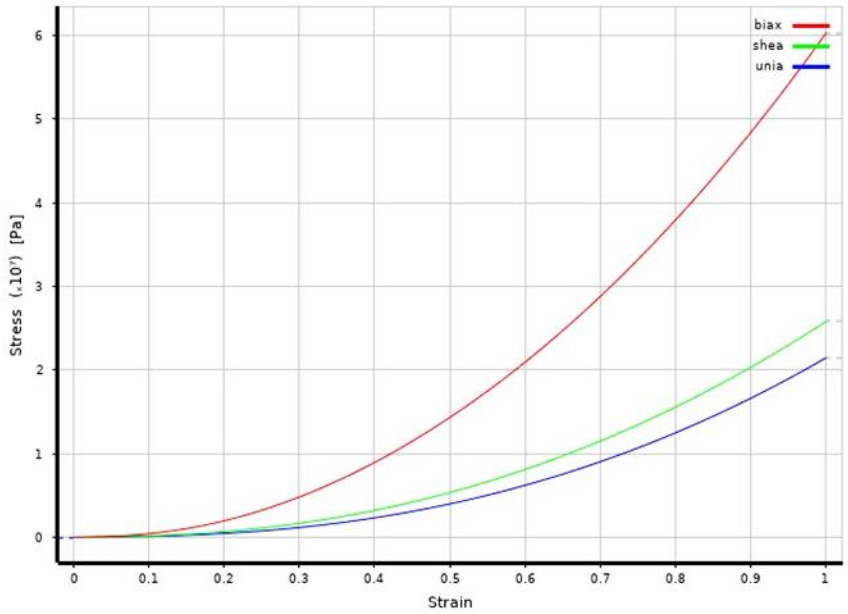

Figure 51 Stress-strain relationship for the material modelled.

3.5.2 Numerical setting - Mechanical APDL

Mechanical APDL relies on a displacement-based Finite Element method (FEM) for the approximation of the governing equation. After obtaining the integral form of the equation, the displacement field is discretized on the nodes through the use of shape functions and the stresses and strains are rewritten as a function of the nodal displacement. The final form of the discretized equation can be summarized as

$$\boldsymbol{M\ddot{u} + Ku = f} \tag{3.14}$$

where **M** and **K** are respectively the mass and stiffness matrix, **f** is the load vector and $\boldsymbol{\ddot{u}}$ and $\boldsymbol{u}$ are the nodal acceleration and displacement respectively.

A viscous matrix $\boldsymbol{\zeta}$ can be introduced in this formulation to account for the viscoelasticity of the aortic wall. This matrix add a Rayleigh numerical damping to the system and is calculated as a linear combination of the stiffness and the mass matrix according to the following formula:

$$\boldsymbol{\zeta} = \alpha \boldsymbol{M} + \beta \boldsymbol{K} \tag{3.15}$$

where $\alpha = 5650$ and $\beta = 0.1$ are Rayleigh numerical coefficient [80].
Thus, the equation that is solved by ANSYS Mechanical becomes:

$$\boldsymbol{M\ddot{u} + \zeta\dot{u} + Ku = f} \tag{3.16}$$

where $\boldsymbol{\dot{u}}$ is the nodal velocity.

Aside the Rayleigh coefficient, no specific analysis parameter was imposed and the default option Programme Controlled was maintained. Two sub-steps for each time iteration were imposed, as a $\Delta t = 0.001\ s$ was not sufficient to guarantee the convergence of the structural domain. Other than that, the necessary BC have been set. A fixed support was adopted at the inlet and the outlets, a fluid solid interface was defined on the surface to allow the interaction with the fluid domain and a pressure of 52 mmHg was applied to the exterior surface to account for the constrain imposed by the surrounding tissues.

3.6 System Coupling

The system coupling component guarantees the interaction between ANSYS Fluent and Mechanical APDL, by transferring the obtained data from one solver to the other at each coupling iteration. In particular, the data transferred from the fluid domain to the structural one is the force imposed by the blood motion on the fluid-solid interface, calculated as the integral form of the pressure over the surface area. The incremental displacement registered at the wall is then transferred back to the fluid domain, where eventually the remeshing process takes place. A convergence criterion is imposed on the data transferred, through a maximum root-mean-square (RMS) residual which measures the variation of the data transfer between two following iterations. An RMS equal to 0.01 was chosen for both data transfers.

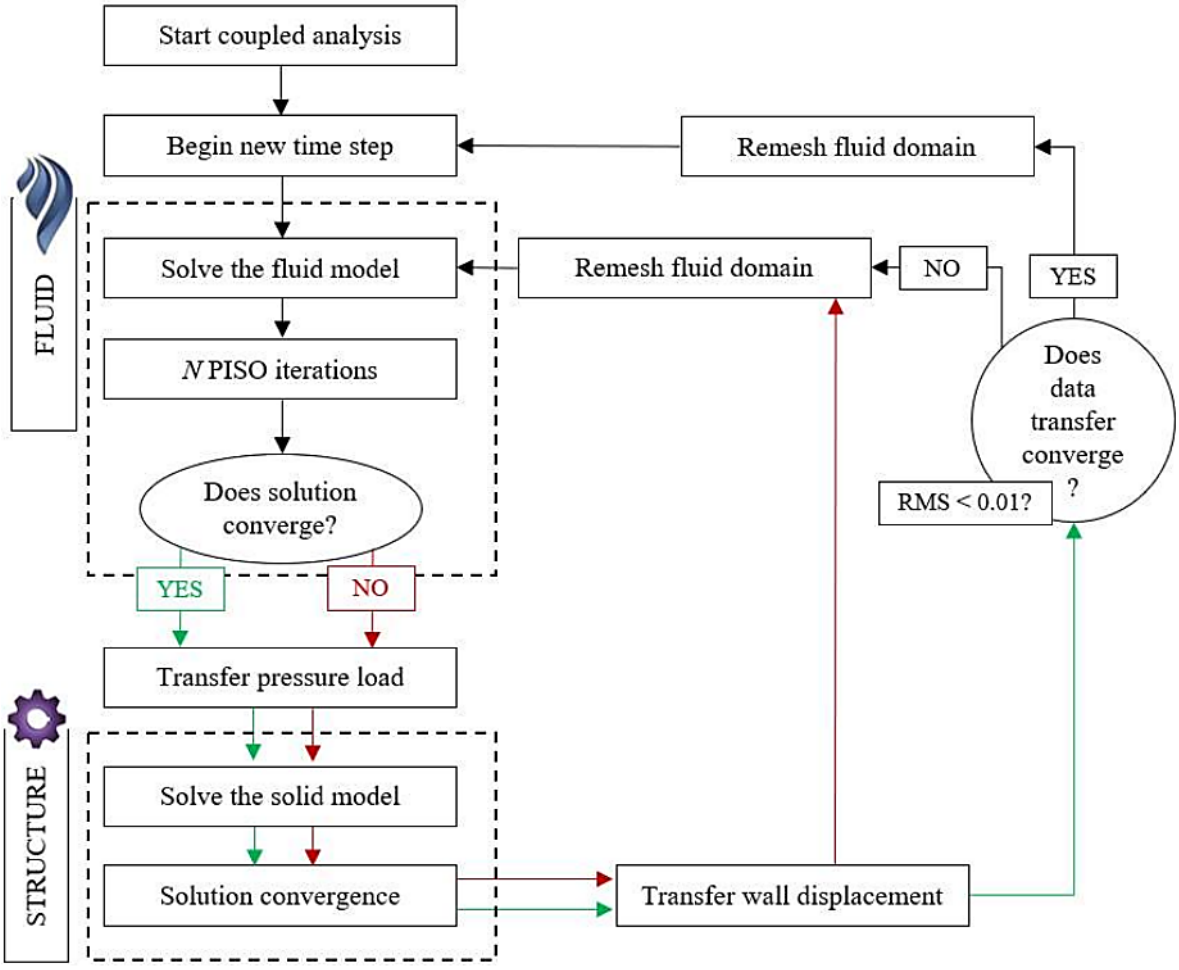

Figure 52 Schematic representation of the coupling solving process [90].

Coupling iterations were repeated till the convergence threshold was reached or the maximum number of iterations imposed for each time step was reached (the default number of 5 iterations was maintained). Also, an URF of 0.3 was set for the transfer of the pressure load from the fluid domain to the structural one to help the convergence of the system. Two complete cardiac cycles were run by imposing an end time of 2 s. As anticipated in Section 3.3.3 a time step of 0.001 was imposed, so a total of 2000 iterations were run. A schematic representation of the coupled simulation solving process is reported in Figure 52.

3.7 WSS-based descriptors

Given the strict correlation between WSS and aortic wall pathologies, there is an increased interest towards this hemodynamic quantity within the biomechanics literature. Various WSS-based descriptors have been introduced in order to ease the interpretation of complex four-dimensional WSS data. The WSS descriptors integrate the WSS data over time, allowing an overall understanding of the interaction between hemodynamic patterns and aortic wall throughout a whole cardiac cycle. In this study, the Time-Averaged Wall Shear Stresses (TAWSS), the Oscillatory Shear Index (OSI) and the Relative Residence Time (RRT) were calculated and analysed.

The TAWSS expresses the total amount of shear-stress experienced by a vessel wall throughout the entire cardiac cycle. Low TAWSS (<0.4 Pa) have been demonstrated to be associated to abnormal flow patterns promoting atherogenic pathologies and wall thickening [81, 82]. Elevated TAWSS, instead, can potentially cause the haemolysis of RBC and damage the endothelium, leading to the initiation and the progression of intimal tearing [83]. TAWSS is defined by the following equation:

$$TAWSS = \frac{1}{T} \cdot \int_0^T |WSS(s,t)|\, dt \qquad \textbf{(3.17)}$$

where T is the duration of the cardiac cycle and $WSS(s,t)$ is the magnitude of the WSS vector at a specific location and time.

The OSI estimates the deviation of the WSS vector from the principal flow direction over a cardiac cycle. OSI values, which range between 0 and 0.5, are calculated through the formula below:

$$OSI = \frac{1}{2} \cdot \left[1 - \left(\frac{\left| \int_0^T WSS(s,t) dt \right|}{\int_0^T |WSS(s,t)| \, dt} \right) \right] \quad \textbf{(3.18)}$$

Areas characterized by elevated OSI values are associate to highly oscillating WSS vectors over the cardiac cycle, which can lead to flow disruption and separations at the bifurcation level. Oscillating pattern together with low magnitude of WSS can lead to atherosclerotic plaque and hyperplasia [84, 85].

Finally the RRT combine the previous indices to estimate the residence time of the particles at the wall. It is described as

$$RRT = \frac{1}{(1 - 2 \cdot OSI) \cdot TAWSS} = \frac{1}{\left| \int_0^T WSS(s,t) dt \right|} \quad \textbf{(3.19)}$$

4 Results

In this chapter the results obtained from numerical simulations will be presented. Flow patterns, WSS-based descriptors and structural results are reported, comparing the BCs and the aortic arch configurations.

4.1 Introduction

The results reported in this section are divided in three main sections. The first one focuses on the analysis of the comparison of the flow rates obtained at the outlets for the different boundary conditions. the second one is a comparison between the hemodynamics and the structural results obtained for the different pressure levels, first studying the standard configuration and then the bovine arch. Finally, the third section reports a comparison of the results obtained for the two configurations to assess the effect of the aortic arch configuration on the results obtained.

All the data were taken from the second cardiac cycle. The simulation run times for two cardiac cycle were around 5 to 7 days depending on the simulation. Many factors influenced the run time: two different computers were used and some simulations were run simultaneously causing the simulation to slow each other down a bit.

4.2 Flow rate curves

The modelling of the BCs through the use of the Computational Life model is an important focus of this work thesis. The possibility to compute curves specific for the conditions and the pathologies of interest is a powerful tool, which allows obtaining similar conditions to the ones experienced by the patient by simply tuning some parameters. The gold standard at the moment is the use of patient-specific boundary conditions, or the imposition of a flow division between the descending aorta and the supra-aortic vessel based on the literature. The patient-specific boundary conditions guarantee the greatest adherence to reality possible but it can be difficult to obtain and process these data; on the other hand the flow division is very easy to model but represents a strong simplification of the system. The curves obtained by the Computational Life model can be a good compromise to reproduce accurately the cardiovascular system without complicating excessively the process to obtain these boundary conditions. In this paragraph the flow rate curves at the outlets are analysed, in order to evaluate the results obtained for this approach and to assess the differences generated by the different pressure conditions.

Figure 53 and Figure 54 report respectively the flow rate curves for the healthy and for the bovine configuration. Each graph reports the results associated to a specific outlet for the three sets of BCs. The curves reproduce faithfully the pattern typical of the cardiac cycle, characterized by a sharp positive peak at systole followed by a negative peak in the backflow phase and then by an almost flat profile in diastole. However, some discrepancy can be identified, such as the depth of the negative peak for the SCA and the LCCA, which is almost as high and as large as the systolic one.

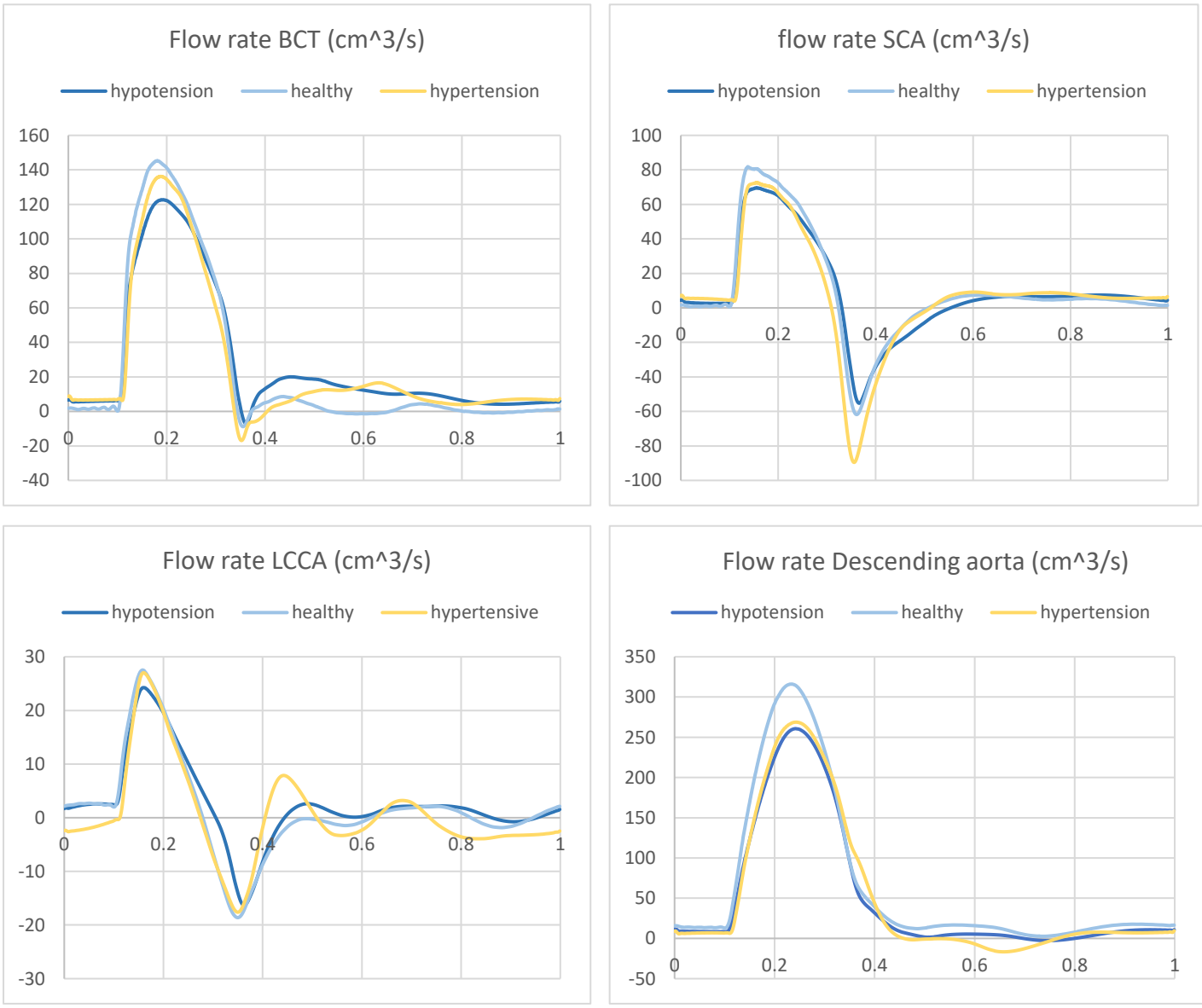

Figure 53 Flow rate plots for the standard configuration for the three sets of boundary conditions.

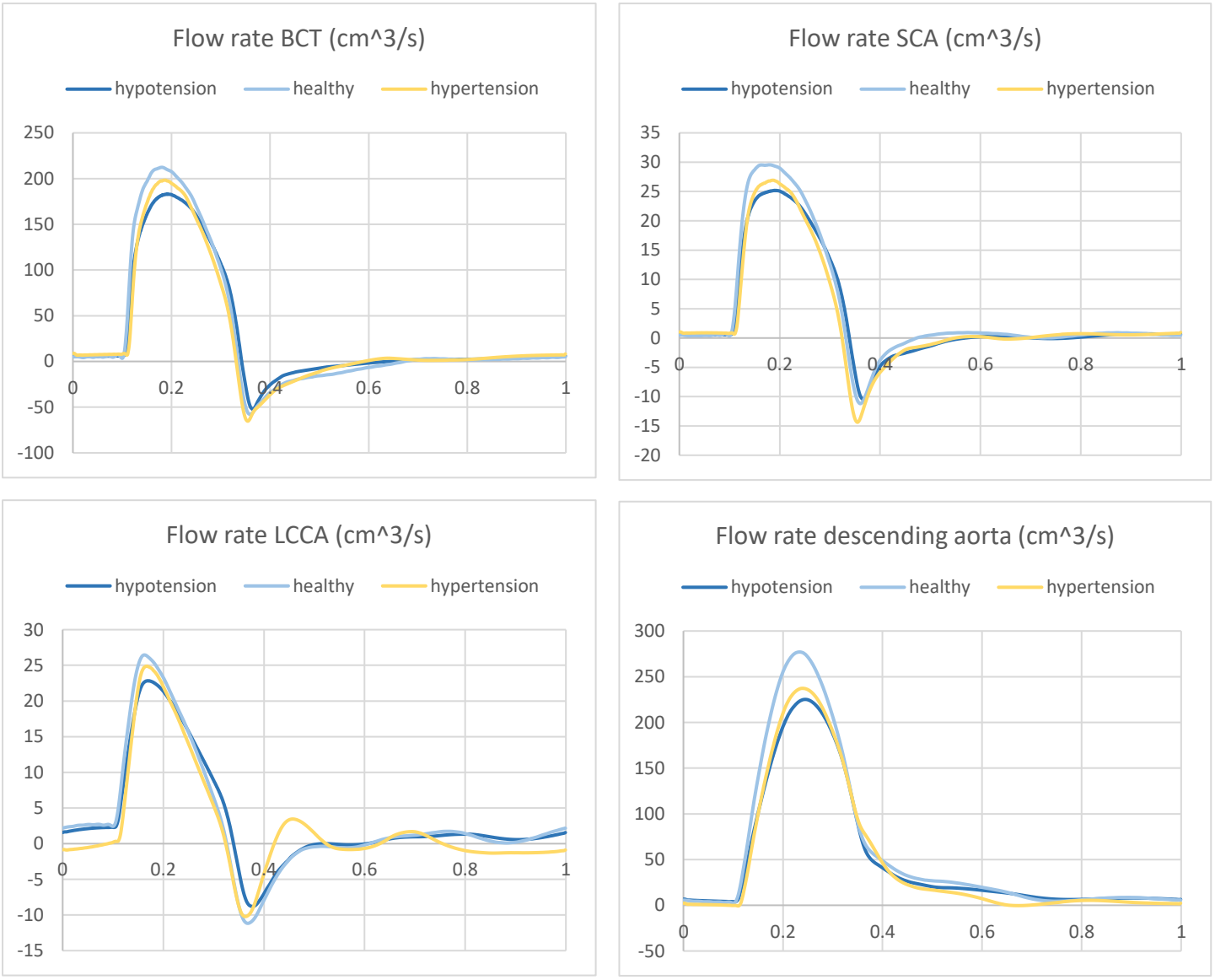

Figure 54 Flow rate plots for the bovine configuration for the three sets of boundary conditions.

Looking at the differences within boundary conditions, it can be noticed that for both configurations the hypertensive condition shows higher oscillatory patterns, especially at the LCCA. The patterns are in most cases very similar in the diastolic phase with the exception of the LCCA and, in the standard configuration, for the BCT. Focusing on the systolic peak, a decrease of 10-18% is measured for the hypotension curve with respect to the healthy one depending on the outlet considered for both configurations; for the hypertensive condition, instead, the decrement observed varies between approximately 4% and 17 % depending on the vessel analysed. The hypertension case is characterized by a higher variability, which brings

the curves to be sometimes more similar to the hypotension ones and other times to be closer to the healthy ones. Also, the hypertension case presents a deeper negative peak for the SCA and the BCT, with respect to the other pressure levels. Looking at these results, it may seem surprising that the hypertension curve is lower than the healthy one, however the development of flow in the ascending aorta depends strongly on the afterload (or the resistance present in the systemic circulation), which is higher in the hypertensive case. This is confirmed by the velocity curves imposed at the inlet that show a greater value for the healthy case and a lower one for the hypotension and the hypertension ones (the decrement is respectively of 15% and 10%) (Figure 55). Also the pressure difference between the inlet and outlet for the three set of boundary conditions was calculated and reported in Table 6: the results confirm the observations above with higher pressure difference in the hypertensive case.

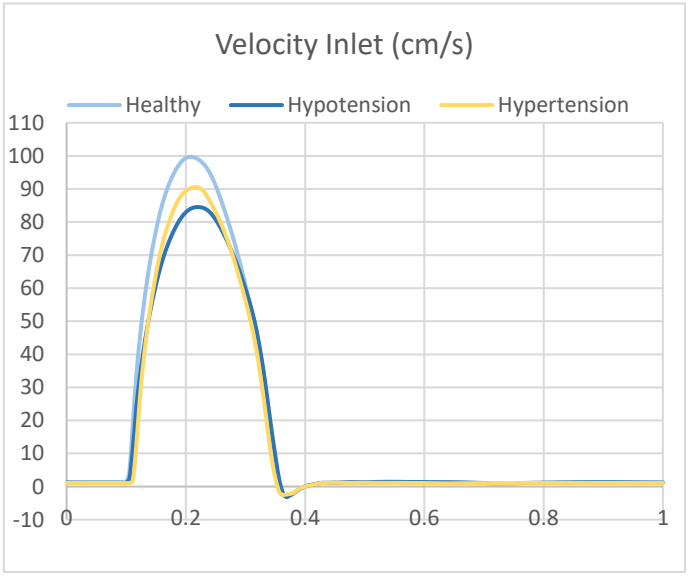

Figure 55 Inlet boundary condition.

Boundary	**Hypotension**		**Healthy**		**Hypertension**	
	P (mmHg)	ΔP (mmHg)	P (mmHg)	ΔP (mmHg)	P (mmHg)	ΔP (mmHg)
Inlet	113.11		88.97		133.16	
BCT	108.05	5.06	84.21	4.76	127.25	5.91
LCCA	105.13	7.98	79.70	9.27	124.91	8.25
SCA	106.49	6.62	82.88	6.09	126.74	6.42

Table 6 Pressure difference between the outlets and the inlet pressures.

4.3 Comparison results for different BCs

4.3.1 Standard configuration

4.3.1.1 Flow patterns

A representation of the flow patterns in the 3D domain was completed for the three sets of BCs at three different time steps: the systolic peak (t=0.2 s), the diastolic peak (t=0.4s) and the end of the diastole (t=0.1 s). For the purpose of comparison all the results at the same time step were rescaled to the same velocity range before reporting them in Figure 56. Also, the results have been plotted on various planes chosen through the vessel in strategic positions: PLANE 1 and PLANE 2 in the ascending aorta (Figure 57, a), PLANE 3, PLANE 4 and PLANE 5 at the proximal descending aorta (Figure 57, b). The data plotted on these planes follow the velocity range reported for the total domain at the corresponding time step.

At the systolic peak (t=0.2 s), no significant differences were observed in the flow patterns between the three cases: an organized flow with parallel streamlines is observed through the domain and no vortexes are generated in correspondence of high curvature and bifurcation. The maximum values are seen at the supra-aortic vessel, particularly at the LCCA that presents the higher section reduction. A contour map was created at PLANE 1 and PLANE 2 to assess the velocity distribution in the ascending aorta (Figure 58, a). The maximum velocity is registered at the posterior wall, meaning there is no impingement of the flow on the anterior area. Higher velocity values are observed throughout the domain for the normotensive case, consistent with the fact that higher velocity profile is imposed at the inlet. The velocity magnitude directly influences the WSS imposed at the wall.

At the diastolic peak (t=0.4 s), recirculating patterns are observed both in the ascending and in the descending aorta. However, some differences can be identified between the two regions, as in the ascending tract the flow patterns are organized in a left-handed helicoidal pattern (Figure 58,b), while the aortic arch and the descending aorta present complicated patterns that vary according to the BCs (Figure 59). In particular, in correspondence of PLANE 3 each BCs is associated with a different streamlines distribution and a different number of vortices. Low vorticity is observed for the hypertension condition in this area. A particular flow distribution is observed for this case, characterized by an acceleration through the SCA vessel and few flow streamlines at the BCT. This distribution suggests the flow encounters some difficulties in

going through the first supra-aortic vessel and is then forced to converge to the SCA. This may be the result of a combination of factor, including velocity differences and differences in the shape of the pressure curves imposed at outlets.

On PLANE 4, a vortex is present at the inner wall for all the BCs, where the highest velocity value is also registered. The recirculation patterns can be an indicator of areas where ADs are more likely to occur, due to the fact that disturbed flow can cause a change in the shape and distribution of the endothelial cells, favouring changes in the mechano-transduction process that characterize the aortic vessel. However, the high vorticity area should be combined with high WSS values for AD, otherwise it is more likely a sign of the development of an atherosclerotic pathology. For this reason, the vortex registered at the outer wall observed in the healthy case shouldn't be a concern for AD formation. On PLANE 5 secondary flows are identified for all the BCs, characterized by two counter-rotating vortices where fluid moves to the outer wall at the centre of the vessel.

At the end-diastole (t=0.1 s) disturbed flows are predominant in the aortic lumen. In the ascending aorta the helicoidal pattern observed at time 0.4 s is maintained (Figure 58, c), while in the descending aorta no clear recirculation patterns were identified.

The data collected till now suggest that the areas characterized by a higher risk of AD development are the posterior area of the ascending aorta, the SCA entrance area and the proximal descending aorta at the interior wall.

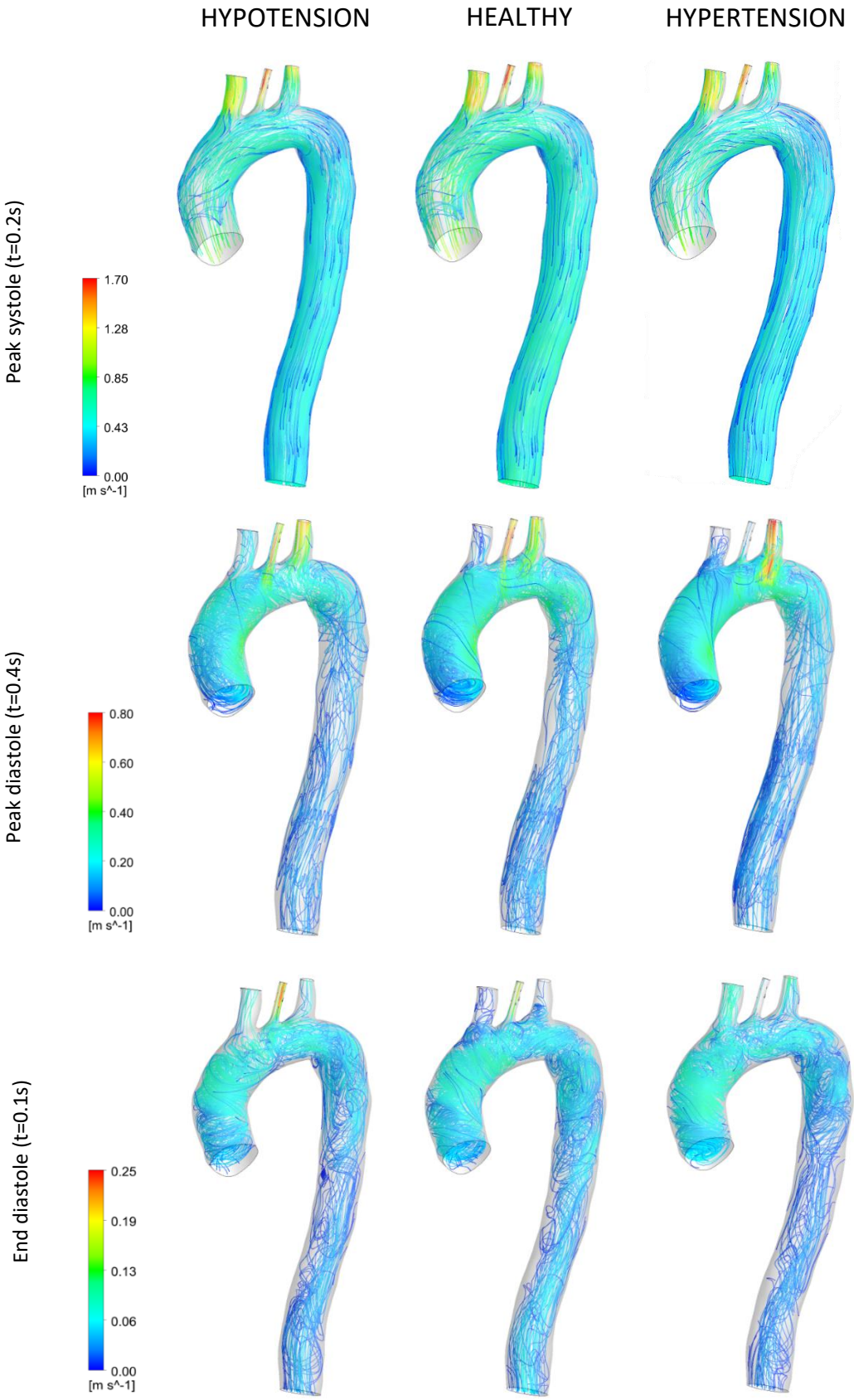

Figure 56 Flow patterns for the standard configuration in the 3D domain.

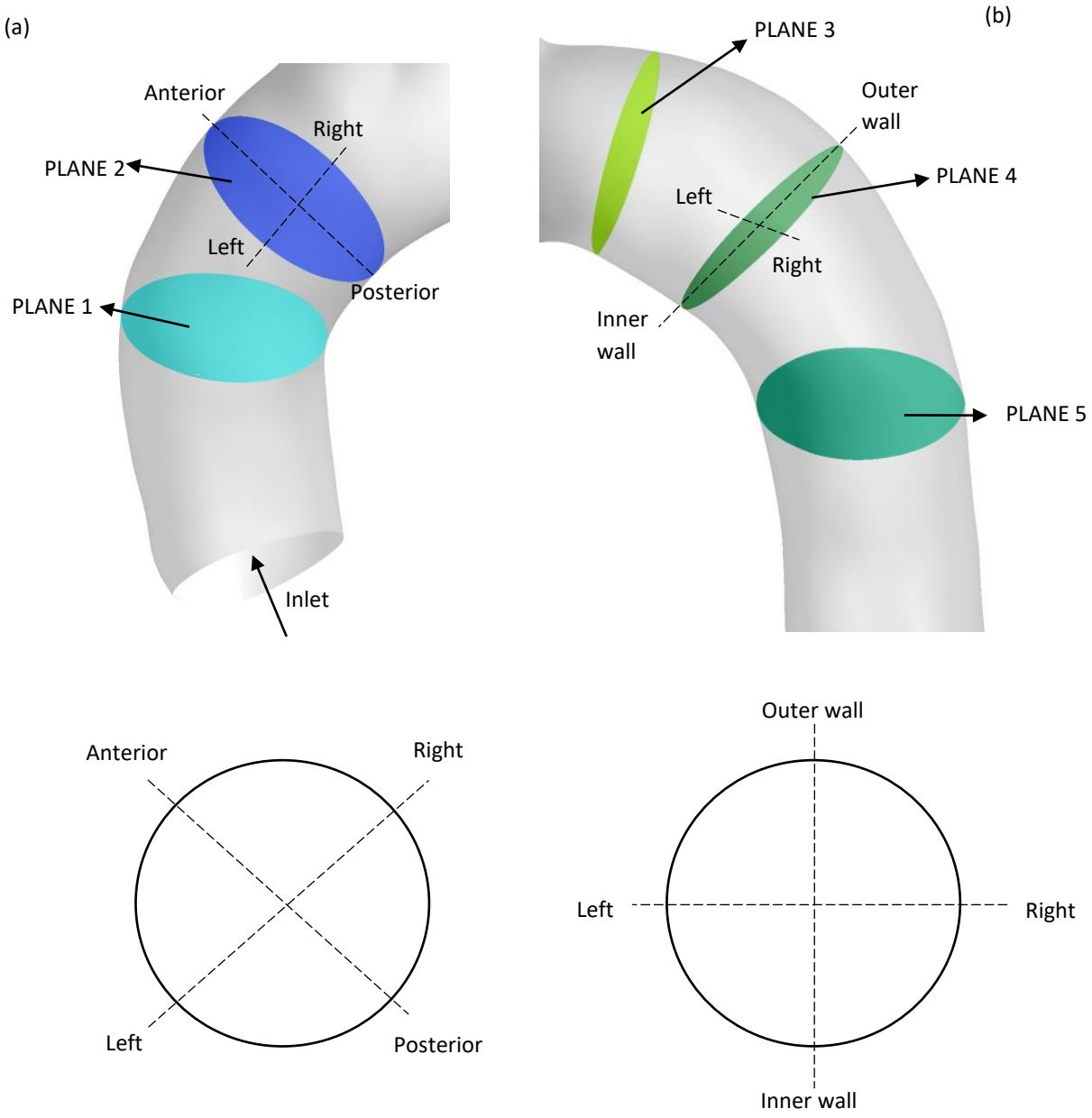

Figure 57 Planes designed in the standard configuration of the aortic vessel. (a) Planes in the ascending aorta, (b) planes in the proximal descending aorta.

(a) **Peak systole (t=0.2 s)**

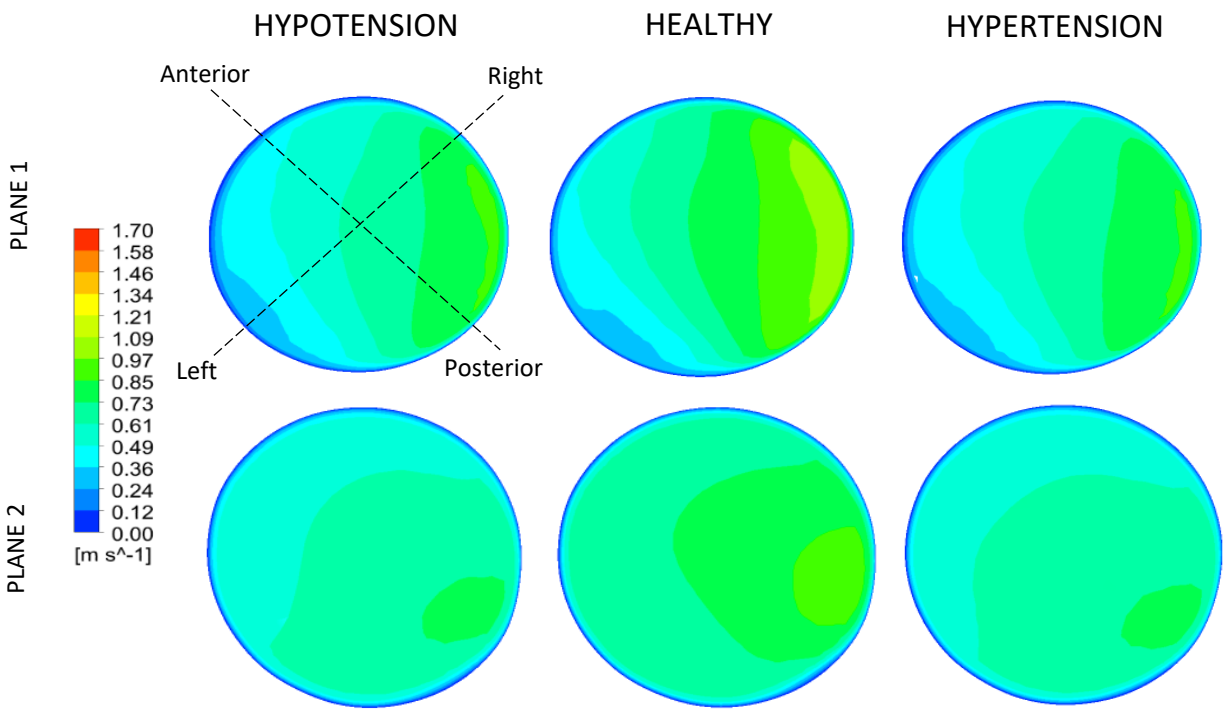

(b) **Peak diastole (t=0.4 s)**

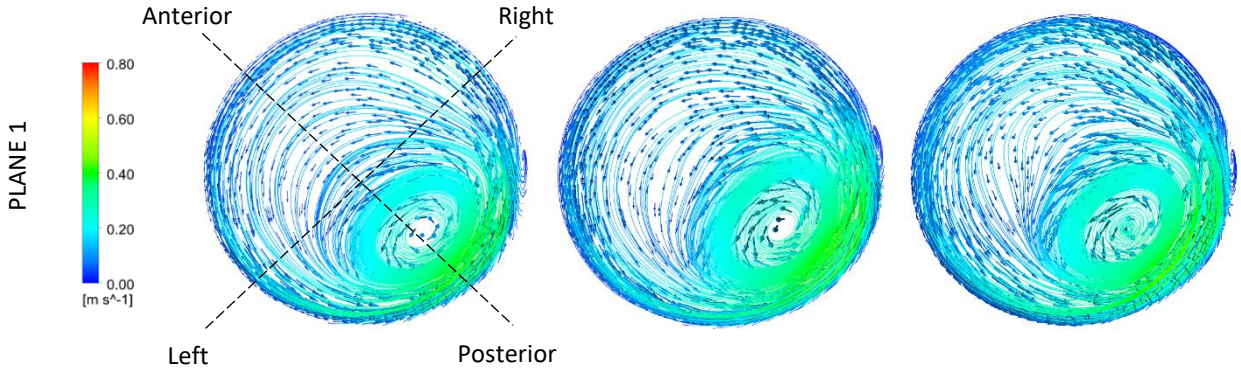

(c) **End diastole (t=0.1 s)**

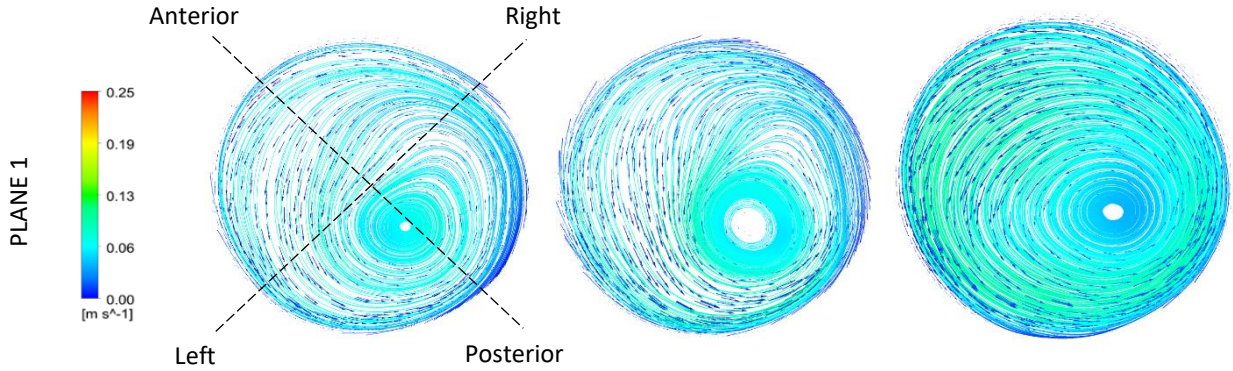

Figure 58 Results plotted in the ascending aorta of the standard configuration. (a) Velocity contour map at the systolic peak. (b) flow patterns at the diastolic peak. (c) Flow patterns at the end diastole.

Peak diastole (t=0.4 s)

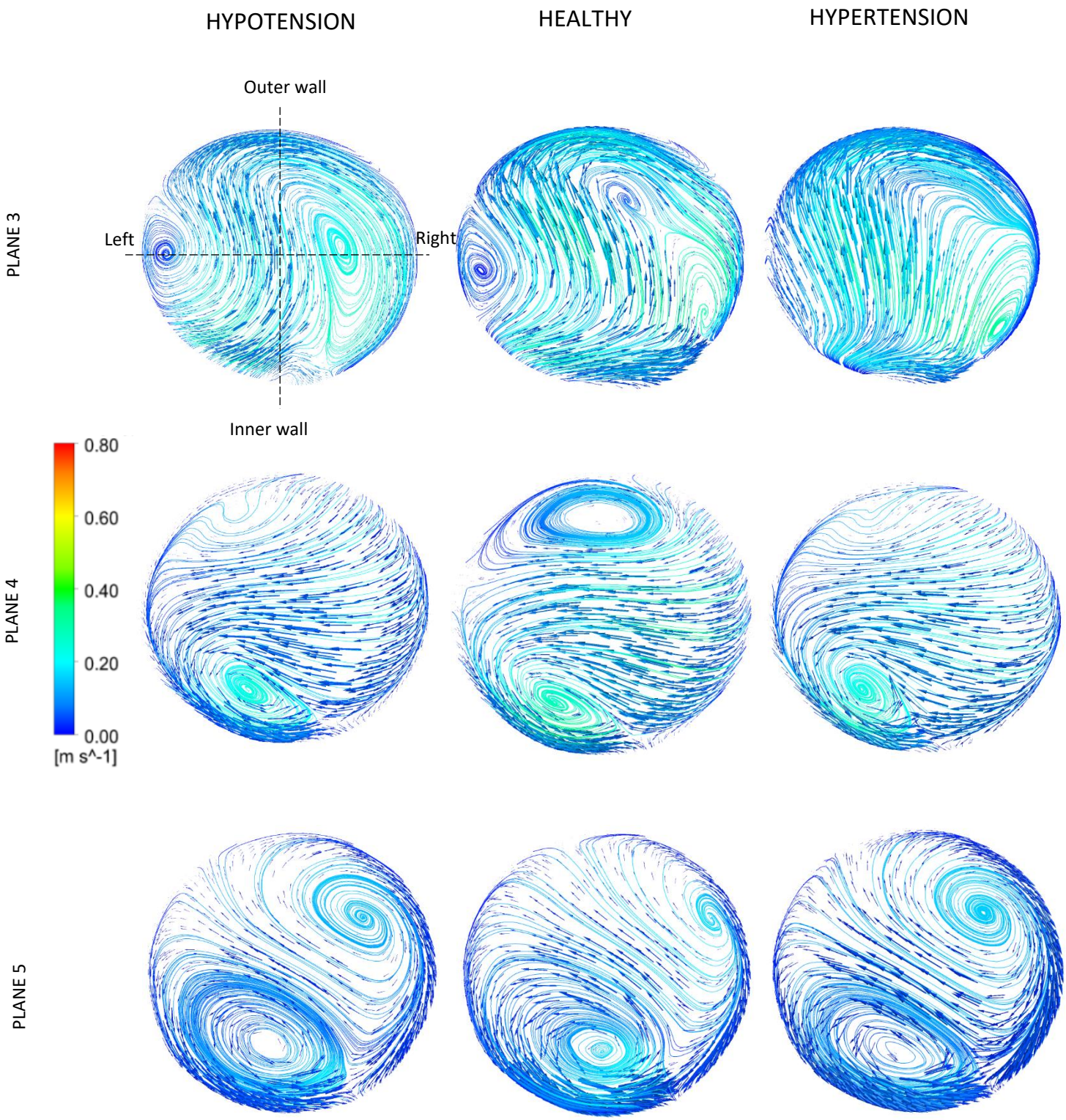

Figure 59 Flow recirculation patterns at the proximal descending aorta in the standard configuration.

4.3.1.2 WSS-based descriptors

A visual representation of the WSS descriptors pattern is reported in Figure 60, while a more quantitative analysis is given in

Table 7 where the mean and the maximum values are detailed for each index and for all the simulations run in the standard configuration. For the purpose of comparison all the results obtained for the same index were rescaled at the same velocity range.

Elevated TAWSS are observed both at the inlet and at the supra-artic vessels, with a peak value of 15 Pa at middle height for the LCCA configuration. The data in correspondence of the boundary surfaces were considered unreliable due to the fact that BCs setting can induce systematic errors. Relatively high values are shown at the level of the bifurcations on the outer wall of the aortic arch, especially in correspondence of the BCT where TAWSS is approximately 6 Pa. A qualitative comparison between BCs highlights that the healthy case presents in many areas higher TAWSS values than other conditions. This is confirmed by the mean TAWSS value reported in Table 7 for the healthy condition, that is 12-13% higher than the one measured for the hypertensive and the hypotensive cases.

The maximum OSI value of 0.5 is observed at multiple regions throughout the domain, including the posterior wall of the ascending aorta, the aortic arch close to the bifurcations and numerous spots along the descending aorta. The distribution is similar for the three sets of BCs, but there are some significant differences in the extension of the areas characterized by high values of the OSI. The size of the area can be an indicator of the probabilities AD tear can occur in that specific area; specifically, the higher the extension the more elevated is the probability the AD can initiate. The hypertensive condition present an evident larger area in correspondence of the SCA vessel entrance, 5 time larger than the one obtained for the other conditions. Moreover, the hypertension condition is characterized by more elevated OSI values throughout the whole vessel, as demonstrated by the mean OSI value reported in Table 7, that is 16% and 9% higher than the healthy and the hypotension cases, respectively.

For all the boundary conditions, regions characterized by high RRT values are observed at the descending aorta. Moreover for the hypertension and the hypotension conditions there is a relatively high RRT also in correspondence of the SCA. In general, the values obtained for the healthy case are lower than the ones of the other pressure conditions, as the mean RRT value is 23% and 27% lower than the hypotension case and the hypertension one, respectively (Table 7).

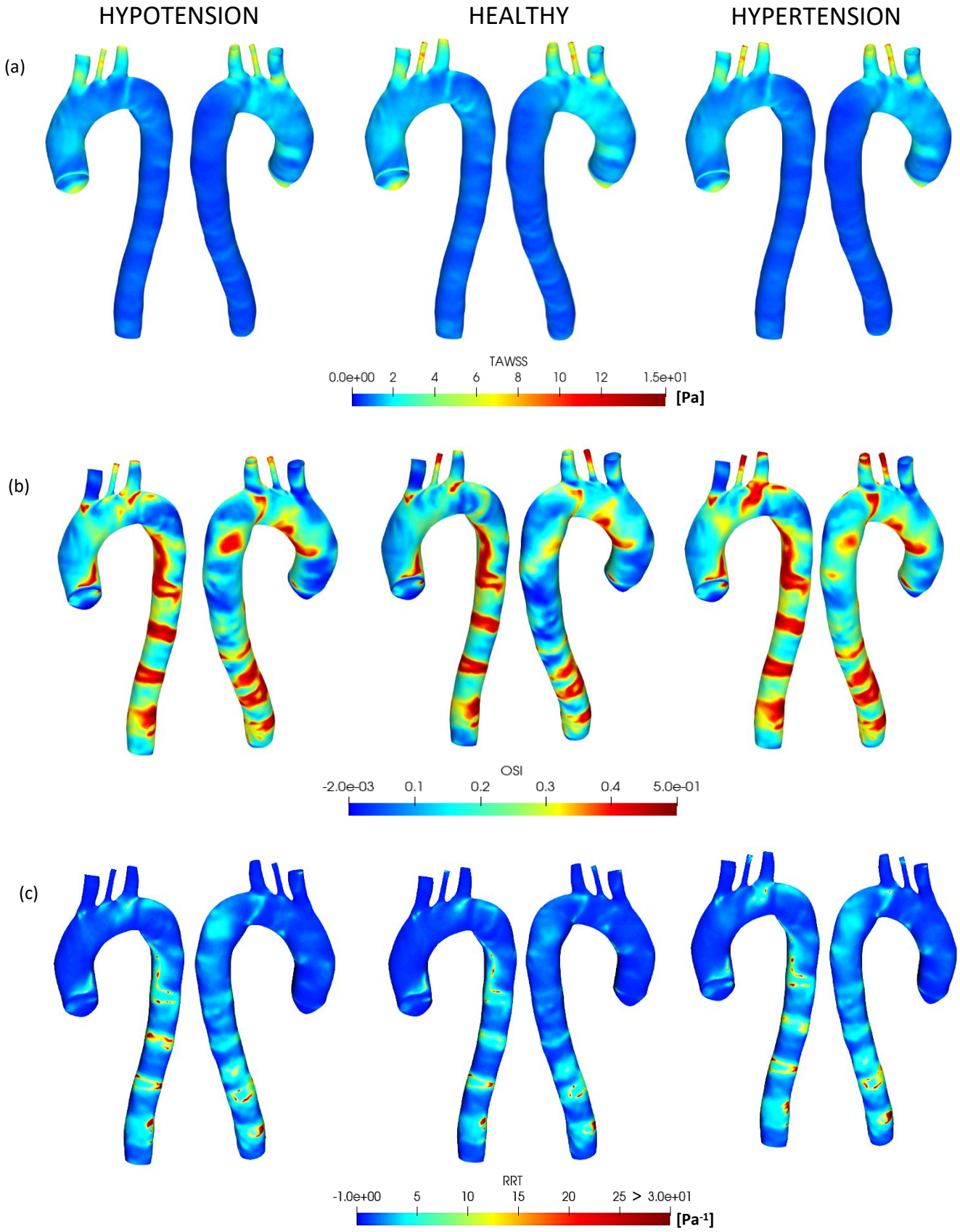

Figure 60 WSS-based descriptors calculated for the three set of BCs in the standard configuration. (a) TAWSS, (b) OSI, (c) RRT.

Pressure levels	TAWSS (Pa)		OSI		RRT (Pa^{-1})	
	Mean	Max	Mean	Max	Mean	Max
Hypotension	1.08	11.04	0.21	0.50	3.36	192.74
Healthy	1.23	14.34	0.19	0.49	2.57	193.34
Hypertension	1.09	15.40	0.23	0.49	3.54	236.47

Table 7 Mean and Maximum value WSS-based descriptors for the standard configuration.

4.3.1.3 Structural results

A representation of the maximum principal stresses and of the displacments of the structural domain is reported in Figure 61. The results were mapped at time 0.4 s when the maximum value of both stress and displacement occurs.

The results reported for the maximum principal stresses are referred to the outer surface of the wall. It should be mentioned that the distribution at the inner wall is different from the one at the outer wall, and indeed the maximum value of stress is registered at the inner wall and is not visible in Figure 61. A cut plane was inserted during the post-processing phase for the healthy case to show the area associated to the maximum stresses (Figure 62), i.e. a spot at the entrance of the BCT vessel. The stress distribution at the outer wall is approximately homogeneous throughout the aortic vessel, with no circumscribed peaks, while the wall stresses at the supra-aortic vessel are lower. The stress distribution assesses in which areas it is most probable for the dissection to propagate, as it gives information of the locations at which the tunica media is most solicited and can undergo the greatest histological changes. In this case it is of course the bifurcation area of the BCT. A significant difference among the boundary conditions is seen in the stress values: taken the healthy condition as baseline, a 44% decrease in the maximum value is observed for the hypotension condition and a 46% increment is measured for the hypertension one. The magnitude of the wall stress is directly proportional to the probability the AD tear will propagate, so it can be deducted that hypertension is the riskiest condition. The distribution of the displacement values shows a maximum at the outer wall of the descending aorta and on the lateral sides of the aortic arch. No deformation occurs at the supra-aortic vessels, which is consistent with the lower wall stresses in these areas. The maximum displacement registered changes accordingly to the BCs imposed, growing from 1 mm for the hypotension case to 2,5 mm in the hypertensive one.

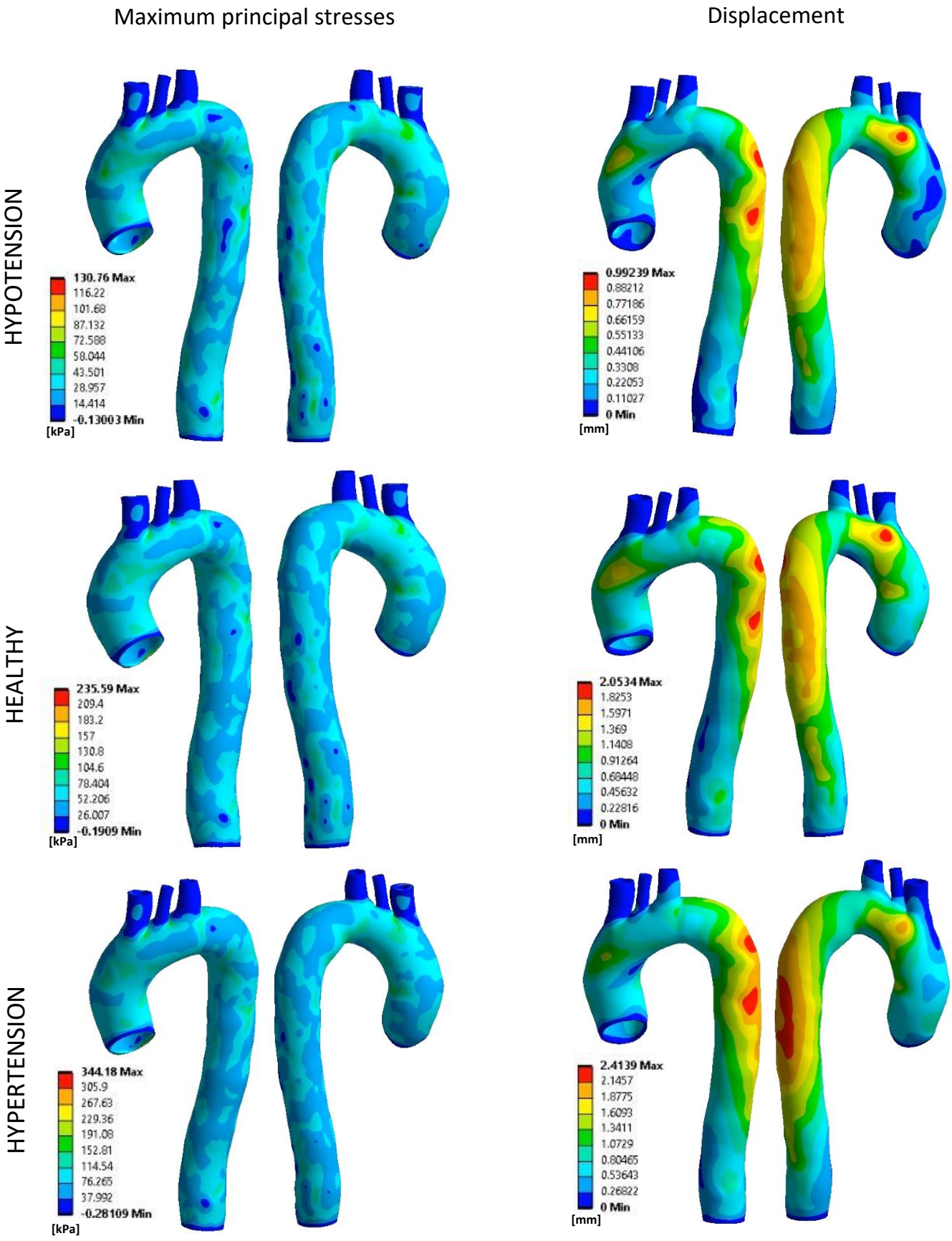

Figure 61 Structural results obtained in the standard configuration.

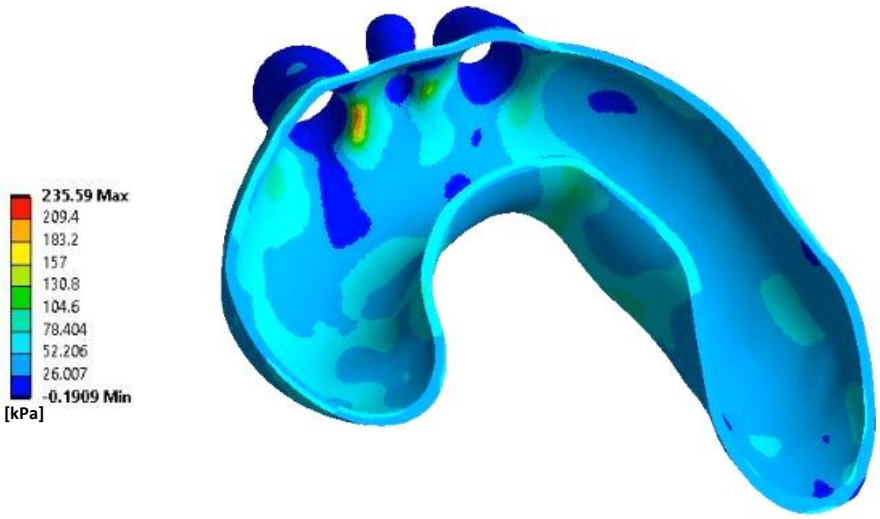

Figure 62 Detail of the maximum principal stresses at the inner wall of the bifurcation area.

4.3.2 Bovine arch configuration

4.3.2.1 Flow patterns

As for the standard configuration, flow patterns were represented through streamlines at the systolic peak (t=0.2 s), the diastolic peak (t=0.4 s) and the end diastole (t=0.1 s) for the three set of BCs (hypotension, healthy and hypertension) (Figure 63). For the purpose of comparison all the results at the same time step were rescaled at the same velocity range. Again, various planes were designed in the ascending aorta (PLANE 1b and PLANE 2b) (Figure 64, a), and at the proximal descending aorta the (PLANE 3b, PLANE 4b and PLANE 5b) (Figure 64, b). The data plotted on these planes maintain the velocity range reported for the total domain at the corresponding time step.

At the systolic peak (t=0.2 s) an organized flow with parallel streamlines is observed both in the ascending and descending aorta. No particular differences in the patterns are highlighted between the BCs, but the healthy condition presents a higher velocity magnitude. The velocity contours at PLANE 1b and PLANE 2b show that the maximum velocity is at the posterior left area of the aortic lumen (Figure 65, a), meaning there is a higher risk the AD initiates in this area.

At the diastolic peak (t=0.4 s) recirculation patterns are noticed in the ascending aorta, characterized by two counter rotating vortexes (Figure 65, b). Two vortices can be reported also on PLANE 3b, which is positioned right after the SCA at the end of the aortic arch. These areas present also high velocity magnitude so there is a high probability AD can develop here. Moving down along the descending aorta the streamlines progressively regularize and organize at the outer wall as shown at PLANE 4b and PLANE 5b (Figure 66), while at the inner wall an helicoidal pattern is maintained, especially in the hypotensive case. The distal descending aorta presents an increment in the velocity value, causing this region to be at high risk for AD. In the hypotension and in the healthy conditions the flow patterns converge towards the BCT vessel and present a peak value in the LCCA. In the hypertension case, instead, the flow is partially redirected towards the SCA and an helicoidal pattern is observed in the LCCA. It is believed that the recirculation in the LCCA could be related to the oscillations observed in the flow rate plot for the hypertension condition (Figure 54).

At the end diastole (t=0.1 s) a left-ended helicoidal flow is observed in the ascending aorta (Figure 65, c), which then evolves into disturbed flow in correspondence of the aortic arch where the bifurcation occurs. The flow then is organized in parallel streamlines in the descending aorta.

The data shown in this section suggest that the AD would probably initiate at the supra-aortic vessels, in the proximal descending aorta close to the SCA, or in the distal descending aorta.

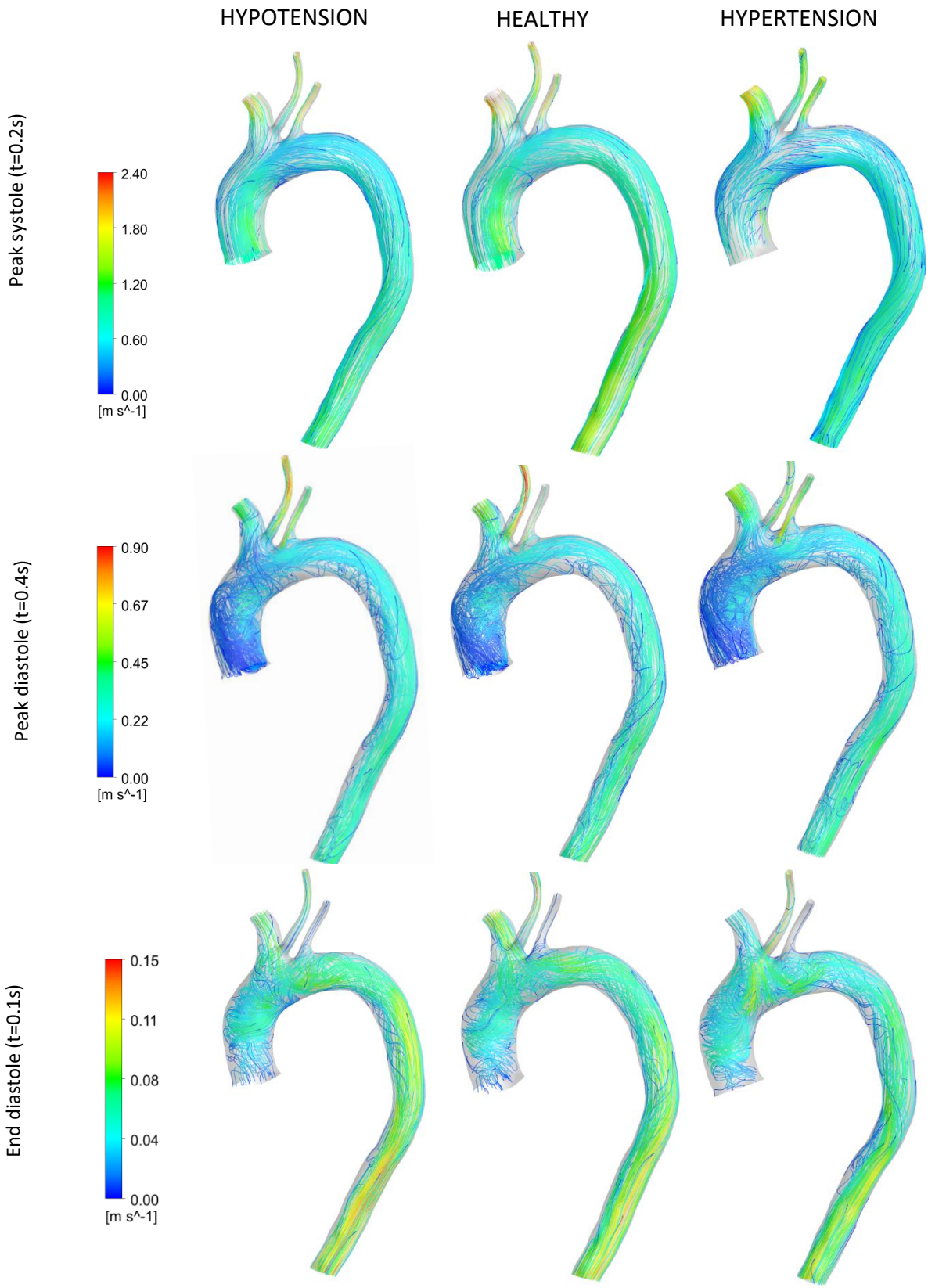

Figure 63 Flow patterns for the bovine configuration in the 3D domain.

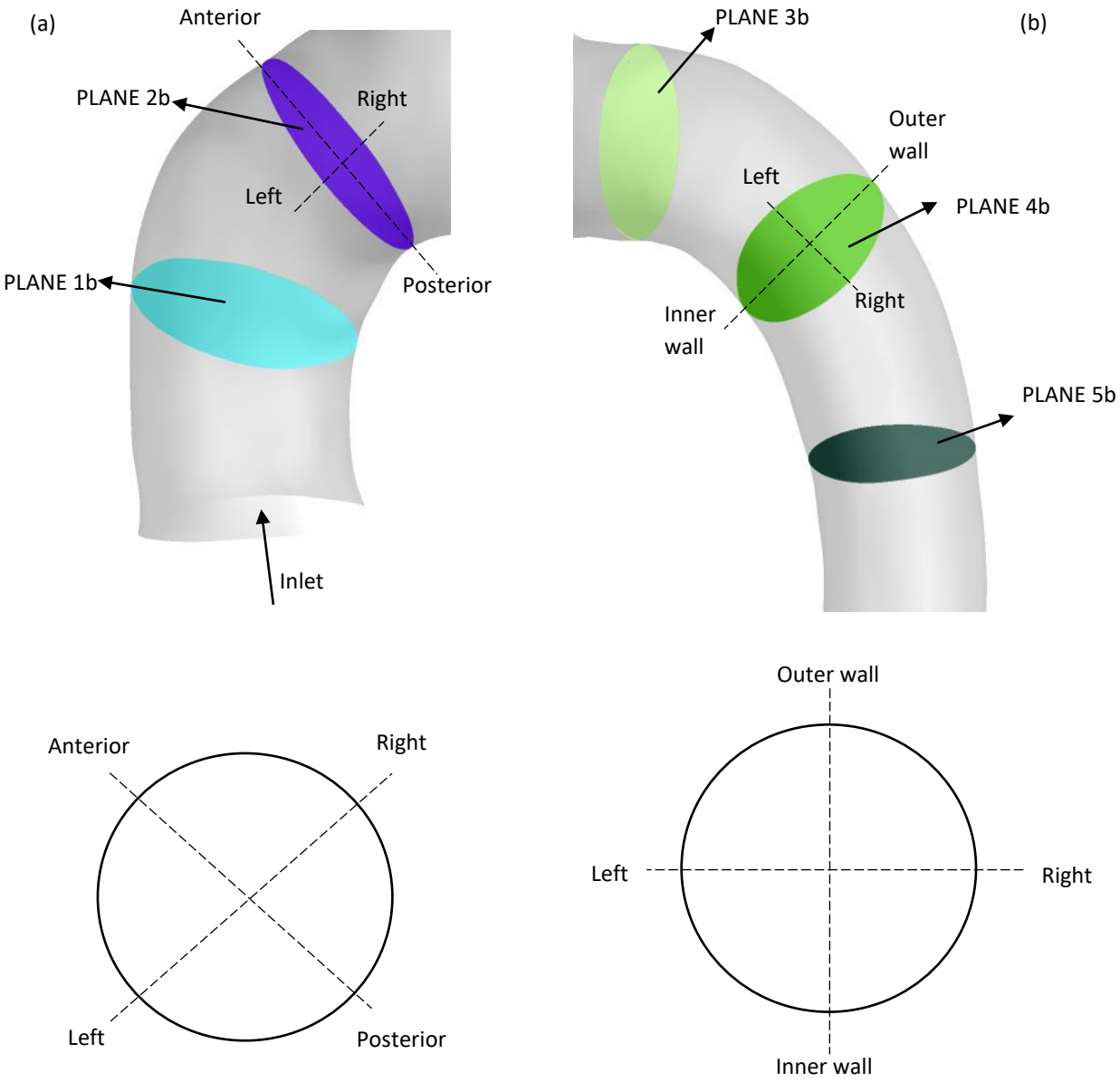

Figure 64 Planes designed in the standard configuration of the aortic vessel. (a) Planes in the ascending aorta, (b) planes in the proximal descending aorta.

(a) **Peak systole (t=0.2 s)**

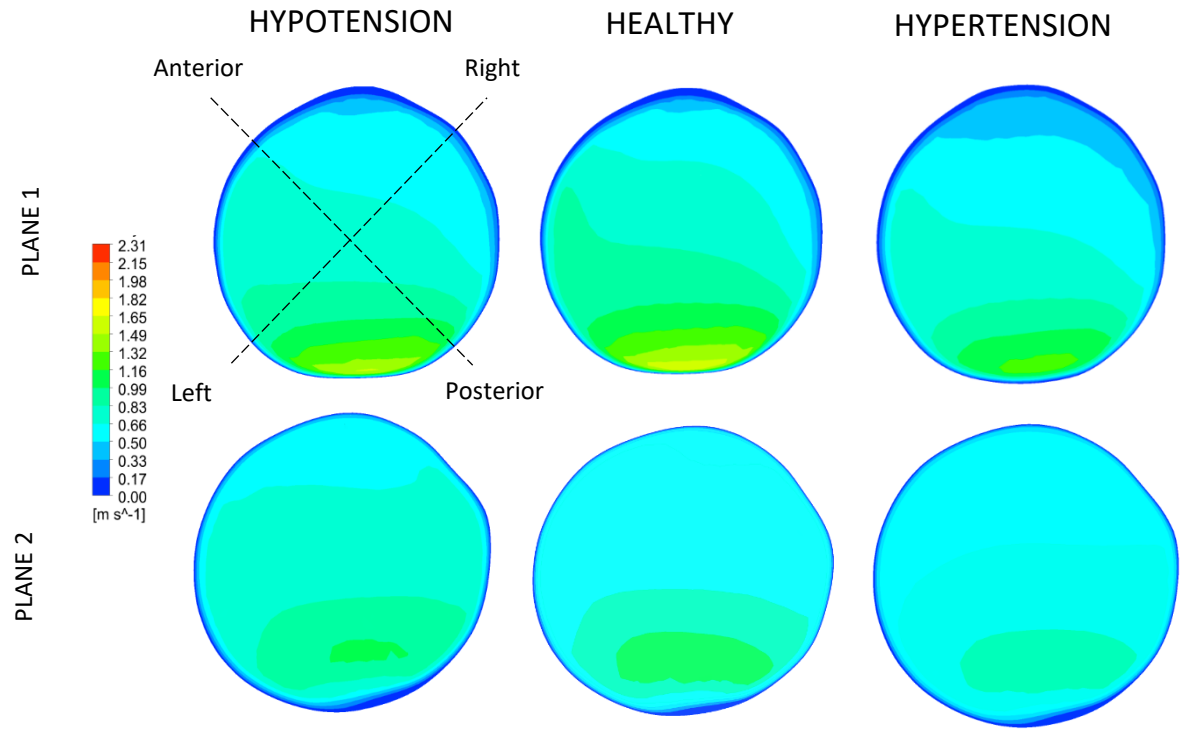

(b) **Peak diastole (t=0.4 s)**

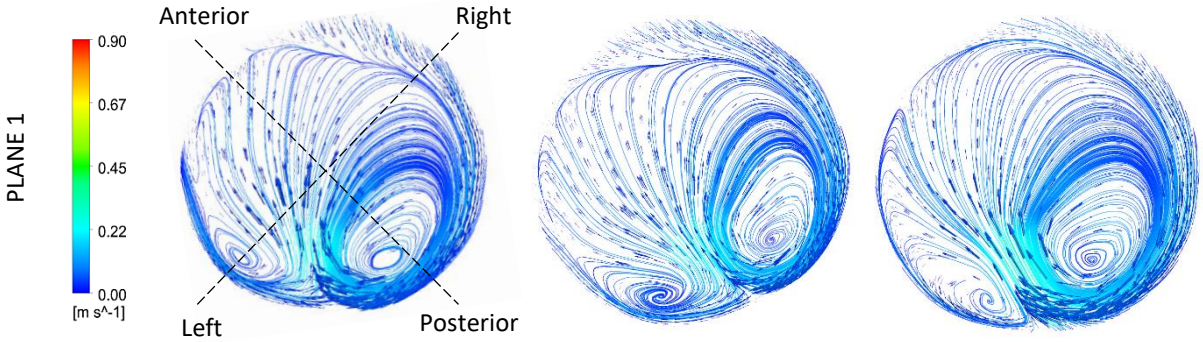

(c) **End diastole (t=0.1 s)**

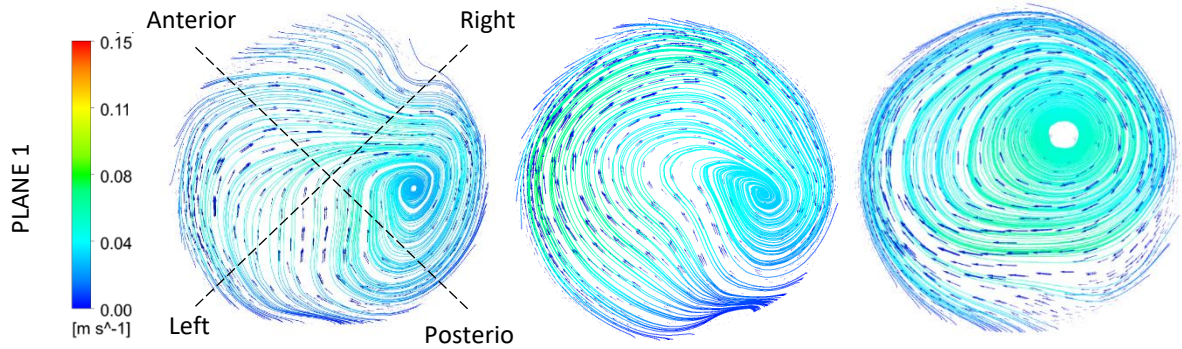

Figure 65 Results plotted in the ascending aorta of the bovine configuration. (a) Velocity contour map at the systolic peak. (b) flow patterns at the diastolic peak. (c) Flow patterns at the end diastole.

Peak diastole (t=0.4 s)

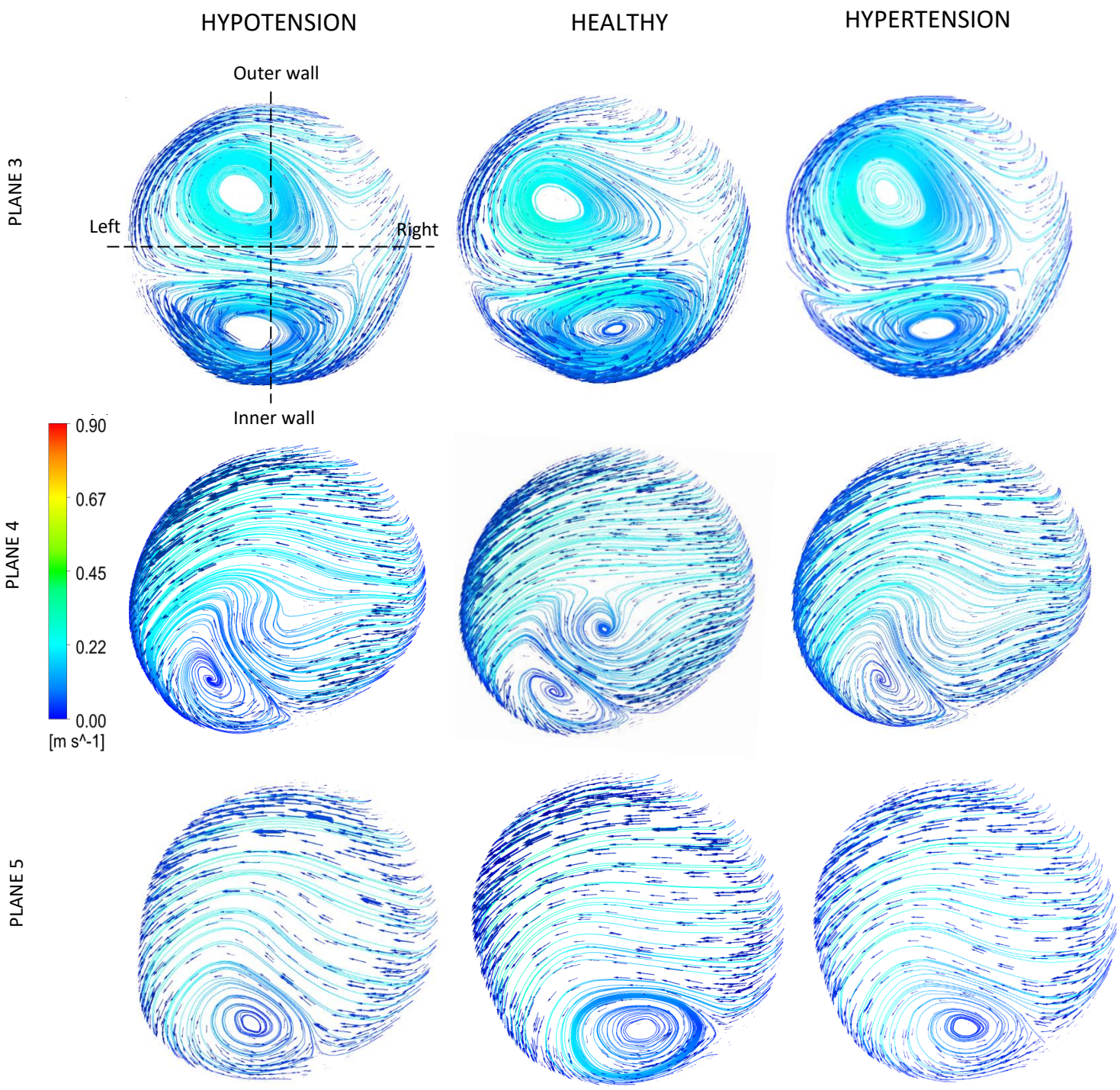

Figure 66 Flow recirculation patterns at the proximal descending aorta in the bovine configuration

4.3.2.2 WSS-based descriptors

A visual representation of the WSS pattern is reported in Figure 67, while a quantitative analysis is given by the Table 9 where the mean and the maximum values are detailed for each index and for all the simulations run with the bovine arch configuration. For the purpose of comparison, all the results obtained for the same index were rescaled at the same velocity range.

Elevated TAWSS were detected at the supra-aortic vessel, especially at the distal portion of the BCT and the LCCA, and at the middle height of the SCA. In these areas, the TAWSS reach values of 8 Pa (excluded the peak values at the boundaries), while at the bifurcation level they decrease to 2-3 Pa, which is still higher than the mean value of each simulation (Table 8). Furthermore, high values of the descriptor are observed in the distal part of the descending aorta. The TAWSS levels are higher for the healthy case, consistent with the higher velocity magnitude observed for this pressure condition. The mean value measured for the healthy condition is 14% and 17% higher than the hypertension and the hypotension case, respectively.

The OSI distribution has a peak value in correspondence of the anterior wall of the ascending aorta, the bifurcation areas of the three supra-aortic vessels, and the inner wall of the distal descending aorta. The red areas associated to the maximum OSI values have similar distribution and dimension when the BCs are compared. However, the hypertension case presents a red area at the outer wall of the aortic arch right after the SCA, which is associated to lower values in the other two cases. It can then be deducted that an increase in the pressure level may increase the probability for AD formation near the SCA. In general higher OSI levels are observed throughout the vessel for the hypertension condition: an increase by 12% and 17% is registered with respect to the hypotension and the healthy conditions respectively (

Table 8). A significant difference is reported especially at the ascending aorta, where however it is improbable an AD develops because of the low TAWSS values.

The RRT values are maximum in the ascending aorta and in correspondence of the bifurcations. No relevant differences are registered between the three pressure levels, but it can be noticed that the healthy patient is overall characterized by a lower value of the index: a decrease by 17% and 22% is measured from the hypotension and the hypertension conditions, respectively.

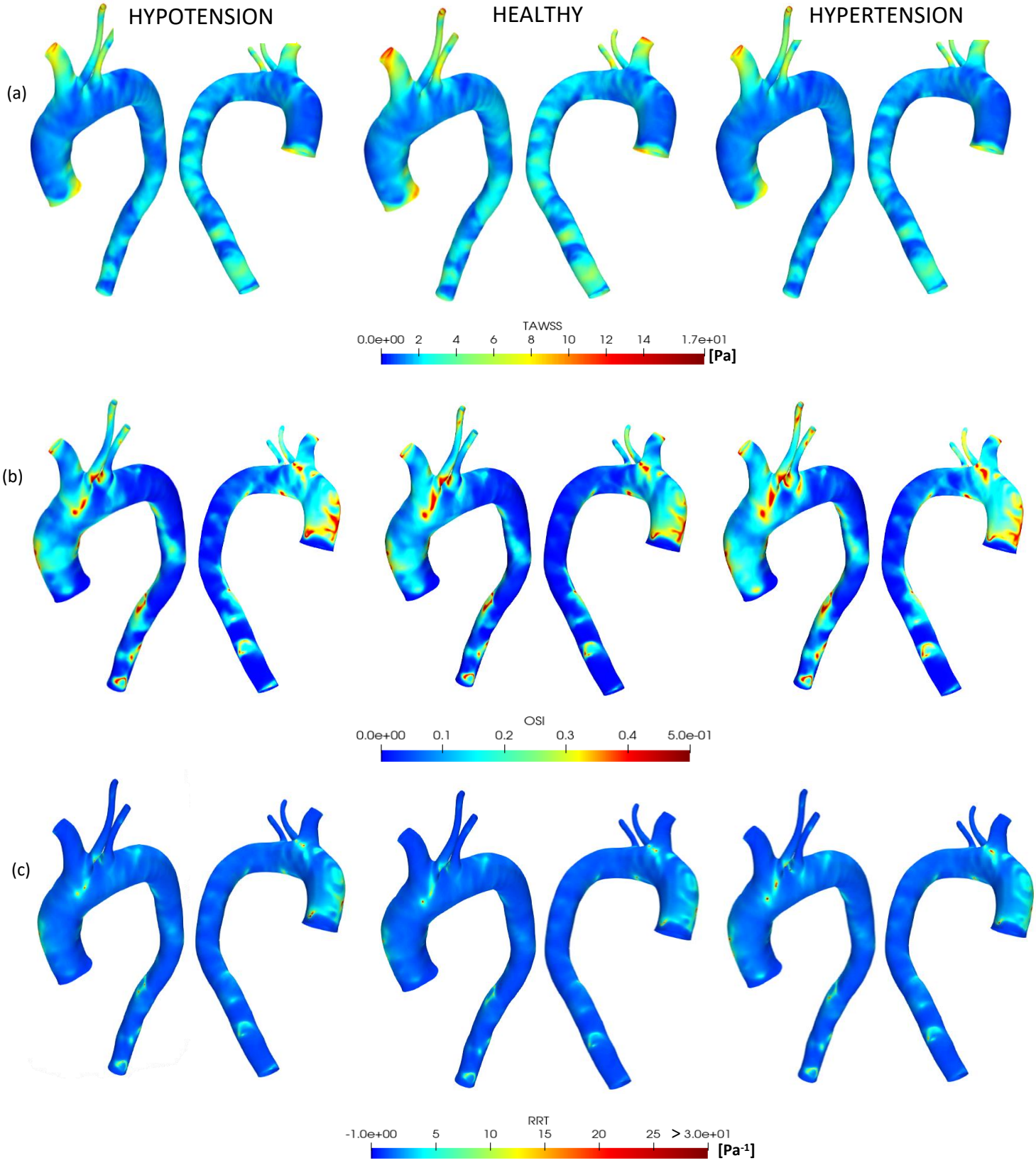

Figure 67 WSS-based descriptors calculated for the three set of BCs in the bovine configuration. (a) TAWSS, (b) OSI, (c) RRT.

Pressure levels	TAWSS		OSI		RRT	
	Mean	Max	Mean	Max	Mean	Max
Hypotension	1.79	14.10	0.10	0.50	1.17	126.71
Healthy	2.10	17.24	0.09	0.49	0.97	64.88
Hypertension	1.73	15.08	0.11	0.49	1.25	107.12

Table 8 Mean and Maximum value WSS-based descriptors for the bovine arch configuration

4.3.2.3 Structural results

A representation of the maximum principal stresses and of the deformation of the structural domain is reported in Figure 68. The results were mapped at time 0.4 s when the maximum value of both stress and deformation occurs over the cardiac cycle. The view from a cut plane in the healthy case is reported in Figure 69 to better assess the maximum principal stresses at the bifurcation area between BCT and SCA.

The maximum principal stress distribution is similar for the three conditions, presenting a peak value at the lateral ascending aorta, in correspondence of the BCT bifurcation area and down the descending aorta at middle height. A negative value of the stresses is measured at the LCCA, the SCA and at the inner wall of the descending aorta. The stress maximum value changes among the different BCs, decreasing by 38% for the hypotension case and increasing by 37 % for the hypertensive one. According to the considerations made in section 4.3.1.3 also in the bovine arch configuration, the probability of AD initiation increases with the pressure level.

The maximum displacements correspond to the areas characterized by higher values of stresses. In general, high deformation is observed throughout the whole vessel, even at the supra-aortic vessels where negative values of stresses were measured. The magnitude of the displacement increases from 1,5 mm in the hypotensive case to 2,5 mm in the hypertensive one.

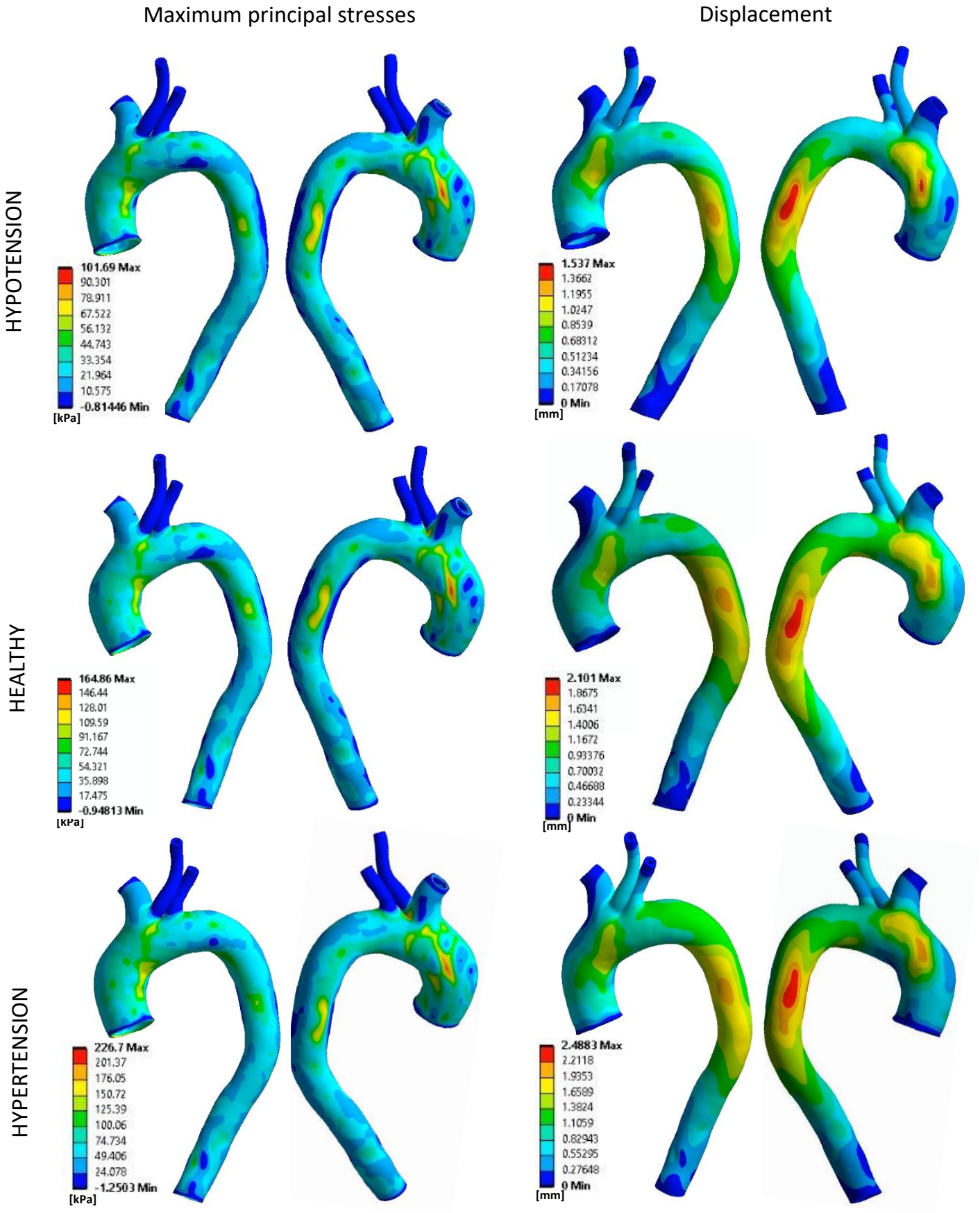

Figure 68 Structural results obtained in the bovine configuration.

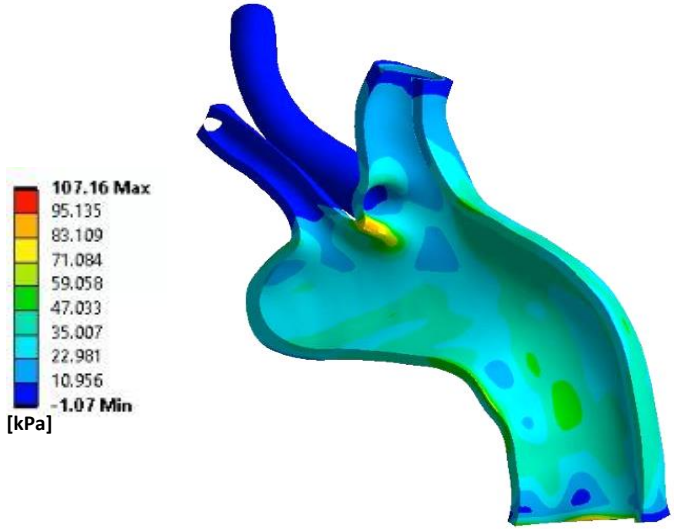

Figure 69 Detail of the maximum principal stresses at the inner wall of the bifurcation area in the bovine configuration.

4.3.3 Discussion

The analysis performed for the two configurations allows to make some considerations on the effect of the BCs on the AD initiation and propagation in the aortic vessel. Looking at the hemodynamic pattern, first of all it can be noticed that the healthy case presents higher velocity values throughout the vessel and as a consequence more elevated TAWSS values. This a direct consequence of the velocity curve imposed at inlet which is higher for the healthy case.

Secondarily it can be observed that in the hypertensive condition the flow is redirected toward the SCA vessel, leading to higher velocity values in this area and to an increase in the extension of the locations associated to maximum OSI values. In particular in the standard configuration it has been observed a significant acceleration of the blood through the SCA vessel where peak velocity values are measure and a significant increase of the regions characterized by elevate OSI on the lateral wall of the aortic arch.

Finally substantial change in the maximum principal stresses magnitude at the wall is observed when a pressure variation occur. An increase up to 46% can be measure in the stress level for a 15% change in the pressure levels imposed at the outlet.

Summing up all the factors, it can be stated that the riskiest condition that can lead to the AD pathology is the hypertension, both because it shows the most extended areas associated to high OSI and because it imposes the higher stress values at the wall.

4.4 Standard vs bovine configuration

4.4.1 Flow patterns

Figure 70 represents the flow patterns in the aortic arch for the standard and the bovine configurations at the systolic peak (t=0.2 s), the diastolic peak (t=0.4 s) and the end diastole (t=0.1s). As the previous sections demonstrated that the flow patterns were similar among different boundary conditions, a single case was reported for the comparison, precisely the hypertensive one as it is the most clinically interesting condition. The velocity ranges for each case was maintained to allow some considerations on the velocity magnitude. Other than that Table 9 report the flow rate percentage measured at the supra-aortic vessel at the systolic peak (t=0.2 s), to check if any difference is generated by the changes in the configurations.

At the systolic peak (t=0.2 s) the flow patterns develop in the same way for both geometries through the vessel, with the flow organized in parallel streamlines. There is instead a high variance in the velocity magnitude, as a maximum value of 1.7 $m * s^{-1}$ and of 2.4 $m * s^{-1}$ was measured respectively for the common and the bovine configurations. The bovine arch configuration will have then a higher probability for tear formation.

At the diastolic peak (t=0.4 s) it can be seen a substantial difference in the organization of the flow patterns. In the standard configuration the flow tends to be more organized in the ascending aorta to then disrupt into recirculation patterns in the descending aorta, in the bovine arch case instead an opposite behaviour is observed, which presents disturbed flow in the ascending aorta and more organized streamlines at the descending one. It is believed that the lack of the bifurcation in the last part of the aortic arch has a role in favouring a more organized flow in the descending aorta of the bovine arch configuration. This suggests that the bovine arch configuration have a higher probability to develop a type B AD. The velocity magnitude is still higher in the bovine arch geometry, but the gap is reduced to approximately 0.1 $m * s^{-1}$. At the end diastole (t=0.1 s) a disturbed flow is observed in the whole domain for both geometries, anyway some difference can be detected. An acceleration of the flow towards the BCT occur in the bovine arch configuration, as well as an helicoidal pattern through the LCCA. Furthermore, the bovine arch presents a much more organized flow through the descending aorta.

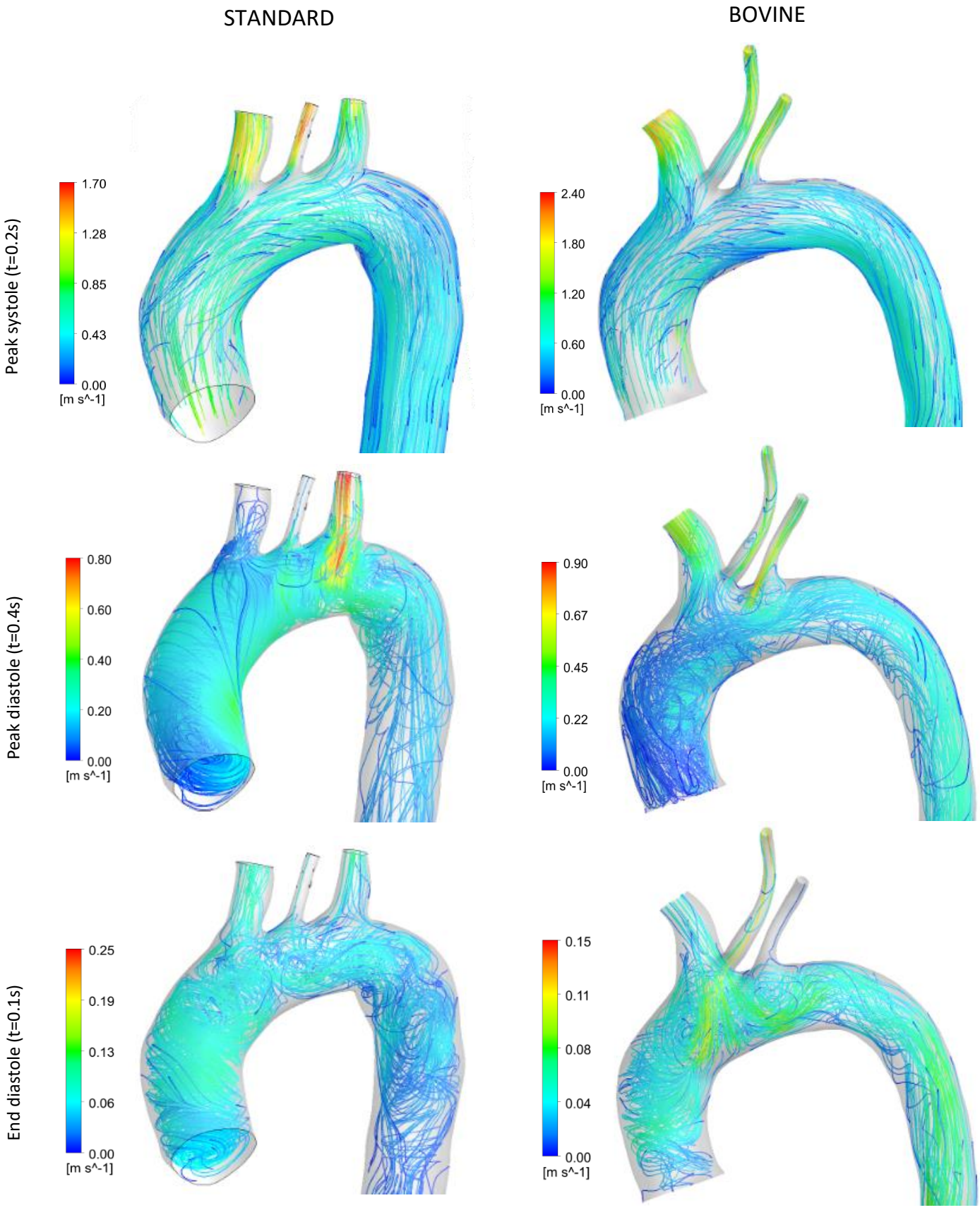

Figure 70 Flow patterns in the aortic arch for the standard and the bovine arch configurations.

Table 9 shows that the geometry influences the flow rate distribution through the supra-aortic vessels. No big differences are shown in the output of the LCCA, while there is a clear increment of the flow through the BCT and a reduction in the SCA, moving from the standard to the bovine configuration. This is probably due to the different dimensions of the two vessels in the two geometries, indeed the BCT entrance section is much larger in the bovine arch geometry allowing to canalize a greater percentage of the flow rate. On the contrary SCA presents a smaller diameter throughout the whole length of the vessel.

Artery	**Flow rate (%)**	
	Standard	Bovine
BCT	26.24	37.63
LCCA	3.79	4.24
SCA	12.95	5.27

Table 9 Flow rate percentage at the supra-aortic vessels.

4.4.2 WSS-based descriptors

For the purpose of comparison of the hemodynamic descriptors between the two configurations, the geometries were divided in patches through the use of VMTK. To each patch is associated a value, calculated by making the mean of the data associated to the nodes belonging to the patch. The results are shown in Figure 71 only for the hypertensive case.

Looking at the TAWSS distribution it can be noticed that the bovine arch geometry presents a larger number of patches with non-zero value with respect to the standard configuration. In particular at the descending aorta most of the patches present an index value equal or greater than 2 Pa. This is consistent with the velocity patterns observed and with the consideration made in the previous section, and confirm that the bovine arch configuration is most prone to type B AD. Besides that, some differences are reported at the supra-aortic vessels. At the LCCA level, the standard configuration shows a TAWSS value of at least 5 Pa for all the patches, while in the bovine arch the bifurcation area in correspondence of the BCT present lower values (around 2 Pa). Also, high values are observed in the distal portion of the BCT and throughout the length of the SCA in the bovine configuration.

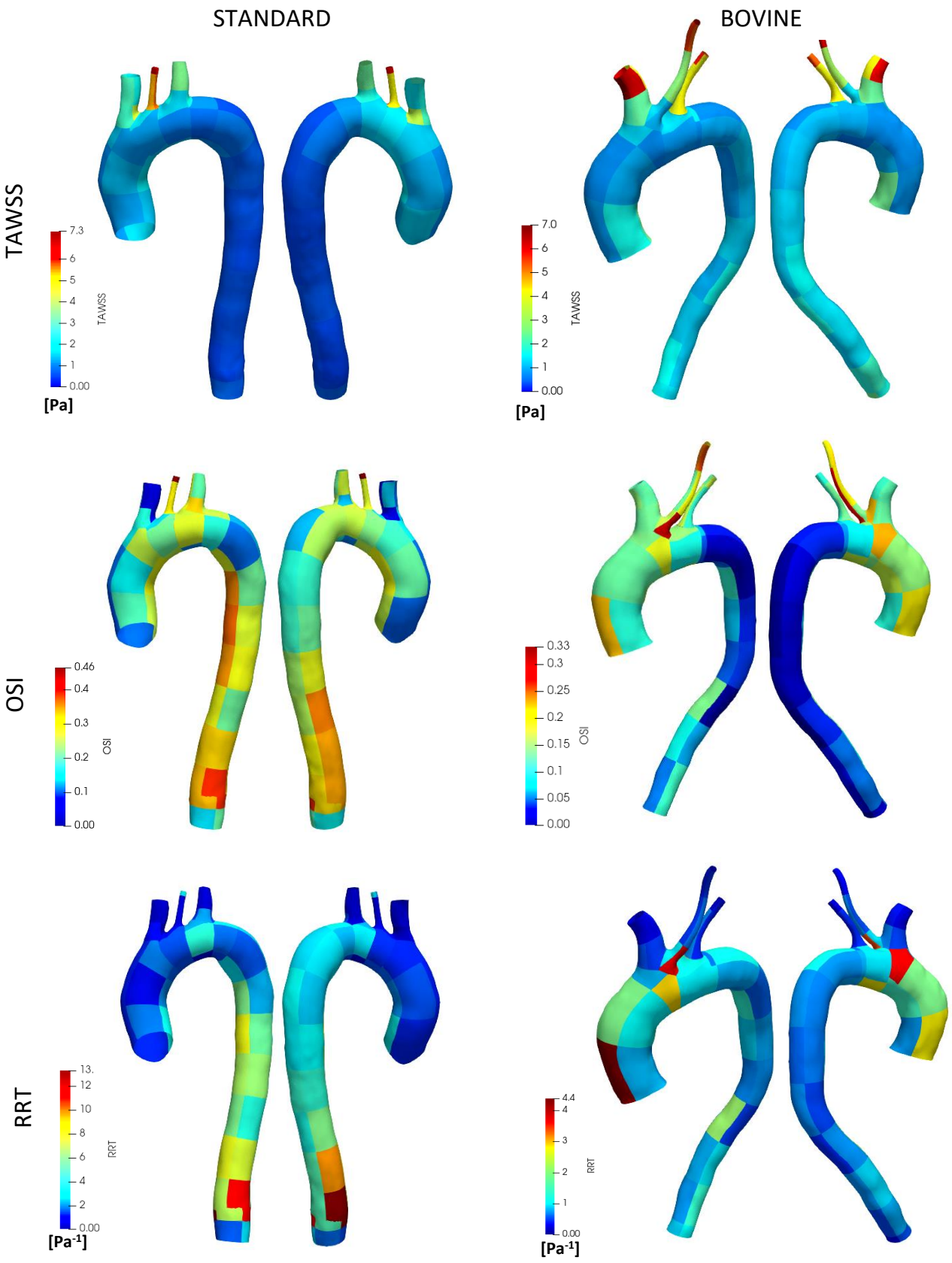

Figure 71 TAWSS, OSI and RRT comparison by using patches.

The OSI distribution is specular for the two configurations, as the standard aortic arch shows OSI peak values in correspondence of the descending aorta, while the bovine configuration shows higher values in the ascending aorta. Also, elevated OSI values are measured for both configurations in correspondence of the patches next to the SCA and the BCT entrances.

Similar consideration to the ones made for the OSI can be made for the distribution of the RRT value. The ranges measured for the two geometries are significantly different, with a peak value of 13 Pa^{-1} for the standard case and of 4.4 Pa^{-1} for the bovine one.

4.4.3 Structural results

In Figure 72 the maximum principal stress distribution and the displacement are reported for the hypertensive condition at time 0.4 s, when both quantities reach their maximum.

Some significant difference in the distribution of the maximum principal stresses can be identified between the two geometric configurations. For the standard case, a peak value is registered only at the entrance of the BCT vessel, while for the bovine arch configuration a maximum can be identified also at the ascending aorta and at the mid descending one. This means there exist more locations in the bovine arch configuration in correspondence of which the AD might develop in case tear formation occurs. However the maximum value reached by the bovine arch geometry is much lower than the one obtained for the standard configuration: a percentage difference of 34% is measured between the two configurations. This suggest that the standard configuration is overall characterized by a higher probability for the AD to propagate.

Also the displacement map is different, the standard configuration shows large displacement throughout almost the whole descending aorta at the outer wall, and at the aortic arch in the area close to the BCT and LCCA. Instead, in the bovine arch geometry large deformations are observed on the lateral sides of the descending aorta, plus a spot in the ascending aorta close to the entrance of the BCT. The displacement values are similar, with a maximum value of almost 2.5 mm in both cases.

The comparison between the two configurations suggests that the bovine arch geometry has a higher probability to develop type B AD, and that the standard configuration has a higher probability for AD to develop if tear formation occurs.

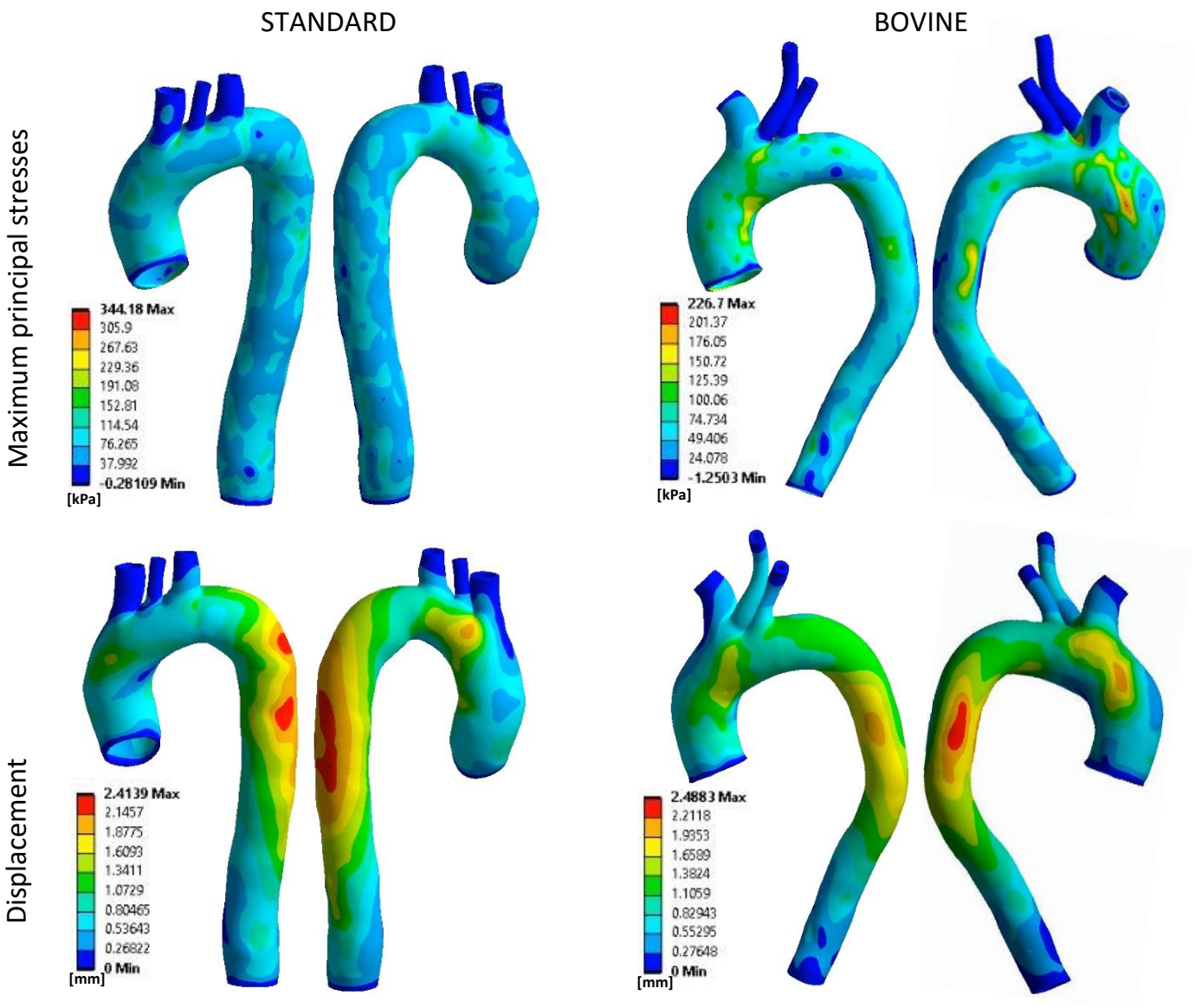

Figure 72 Maximum principal stresses and displacement for the standard and the bovine arch configurations.

5 Conclusions

In this chapter final considerations are made, highlighting the limitation of this work and suggesting future direction in which it can be developed.

5.1 Conclusions

In this work thesis, 2-way FSI simulations were implemented in order to assess the influence of different pressure conditions and geometry configuration on the location at which the AD could initiate and propagate. Three different pressure levels were implemented (hypotension, normotension and hypertension) through the use of pressure curves computed through a multi-dimensional model developed by the start-up Computational Life. A subject with a common configuration of the aortic arch and one with a bovine arch configuration were compared.

The results obtained suggest the variation of the BCs do not affect the areas at which tear formation may occur, but they do have a major role in determining the probability for the aortic vessel to experience the dissection pathology. By increasing the pressure level, an acceleration of the flow through the SCA vessel was observed, which leads to elevated velocity values and to a greater extension of the area characterized by elevated OSI values (5 times larger than in the other conditions). As a result, the hypertension condition presents a higher probability for the AD to develop in the aortic arch in correspondence of the SCA bifurcation. Also, the pressure level has been shown to be directly proportional to the maximum principal stresses registered throughout the vessel. In particular for the standard configuration, taken the healthy condition as baseline, a 44% decrease in the maximum value is observed for the hypotension condition and a 46% increment is measured for the hypertension one. In the bovine configuration instead, a 38% decrease is seen for the hypotension condition and a 37 % increment occurs for the hypertensive one. Given that higher stress values are associated with a higher probability for the AD to propagate into the tunica media, the hypertension case is confirmed to be the riskiest condition for this pathology. This is consistent with the results obtained in previous studies and with the clinical outcomes of patients with high blood pressure [29, 30].

The aortic arch configuration is shown to have an impact on the patterns of both hemodynamic and structural quantities. Higher flow organization, and consequently higher TAWSS values, are observed respectively at the ascending aorta for the common configuration of the aortic arch and at the descending aorta for the bovine arch configuration. The bifurcation area is critical for both configurations, because of the high recirculation patterns generated in the aortic arch by the bifurcation of the supra-aortic vessel. It can be stated that, according to the results obtained, the standard configuration present a higher probability for the AD to

initiate at the posterior wall of the ascending aorta, the bifurcation area of the BCT and the SCA, and the LCCA vessel. In the bovine arch configuration, instead, tear formation has a higher probability to occur in correspondence of the bifurcations of the supra-aortic vessel or at the distal the descending aorta. This analysis suggests that the bovine arch configuration favours the development of type B AD with respect to the standard configuration. This result is in accordance with clinical studies that study the prevalence of subjects with bovine arch condition within the AD patients: they show that only the 27% of the subject which experience type A AD condition presents a CILCA anomaly at the aortic arch, against a 39% for patient with type B AD [4, 86]. Also structural results show different patterns between the two configurations. The standard geometry has only one spot where the peak value is observed, which is in correspondence to the entrance of the BCT. In the bovine arch geometry instead multiple regions characterized by the maximum wall stresses are observed, which comprehend the lateral ascending aorta, the bifurcation area of the BCT and the LCCA, and the descending aorta. This means that the bovine arch configuration has more regions at which if a tear formation occurs there is a high probability it will propagate.

In recent years, the interest toward the AD pathology has grown exponentially as the mortality rate associated to this condition is still very elevated. In particular, the research for a predictor that allows to individuate patients at risk of AD, in order to intervene by time and to simplify the recognition and the diagnosis of the pathology. In this context, this work thesis gives a deeper insight on the correlation between the AD pathology and the pressure conditions that the patient can experience, and between the AD pathology with the geometry of the vessel.

5.2 Limitations

The FSI model implemented in this study is affect by some limitations and approximations:

- The hypertension condition was modelled only by changing the resistances of the systemic circulation. The cardiac output was maintained constant, causing the velocity to be lower in the hypertension condition than in the healthy case. This is a conservative choice that do not affect so harshly the stress condition at the wall . For a complete study of this condition a variation in the ejection power should be taken into consideration.

- The arterial wall was modelled as an isotropic material. Despite the fact this assumption is widely accepted in literature, this can affect the accuracy of the structural result. a more complete constitutive model should be adopted to obtain more precise results in the structural domain.
- No follow-up of the patients' conditions was available to validate the hypothesis that have been made in this research. Having a feedback on whether or not the patient has effectively developed the AD pathology and in the expected areas is fundamental to find a correlation between computational data and clinical results.
- the simulation time of an FSI model is significantly higher compared to a simpler CFD model or to a simple structural analysis (5-6 days depending on the simulation). To reduce as much as possible the computational cost the model has been simplified as much as possible, choosing the coarser computational grid possible, avoiding the refinement and choosing a lower order numerical model in the Fluent solver. This might influence the accuracy of the results obtained.

5.3 Future directions

The present research work opens up to possible future work and methods improvement.

First of all, it would be of great interest to find a way to make the Computational life model interact directly with the Ansys Software. The extraction of the data from the model, followed by the implementation of the velocity and pressure curves in Fluent, is not the most efficient workflow and have caused some discrepancies in the flow rate curves, particularly in the backflow phase. The development of these boundary conditions is of high interest as they allow to calculate with an acceptable computational cost specific pressure and flow conditions. At the moment those data are not easily accessible, and many studies have to make major simplifications to perform the simulations, such as not including the supra-aortic vessel in the computational domain. A further improvement of this tool might be game-changing in the computational field.

Further studies should be made using the geometries of subjects of whom the follow-up is known, in order to validate the results of the simulation and develop a deeper knowledge of the pathogenesis of the AD.

6 Bibliography

[1] Marrocco-Trischitta MM, Alaidroos M, Romarowski RM, Secchi F, Righini P, Glauber M, Nano G. Geometric pattern of proximal landing zones for thoracic endovascular aortic repair in the bovine arch variant. European Journal of Vascular and Endovascular Surgery 2020; 59: 808-816

[2] Marrocco-Trischitta MM, Alaidroos M, Romarowski RM, Milani V, Ambrogi F, Secchi F, Glauber M, Nano G. Aortic arch variant with a common origin of the innominate and left carotid artery as a determinant of thoracic aortic disease: a systematic review and meta-analysis. European Journal of Cardio-Thoracic Surgery 2020; 57: 422-427

[3] Dumfarth J, Peterss S, Kofler M, Plaikner M, Ziganshin BA, Schachner T, Tranquilli M, Grimm M, Elefteriades JA. In DeBakey type I aortic dissection, bovine aortic arch is associated with arch tears and stroke. The Annals of Thoracic Surgery 2017; 104: 2001-2008

[4] Wanamaker KM, Amadi CC, Mueller JS, Moraca RJ. Incidence of Aortic Arch Anomalies in Patients with Thoracic Aortic Dissections. Journal of cardiac surgery 2013; 28: 151-154

[5] Marrocco-Trischitta MM, Romarowski RM, Alaidroos M, Sturla F, Glauber M, Nano G. Computational Fluid Dynamics Modeling of Proximal Landing Zones for Thoracic Endovascular Aortic Repair in the Bovine Arch Variant. Annals of Vascular Surgery 2020; 69: 413-417

[6] Bersi MR, Santamaría VAA, Marback K, Di Achille P, Phillips EH, Goergen CJ, Humphrey JD, Avril S. Multimodality imaging-based characterization of regional material properties in a murine model of aortic dissection. Scientific reports 2020; 10: 1-23

[7] Iliopoulos DC, Kritharis EP, Giagini AT, Papadodima SA, Sokolis DP. Ascending thoracic aortic aneurysms are associated with compositional remodeling and vessel stiffening but not weakening in age-matched subjects. The Journal of thoracic and cardiovascular surgery 2009; 137: 101-109

[8] Raaz U, Zöllner AM, Schellinger IN, Toh R, Nakagami F, Brandt M, Emrich FC, Kayama Y, Eken S, Adam M. Segmental aortic stiffening contributes to experimental abdominal aortic aneurysm development. Circulation 2015; 131: 1783-1795

[9] Hickson SS, Butlin M, Graves M, Taviani V, Avolio AP, McEniery CM, Wilkinson IB. The relationship of age with regional aortic stiffness and diameter. JACC: Cardiovascular Imaging 2010; 3: 1247-1255

[10] Kurz SD, Falk V, Kempfert J, Gieb M, Ruschinski TM, Kukucka M, Tsokos M, Grubitzsch H, Herbst H, Semmler J, Buschmann C. Insight into the incidence of acute aortic

dissection in the German region of Berlin and Brandenburg. International journal of cardiology 2017; 241: 326-329

[11] Criado FJ. Aortic dissection: a 250-year perspective. Texas Heart Institute journal 2011; 38: 694-700

[12] Khan IA, Nair CK. Clinical, Diagnostic, and Management Perspectives of Aortic Dissection. Chest 2002; 122: 311-328

[13] Golledge J, Eagle KA. Acute aortic dissection. The Lancet 2008; 372: 55-66

[14] Song J, Kim S, Kim J, Kim M, Kang D, Seo JB, Lim T, Lee JW, Song M, Song J. Long-term predictors of descending aorta aneurysmal change in patients with aortic dissection. Journal of the American College of Cardiology 2007; 50: 799-804

[15] Evangelista A, Galuppo V, Gruosso D, Cuellar H, Teixido G, Rodriguez-Palomares J. Role of entry tear size in type B aortic dissection. Annals of cardiothoracic surgery 2014; 3: 403-405

[16] Nienaber CA, Clough RE, Sakalihasan N, Suzuki T, Gibbs R, Mussa F, Jenkins MP, Thompson MM, Evangelista A, Yeh JS. Aortic dissection. Nature Reviews Disease Primers 2016; 2: 1-18

[17] Wen D, Zhou X, Li J, Hui R. Biomarkers in aortic dissection. Clinica chimica acta 2011; 412: 688-695

[18] Tsai TT, Trimarchi S, Nienaber C. Acute aortic dissection: perspectives from the International Registry of Acute Aortic Dissection (IRAD). European journal of vascular and endovascular surgery 2009; 37: 149-159

[19] Nienaber CA. Influence and critique of the INSTEAD Trial (TEVAR versus medical treatment for uncomplicated type B aortic dissection) 2011; 24: 167-171

[20] Nienaber CA, Kische S, Rousseau H, Eggebrecht H, Rehders TC, Kundt G, Glass A, Scheinert D, Czerny M, Kleinfeldt T. Endovascular repair of type B aortic dissection: long-term results of the randomized investigation of stent grafts in aortic dissection trial. Circulation: Cardiovascular Interventions 2013; 6: 407-416

[21] Li F, Wu X, Yuan J, Wang J, Mao C, Wu X. Comparison of thoracic endovascular aortic repair, open surgery and best medical treatment for type B aortic dissection: A meta-analysis. International journal of cardiology 2018; 250: 240-246

[22] Rinaudo A, D'Ancona G, Lee JJ, Pilato G, Amaducci A, Baglini R, Follis F, Pilato M, Pasta S. Predicting outcome of aortic dissection with patent false lumen by computational flow analysis. Cardiovascular Engineering and Technology 2014; 5: 176-188

[23] Bernard Y, Zimmermann H, Chocron S, Litzler J, Kastler B, Etievent J, Meneveau N, Schiele F, Bassand J. False lumen patency as a predictor of late outcome in aortic dissection. The American Journal of Cardiology 2001; 87: 1378-1382

[24] Tsai TT, Evangelista A, Nienaber CA, Myrmel T, Meinhardt G, Cooper JV, Smith DE, Suzuki T, Fattori R, Llovet A. Partial thrombosis of the false lumen in patients with acute type B aortic dissection. New England Journal of Medicine 2007; 357: 349-359

[25] Melvinsdottir IH, Lund SH, Agnarsson BA, Sigvaldason K, Gudbjartsson T, Geirsson A. The incidence and mortality of acute thoracic aortic dissection: results from a whole nation study. European Journal of Cardio-Thoracic Surgery 2016; 50: 1111-1117

[26] Dolan JM, Sim FJ, Meng H, Kolega J. Endothelial cells express a unique transcriptional profile under very high wall shear stress known to induce expansive arterial remodeling. American Journal of Physiology-Cell Physiology 2012; 302: C1109-C1118

[27] Reneman RS, Arts T, Hoeks AP. Wall shear stress--an important determinant of endothelial cell function and structure--in the arterial system in vivo. Discrepancies with theory. Journal of vascular research 2006; 43: 251-269

[28] Chi Q, He Y, Luan Y, Qin K, Mu L. Numerical analysis of wall shear stress in ascending aorta before tearing in type A aortic dissection. Computers in biology and medicine 2017; 89: 236-247

[29] Carretero OA, Oparil S. Essential hypertension: part I: definition and etiology. Circulation 2000; 101: 329-335

[30] Staessen JA, Wang J, Bianchi G, Birkenhäger WH. Essential hypertension. The Lancet 2003; 361: 1629-1641

[31] Britton KA, Gaziano JM, Djoussé L. Normal systolic blood pressure and risk of heart failure in US male physicians. European journal of heart failure 2009; 11: 1129-1134

[32] Kjeldsen SE. Hypertension and cardiovascular risk: general aspects. Pharmacological research 2018; 129: 95-99

[33] Kalaitzidis RG, Bakris GL. Prehypertension: is it relevant for nephrologists?. Kidney international 2010; 77: 194-200

[34] Arima H, Barzi F, Chalmers J. Mortality patterns in hypertension. Journal of hypertension 2011; 29: S3-S7

[35] Prospective Studies Collaboration. Age-specific relevance of usual blood pressure to vascular mortality: a meta-analysis of individual data for one million adults in 61 prospective studies. The Lancet 2002; 360: 1903-1913

[36] Wagner EN, Hong S, Wilson KL, Calfas KJ, Rock CL, Redwine LS, von Känel R, Mills PJ. Effects of Caloric Intake and Aerobic Activity in Individuals with Prehypertension and

Hypertension on Levels of Inflammatory, Adhesion and Prothrombotic Biomarkers—Secondary Analysis of a Randomized Controlled Trial. Journal of clinical medicine 2020; 9: 655

[37] Yang GH, Zhou X, Ji WJ, Liu JX, Sun J, Shi R, Jiang TM, Li YM. Effects of a low salt diet on isolated systolic hypertension: A community-based population study. Medicine 2018; 97: e0342

[38] Kanjwal K, George A, Figueredo VM, Grubb BP. Orthostatic hypotension: definition, diagnosis and management. Journal of cardiovascular medicine (Hagerstown, Md.) 2015; 16: 75-81

[39] Low PA. Prevalence of orthostatic hypotension. Clinical Autonomic Research 2008; 18: 8-13

[40] Bhave NM, Nienaber CA, Clough RE, Eagle KA. Multimodality imaging of thoracic aortic diseases in adults. JACC: Cardiovascular Imaging 2018; 11: 902-919

[41] Holloway BJ, Rosewarne D, Jones RG. Imaging of thoracic aortic disease. The British journal of radiology 2011; 84: S338-S354

[42] Di Cesare E, Splendiani A, Barile A, Squillaci E, Di Cesare A, Brunese L, Masciocchi C. CT and MR imaging of the thoracic aorta. Open Medicine 2016; 11: 143-151

[43] Campobasso R, Condemi F, Viallon M, Croisille P, Campisi S, Avril S. Evaluation of peak wall stress in an ascending thoracic aortic aneurysm using FSI simulations: effects of aortic stiffness and peripheral resistance. Cardiovascular engineering and technology 2018; 9: 707-722

[44] Nannini G. Assestment of ascending thoracic aortic aneurysm prior and after valve sparing surgery: a patient tailored fluid-structure interaction model enhanced with 4D flow MRI 2020

[45] Kim HJ, Vignon-Clementel IE, Figueroa CA, LaDisa JF, Jansen KE, Feinstein JA, Taylor CA. On coupling a lumped parameter heart model and a three-dimensional finite element aorta model. Annals of Biomedical Engineering 2009; 37: 2153-2169

[46] Madhavan S, Kemmerling EMC. The effect of inlet and outlet boundary conditions in image-based CFD modeling of aortic flow. Biomedical engineering online 2018; 17: 1-20

[47] Morbiducci U, Gallo D, Massai D, Consolo F, Ponzini R, Antiga L, Bignardi C, Deriu MA, Redaelli A. Outflow conditions for image-based hemodynamic models of the carotid bifurcation: implications for indicators of abnormal flow. Journal of Biomechanical Engineering 2010; 132

[48] Pirola S, Cheng Z, Jarral O, O'Regan D, Pepper J, Athanasiou T, Xu X. On the choice of outlet boundary conditions for patient-specific analysis of aortic flow using computational fluid dynamics. Journal of Biomechanics 2017; 60: 15-21

[49] Contarino C. . A holistic multi-scale mathematical model of the murine extracellular fluid systems and study of the brain interactive dynamics 2018

[50] Müller LO, Toro EF. A global multiscale mathematical model for the human circulation with emphasis on the venous system. International journal for numerical methods in biomedical engineering 2014; 30: 681-725

[51] Liang F, Takagi S, Himeno R, Liu H. Biomechanical characterization of ventricular–arterial coupling during aging: a multi-scale model study. Journal of Biomechanics 2009; 42: 692-704

[52] Strocchi M, Contarino C, Zhang Q, Bonmassari R, Toro EF. A global mathematical model for the simulation of stenoses and bypass placement in the human arterial system. Applied Mathematics and Computation 2017; 300: 21-39

[53] Montecinos GI, Müller LO, Toro EF. Hyperbolic reformulation of a 1D viscoelastic blood flow model and ADER finite volume schemes. Journal of Computational Physics 2014; 266: 101-123

[54] Parés C. Numerical methods for nonconservative hyperbolic systems: a theoretical framework. SIAM Journal on Numerical Analysis 2006; 44: 300-321

[55] Castro CE, Toro EF. Roe-type Riemann solvers for general hyperbolic systems. International Journal for Numerical Methods in Fluids 2014; 75: 467-486

[56] Toro EF, Thornber B, Zhang Q, Scoz A, Contarino C. A Computational Model for the Dynamics of Cerebrospinal Fluid in the Spinal Subarachnoid Space. Journal of Biomechanical Engineering 2019; 141

[57] Burkhoff D, Sayer G, Doshi D, Uriel N. Hemodynamics of mechanical circulatory support. Journal of the American College of Cardiology 2015; 66: 2663-2674

[58] Kaye D, Shah SJ, Borlaug BA, Gustafsson F, Komtebedde J, Kubo S, Magnin C, Maurer MS, Feldman T, Burkhoff D. Effects of an interatrial shunt on rest and exercise hemodynamics: results of a computer simulation in heart failure. Journal of cardiac failure 2014; 20: 212-221

[59] Reymond, Reymond P, Crosetto P, Deparis S, Quarteroni A, Stergiopulos N. Physiological simulation of blood flow in the aorta: Comparison of hemodynamic indices as predicted by 3-D FSI, 3-D rigid wall and 1-D models. Medical engineering & physics 2013; 35: 784-791

[60] Mendez, Mendez V, Di Giuseppe M, Pasta S. Comparison of hemodynamic and structural indices of ascending thoracic aortic aneurysm as predicted by 2-way FSI, CFD rigid wall simulation and patient-specific displacement-based FEA. Computers in biology and medicine 2018; 100: 221-229

[61] Crosetto, Crosetto P, Reymond P, Deparis S, Kontaxakis D, Stergiopulos N, Quarteroni A. Fluid–structure interaction simulation of aortic blood flow. Computers & Fluids 2011; 43: 46-57

[62] Pons R, Guala A, Rodríguez-Palomares JF, Cajas J, Dux-Santoy L, Teixidó-Tura G, Molins JJ, Vázquez M, Evangelista A, Martorell J. Fluid–structure interaction simulations outperform computational fluid dynamics in the description of thoracic aorta haemodynamics and in the differentiation of progressive dilation in Marfan syndrome patients. Royal Society open science 2020; 7: 191752

[63] Lantz J, Renner J, Karlsson M. Wall shear stress in a subject specific human aorta—influence of fluid-structure interaction. International Journal of Applied Mechanics 2011; 3: 759-778

[64] Oliveira, OLIVEIRA D, LARANJO S, TIAGO J, PINTO F, SEQUEIRA A. NUMERICAL SIMULATION OF DILATION PATTERNS OF THE ASCENDING AORTA IN AORTOPATHIES. Journal of mechanics in medicine and biology 2020; 20: 1950068

[65] Pasta S, Rinaudo A, Luca A, Pilato M, Scardulla C, Gleason TG, Vorp DA. Difference in hemodynamic and wall stress of ascending thoracic aortic aneurysms with bicuspid and tricuspid aortic valve. Journal of Biomechanics 2013; 46: 1729-1738

[66] Suito H, Takizawa K, Huynh VQ, Sze D, Ueda T. FSI analysis of the blood flow and geometrical characteristics in the thoracic aorta. Computational Mechanics 2014; 54: 1035-1045

[67] Gao F, Matsuzawa T. FSI within Aortic Arch Model over Cardiac Cycle and Influence of Wall Stiffness on Wall Stress in Layered Wall. Engineering letters 2006; 13

[68] Gao F, Ohta O, Matsuzawa T. Fluid-structure interaction in layered aortic arch aneurysm model: assessing the combined influence of arch aneurysm and wall stiffness. Australasian Physics & Engineering Sciences in Medicine 2008; 31: 32

[69] Gao F, Guo Z, Sakamoto M, Matsuzawa T. Fluid-structure interaction within a layered aortic arch model. Journal of Biological Physics 2006; 32: 435-454

[70] Savabi, Savabi R, Nabaei M, Farajollahi S, Fatouraee N. Fluid structure interaction modeling of aortic arch and carotid bifurcation as the location of baroreceptors. International Journal of Mechanical Sciences 2020; 165: 105222

[71] Sturla F, Votta E, Stevanella M, Conti CA, Redaelli A. Impact of modeling fluid–structure interaction in the computational analysis of aortic root biomechanics. Medical engineering & physics 2013; 35: 1721-1730

[72] Khanafer K, Berguer R. Fluid–structure interaction analysis of turbulent pulsatile flow within a layered aortic wall as related to aortic dissection. Journal of Biomechanics 2009; 42: 2642-2648

[73] Warfield SK, Zou KH, Wells WM. Simultaneous truth and performance level estimation (STAPLE): an algorithm for the validation of image segmentation. IEEE Transactions on Medical Imaging 2004; 23: 903-921

[74] Izzo R, Steinman D, Manini S, Antiga L. The vascular modeling toolkit: a Python library for the analysis of tubular structures in medical images. Journal of Open Source Software 2018; 3: 745

[75] Gijsen FJ, van de Vosse, Frans N, Janssen J. The influence of the non-Newtonian properties of blood on the flow in large arteries: steady flow in a carotid bifurcation model. Journal of Biomechanics 1999; 32: 601-608

[76] Arzani A. Accounting for residence-time in blood rheology models: do we really need non-Newtonian blood flow modelling in large arteries?. Journal of The Royal Society Interface 2018; 15: 20180486

[77] Courant R, Friedrichs K, Lewy H. On the partial difference equations of mathematical physics. IBM journal of Research and Development 1967; 11: 215-234

[78] Courtial E, Fanton L, Orkisz M, Douek P, Huet L, Fulchiron R. Hyper-viscoelastic behavior of healthy abdominal aorta. IRBM 2016; 37: 158-164

[79] Gasbarro MD, Shimada K, Di Martino ES. Mechanics of abdominal aortic aneurysm. European Journal of Computational Mechanics/Revue Européenne de Mécanique Numérique 2007; 16: 337-363

[80] Tezduyar TE, Sathe S, Cragin T, Nanna B, Conklin BS, Pausewang J, Schwaab M. Modelling of fluid–structure interactions with the space–time finite elements: Arterial fluid mechanics. International Journal for Numerical Methods in Fluids 2007; 54: 901-922

[81] Peiffer V, Sherwin SJ, Weinberg PD. Does low and oscillatory wall shear stress correlate spatially with early atherosclerosis? A systematic review. Cardiovascular research 2013; 99: 242-250

[82] Hoi Y, Zhou Y, Zhang X, Henkelman RM, Steinman DA. Correlation between local hemodynamics and lesion distribution in a novel aortic regurgitation murine model of atherosclerosis. Annals of Biomedical Engineering 2011; 39: 1414-1422

[83] Shang EK, Nathan DP, Fairman RM, Bavaria JE, Gorman RC, Gorman III JH, Jackson BM. Use of computational fluid dynamics studies in predicting aneurysmal degeneration of acute type B aortic dissections. Journal of vascular surgery 2015; 62: 279-284

[84] Meng H, Tutino VM, Xiang J, Siddiqui A. High WSS or low WSS? Complex interactions of hemodynamics with intracranial aneurysm initiation, growth, and rupture: toward a unifying hypothesis. AJNR.American journal of neuroradiology 2014; 35: 1254-1262

[85] Tse KM, Chiu P, Lee HP, Ho P. Investigation of hemodynamics in the development of dissecting aneurysm within patient-specific dissecting aneurismal aortas using computational fluid dynamics (CFD) simulations. Journal of Biomechanics 2011; 44: 827-836

[86] Mylonas SN, Barkans A, Ante M, Wippermann J, Böckler D, Brunkwall JS. Prevalence of bovine aortic arch variant in patients with aortic dissection and its implications in the outcome of patients with acute type B aortic dissection. European Journal of Vascular and Endovascular Surgery 2018; 55: 385-391

[87] Zhao L, Odigwe B, Lessner S, Clair D, Mussa F, Valafar H. Automated Analysis of Femoral Artery Calcification Using Machine Learning Techniques 2019: 584-589

[88] Petit C, Mousavi SJ, Avril S. Chapter 6 - Review of the Essential Roles of SMCs in ATAA Biomechanics. In: Doweidar MH, ed. Advances in Biomechanics and Tissue Regeneration: Academic Press. 2019: 95-114

[89] Chiu P, Miller DC. Evolution of surgical therapy for Stanford acute type A aortic dissection. Annals of cardiothoracic surgery 2016; 5: 275-295

[90] Nannini G. Assestment of ascending thoracic aortic aneurysm prior and after valve sparing surgery: a patient tailored fluid-structure interaction model enhanced with 4D flow MRI 2020

[91] van Wyk S, Prahl Wittberg L, Bulusu KV, Fuchs L, Plesniak MW. Non-Newtonian perspectives on pulsatile blood-analog flows in a 180 curved artery model. Physics of Fluids 2015; 27: 071901

[92] Canaud L, Gandet T, Marty-Ané C, Alric P. Trattamento endovascolare delle dissecazioni croniche dell'aorta toracica e toracoaddominale. EMC - Tecniche Chirurgiche Vascolare 2018; 23: 1-14

[93] Whitlock MC, Hundley WG. Noninvasive imaging of flow and vascular function in disease of the aorta. JACC: Cardiovascular Imaging 2015; 8: 1094-1106

[94] Baskurt OK, Meiselman HJ. Blood rheology and hemodynamics. Seminars in thrombosis and hemostasis 2003; 29: 435-450

[95] Sakamoto I, Sueyoshi E, Uetani M. MR Imaging of the Aorta. Radiologic clinics of North America 2007; 45: 485-497

[96] Sherifova S, Holzapfel GA. Biochemomechanics of the thoracic aorta in health and disease. Progress in Biomedical Engineering 2020; 2: 032002

RINGRAZIAMENTI

Vorrei partire ringraziando il professor Redaelli per avermi accettato come tesista e avermi sostenuta nel mio intento di svolgere la mia tesi all'estero. Nonostante io non sia potuta partire, ho avuto la fortuna di poter svolgere questo progetto in collaborazione con l'università di Calgary, rendendo questa esperienza unica seppure faticosa.

Un ringraziamento sentito alla professoressa Di Martino per avermi dato la possibilità di svolgere questo lavoro di tesi e per avermi fatto sentire parte del suo team nonostante la distanza imposta dalla pandemia. Un grazie in particolare ad Arianna per essere stata un punto di riferimento in questo percorso, sempre disponibile a rispondere alle mie domande e a fare una call per discutere come risolvere qualunque problema insorgesse. La tua esperienza e i tuoi insegnamenti mi hanno permesso di crescere ed imparare molto.

Vorrei poi ringraziare tutti gli amici che mi hanno accompagnato in questi anni. Un grazie immenso a Giulia per essere la persona su cui posso sempre contare, per aver creduto in me più di quanto ci credessi io e per avermi regalato sorrisi e felicità ogni giorno di questo percorso. Un grazie altrettanto grande a Valentina per aver condiviso con me il percorso alla scoperta di me stessa, per avermi aiutato a crescere, per il suo sorriso e per il sostegno incondizionato. Grazie a Francesca per la sua dolcezza, per i tanti momenti condivisi e per essere un esempio a inseguire i propri sogni e a farsi in quattro per raggiungerli. Grazie a Elisa, la mia compagna di riscaldamento, perché con la sua gioia e la sua voglia di vivere mi ha aiutato a trovare un lato positivo anche nei giorni più difficili. Ringrazio anche Arianna, Marta e Ylenia per essere la mia squadra in campo e nella vita. Un grazie a Cecilia, Sara e Alessia per esserci dal giorno uno, per aver creduto in me sempre e per aver condiviso ogni momento. Vorrei ringraziare anche Gabriele, Valerie, Eleonora e Giovanni e tutte le persone che hanno condiviso con me momenti e parti importanti di questo cammino.

Infine il ringraziamento più grande va alla mia famiglia senza la quale non potrei essere qui oggi. Ringrazio i miei genitori per avermi sempre spronato a fare del mio meglio, per aver festeggiato i miei successi e aver condiviso frustrazioni e delusioni. E ringrazio mia sorella Arianna che mi ha supportato sempre, ha sempre preso le mie difese e mi è stata vicina ogni giorno. Grazie per essere al mio fianco.